FACULTY OF TECHNOLOGY

KINEMATIC ANALYSIS OF THE STAGE 5 DESIGN OF THE KEVITSA OPEN PIT MINE

Carlos Andrés Escalante Cárdenas

Mineral Resources and Sustainable Mining Master's Program

Mining Engineering and Mineral Processing Specialization

Master's thesis

June 2023

ABSTRACT

Kinematic Analysis of the Stage 5 Design of the Kevitsa Open Pit Mine.

Carlos Escalante

University of Oulu, Mineral Resources and Sustainable Mining Master's Program, Mining Engineering and Mineral Processing Specialization.

Master's thesis 2023, 106 pages + 24 appendixes

Supervisor(s) at the university: Dr. Adeyemi Aladejare.

The development of a new pushback in the Kevitsa Open Pit Mine has raised concerns regarding the potential impact of minor and major geological discontinuities on the overall stability of the pit. Furthermore, the daily mining operations are continuously threatened by frequent rock falls that occasionally exceed the bench slope scale, posing hazards in terms of safety and economics. Despite these challenges, the structures or group of structures responsible for most of the rock falls have not been confidently identified. This study reviews the effect of the structural features within the Kevitsa area into the open pit excavation and the proposed slopes of the Stage 5 pit design. To achieve this, structural mapping of rock surfaces was performed using 3D photogrammetry. The collected data was integrated with geotechnical logging data and laser scan data to characterize the dominant joint orientations of the deposit. Kinematic analyses of rock blocks were carried out by stereographic projection techniques to identify potential instabilities in the bench, inter-ramp, and overall slopes of the Stage 5 pit design. Results establish that two areas in the current pit and Stage 5 have major slope instability, where bench and inter-ramp slope failures are attributed to specific joint sets. Moreover, potential planar and wedge failures of overall slope scale are identified. Based on the findings, recommendations for pit optimization and geotechnical investigations are made.

Keywords: Slope stability, Kinematic analysis, Open pit mining, Kevitsa deposit, Pit optimization, Structural geology, Joint set.

FOREWORD

The present thesis aims to contribute to the structural model of the Kevitsa open pit mine and the geotechnical assessment of the proposed Stage 5 pit.

The research was carried out during December 2022 and June 2023 at the New Boliden Kevitsa mine in Sodankylä. I am very grateful to the New Boliden, and more specifically to M.Sc. Pekka Bergström and M.Sc. Esko Pystynen for granting me the opportunity to develop this project.

The products and accomplishments of this work are principally dedicated to God, as nothing would be possible without his guidance and protection.

To my parents, that built every step that took me to this moment. Very soon we will be celebrating this achievement together.

To my dear wife Carolina, who is my daily motivation in life. Thanks for all the love and the support. You and Kebab are my home.

Additionally, I want to express my most sincere gratitude to my supervisor Dr. Adeyemi Aladejare for his guidance before and during the development of the thesis.

To Dr. Sonja Pabst for all her comments and contributions to the project, and to MSc. Loraine Berthet for her support and disposition to help.

Sodankylä, 01.06.2023

Carlos Andrés Escalante Cárdenas

Author

TABLE OF CONTENTS

1 INTRODUCTION

Open pit mining can be defined as a surface mining method that takes care of extracting near-surface ore deposits through a cone-shaped excavation that uses one or more horizontal benches to extract the ore (Altiti et al., 2021). The exploitation of an open pit deposit generally occurs through different phases, also referred to as pushbacks, that represent the extraction of minerals from one or more benches simultaneously (Arteaga et al., 2014). These phases must be carefully designed as they define the long-term strategy for the sequential development of the mine, establishing the schedule of core operational activities such as drilling, blasting, and load and hauling (Gu et al., 2021).

The success of the phases of an open pit mine rely substantially on the stability of its slopes, as they directly impact the economic and safety aspects of the mining operations. Excavation activities generate volumetric, and stress and strain changes in the rock mass surrounding the mine opening, where instability conditions and rock failure can occur when the deformation exceeds the limits defined by the rock strength (Osasan & Afeni, 2010). Therefore, the design of the rock slopes must guarantee satisfactory stability and economic performance during and after excavation, to avoid undesired rock mass movement that can affect human life, basic properties, and ore reserves (Aladejare & Wang, 2017; Aladejare & Akeju, 2020; Kolapo, 2022).

The typical design of an open pit mine is constituted by the global or overall pit slopes, which are defined by a series of stacked benches contained in the inter-ramp slopes (Kuchling, 2015). This means that the essential geotechnical design of an open pit starts at the bench scale configuration, where the slope stability is mainly controlled by the geological discontinuities within the rock mass (i.e., rock joints) that can develop structurally controlled failure mechanisms such as planar, wedge, and toppling failure (Obregon & Mitri, 2019; Lana, 2014). In comparison, the stability of large-scale slopes (i.e., overall and inter-ramp) is controlled by the impact of intermediate and major structures (e.g., faults), as well as the overall strength of the rock mass. Nevertheless, the stability of slopes at every scale relies substantially on the possible movements of its rock blocks. Kinematic analysis is the most common procedure used to evaluate whether blocks or masses of rock may move along discontinuities, sliding out of the face of a slope (Mote, 2004).

Boliden's Kevitsa mine is a Ni-Cu-PGE open pit mine that operates in the municipality of Sodankylä in northern Finland, with a current life of mine plan projected to last until 2034 (Stage 4). Recently, it has been evaluated that there is possibility to extend the life of the mine by developing a new phase (Stage 5) for the open pit. However, the operational activities required for the development of the new pushback (e.g., drill and blasting, load and hauling) are threatened by slope instabilities of different scales. These are due to the influence of minor and major geological structures which are under recurring interpretation as the mine's structural model is being updated constantly.

The slope instabilities of the pit are principally indicated by the monitoring of rock falls around the mine that have identified wedge failure as the typical failure mode occurring at a bench and inter-ramp scale. Additionally, larger-scale structures that can impact the overall-slopes have been identified through geotechnical risk assessments, such as the discovery of a ~9.2Mt unstable wedge in the south-eastern section of the pit (SRK, 2021). Therefore, the consideration of a new phase for the open pit requires a detailed geotechnical evaluation that examines the potential instability modes that could be developed in the different slopes of the Stage 5 design, and furthermore identify the geological structures associated to them.

This study aims to contribute to the geotechnical evaluation of the Stage 5 design of the Kevitsa open pit mine, as well to its structural model, by the development of a comprehensive two-dimensional (2D) kinematic analysis of the minor discontinuities (rock joints) and the major structures (e.g., faults, veins) found in the deposit's rock mass.

The study starts by conducting a phase of structural mapping using 3D photogrammetry to identify potential trends in the orientation and persistence of the rock joints around the mine site. This information is used collectively with core logging data to evaluate if the observed discontinuities together with the proposed excavation slopes of the new stage design create unfavorable conditions. Such conditions can include bench failure along the discontinuity surfaces or pair of intersecting discontinuities, developing planar, wedge, or toppling failure modes. Multi-bench or inter-ramp instabilities are then evaluated by analyzing the intersection of the major geological structures with the slopes, and their possible interactions with rock joint trends that extend beyond the bench-scale. Lastly, the kinematics of rock blocks at an overall slope scale are evaluated according to the interaction of the major structures with the proposed excavation slopes.

The 2D kinematic analyses at bench, inter-ramp, and overall scale are developed for each of the proposed excavation slopes of the Stage 5 pit design by stereographic analyses plots generated using Rocscience DIPS.

1.1 Objectives

The objectives of the study are to:

(1) Perform structural mapping in the pit walls of the Kevitsa open pit mine to identify trends in the orientation and persistence of the minor discontinuities (rock joints) of the deposit.

(2) Identify the potential structurally controlled failure mechanisms at bench, inter-ramp, and overall scale in each of the proposed excavation slopes of the Stage 5 design of the Kevitsa open pit mine.

(3) Identify the geological structures associated with the likely failure modes of the different slopes of the Kevitsa open pit mine.

(4) Develop stereographic analyses plots for kinematic analysis of rock blocks for the evaluation of planar, wedge, and toppling failure modes.

2 THEORETICAL REVIEW

Open-pit mining is the most common method used throughout the world for mineral excavation. It is characterized by large capital investments requirements that often result in high productivity, low operating costs, and good safety conditions, which translates to an overall positive turnover of the operations. The surface mining method excavates near-surface deposits, and can be applied to nonselective, low-grade zones, and metallic and non-metallic ore deposits (Altiti et al., 2021).

The main goal of open pit mining is to remove the smallest amount of material, while processing the biggest amount of marketable mineral product, and consequently obtaining the greatest return on the investment. This requires a pit design and operating plan that dictates in which way the ore body will be extracted, where one of the main challenges consists of maintaining the stability of the pit slopes while achieving maximum ore recovery (Altiti et al., 2021; Obregon & Mitri, 2019). According to Read & Stacey (2009), uncontrolled stability and/or slope failure may have repercussions that impact different aspects of the mining operations (Table 1). Therefore, a minimum degree of stability must be assured at every scale of the pit design (from the overall slopes to the individual benches), and at every stage of the life of mine plan (Read & Stacey, 2009).

Table 1. Effects of slope instability in open pit mining (Read and Stacey, 2009).

Safety / Social	Economic / Operational	Environmental / Regulatory
Loss of life or injury	Disruption of the operations	Impacts to the environment
Loss of worker income	Loss of the ore	Increased regulations
Loss of worker confidence	Loss of equipment	Closure considerations
Loss of corporate credibility	Increased stripping	
	Costs of cleanup	
	Loss of markets	

2.1 Principles of Slope Design in Open Pit mines

The extraction of minerals in an open pit mine is made through benches that are stacked in the slopes that define the boundary of the pit. These slopes are geotechnical structures, and their design must be based on a well-controlled methodology that is planned according to the specific rock mass of the deposit and its geological structure (Fleurisson, 2012).

The general configuration of an open pit slope is made up from three main components (Figure 1) according to Wyllie & Mah (2004):

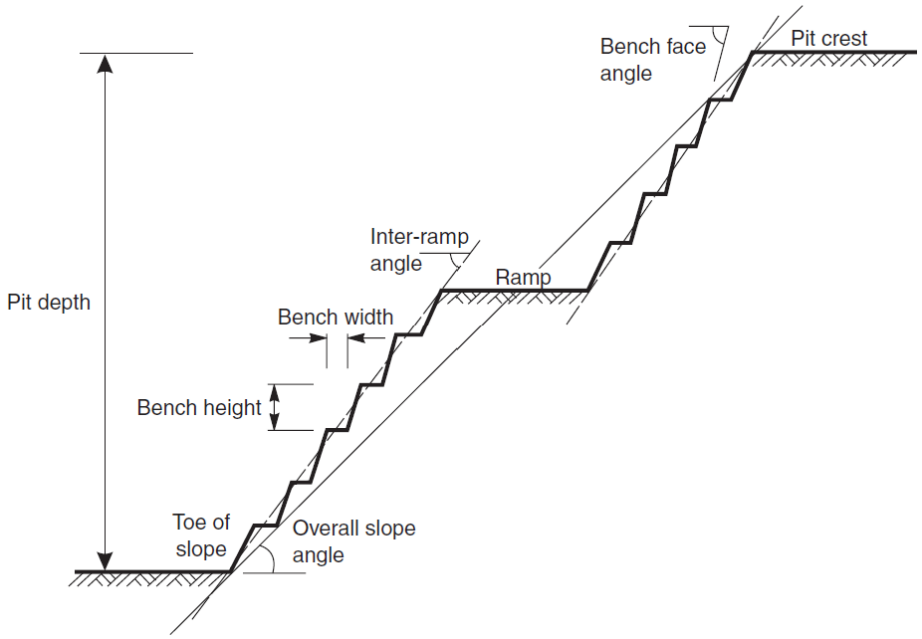

Figure 1. Typical configuration of the slopes of an open pit mine (Wyllie & Mah, 2004).

First, the overall pit slope angle from crest to toe, defines the inclination of the overall slope that includes all ramps and benches. This angle is generally designed to produce flatter slopes in weak and surficial materials; and designed to produce steeper slopes in more competent rocks. The angle can be varied to accommodate changes in the geology and the layout of the ramp. Secondly, the inter-ramp slope angle defines the inclination of the slope, or slopes, lying between each ramp, and it depends on the number of ramps and their widths. Lastly, the face angle of the individual benches depends on the vertical spacing between benches, or combined multiple benches, and the width of the benches that are required to contain minor rock falls.

The design of these components and the final geometry of the overall slope are furthermore influenced by the geology, rock strength, ground water pressures, excavation induced stress, excavation equipment, operator capabilities, mine planning constraints, and regulatory restrictions (Wyllie & Mah, 2004; Read & Stacey, 2009).

2.1.1 Design Methodology

The design of an open pit slope is based on the formulation of design criteria that incorporates the analysis and prediction of the failure modes that could affect the slope at bench, inter-ramp, and overall scale (Read & Stacey, 2009).

The design process consists of the construction of a geotechnical model for the proposed pit area, which will be the foundation of the design approach (Figure 2).

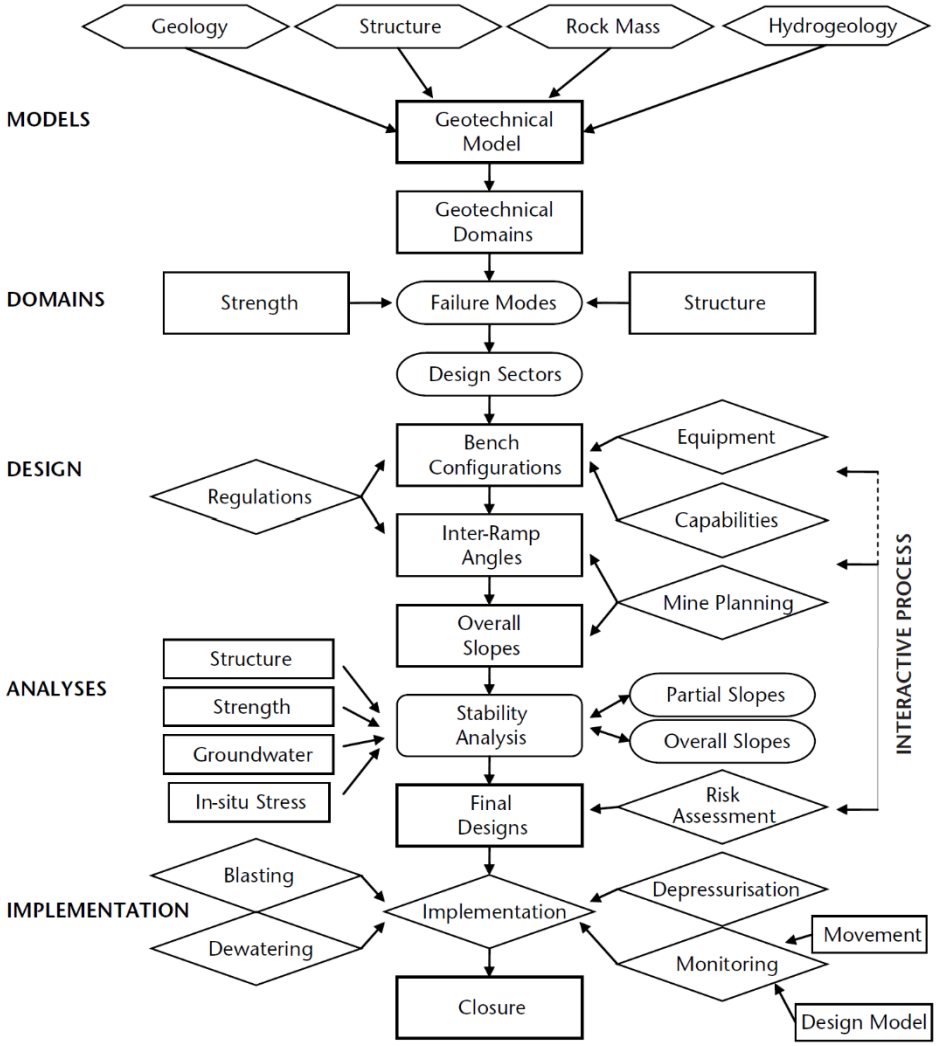

Figure 2. Slope design process (Read & Stacey, 2009).

This phase requires the characterization of the rock mass of the deposit, involving the acquisition of geological, geomechanical, and hydrogeological data used to analyze the materials behavior. The collection of data can be done through field investigations (outcrop mapping, diamond drilling, and geotechnical logging); subsurface geophysical methods (magnetometry and seismic); and laboratory investigations (breakage and shear tests). Then, the quality of the data is assessed, and a geotechnical model is built based on the geological, structural, and hydrogeological models (Read & Stacey, 2009; Wyllie & Mah, 2004; Nicholas & Sims, 2001).

Next, the geotechnical model is divided into domains where the rocks share similar characteristics, which are used to assess potential failure mechanisms. Finally, based on failure analyses, different slope designs are proposed for the pit sectors that will require

approval and compliance in terms of stability with company policies, industrial standards, and/or regulatory requirements (Read & Stacey, 2009).

2.1.2 Design Evaluation

The final design of an open pit must be evaluated through one or multiple stability analyses according to the stage and aim of the project, anticipated failure mode, scale of the slope and/or feature, and data availability. The main types of analyses are described by Read & Stacey (2009) as:

(1) Kinematic analyses: Based on stereographic projections that analyze the geometrically possible motions of the rock blocks of the slope, and their associated modes of failure (planar, wedge, or toppling).

(2) Limit equilibrium analyses: Applied to structurally controlled failures in bench and inter-ramp design; and inter-ramp and overall slope design where the instability is mainly governed by the rock mass strength.

(3) Numerical analyses: Application of finite element and distinct element methods for the assessment of inter-ramp and overall slopes.

To obtain reliable results, these methods require understanding of the structural geology within the rock mass evaluated. Structures such as fractures, joints, bedding planes, and faults play a crucial role in contributing to either the stabilization or destabilization of the rock slope. Therefore, sufficient geological data of consistent quality is required to perform the analyses (Stead & Wolter, 2015; Wyllie & Mah, 2004; Read & Stacey, 2009).

2.2 Geological Data Collection

The characterization of rock masses for geotechnical engineering applications focusses on describing the geometrical properties (e.g., orientation, spacing, length, persistence) of the geological discontinuities within the rock mass. This has been typically achieved through the survey of rock exposures (i.e., outcrops) and drill core logging (Hoek et al., 2000; Villaescusa, 2014). However, the implementation of modern technologies for digital imaging has made data collection more efficient as it allows the measurement of structural properties in a safe, remote, and accurately way over long distances (Read &

Stacey, 2009). The next subsection describes the most significant techniques for the present study.

2.2.1 Geotechnical Core Logging

The purpose of geotechnical core logging is to describe the nature of the structural and geological defects exposed in the drill core. It provides the in-situ position of the structures, which is used to determine favorable and unfavorable conditions of the rock mass for rock slope stability analysis. In addition to their position, properties such as orientation, spacing, persistence, frequency, and roughness are recorded from the structures (Read & Stacey, 2009; Ureel et al., 2013).

The measurement of planar structures in oriented diamond drill cores (DD) can be done in two ways. The first one, considered as the classical way, requires the implementation of a core frame that is used to place the core in the same orientation as it did in the moment of drilling. Once the core has been orientated, the structures within the core are measured using a geologist's compass. The second way to measure structures is the internal core angle technique, which involves the measurement of two different angles (alpha and beta) that a planar structure forms with the Core Axis (CA) and the Bottom of the Hole (BOH) lines in oriented and surveyed diamond drill cores (Figure 3). These angles are typically processed by specialized software to generate the attitude of the measurement in standard terms (dip/dip direction) (Marjoribanks, 2021).

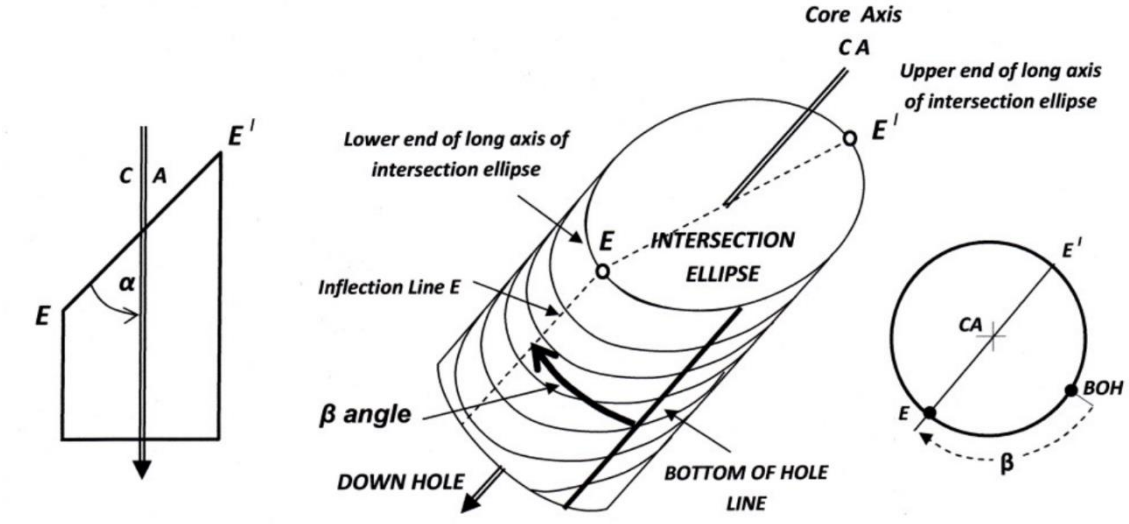

Figure 3. Definition of alpha and beta angles (Marjoribanks, 2021).

When collecting structural data from drill core logging it is important to acknowledge the existence of "blind zones" in the drill holes, which consists of the locus of the poles of

the structures that are parallel to the drill hole and cannot be seen by the drill hole (Read & Stacey, 2009).

Terzaghi (1965) noted that the only way to fully overcome the effect of blind zones is to drill a sufficient number of drill holes in such way that their orientation leaves no structural pole laying near the blind zone of each drill hole. However, this is not always possible due to high cost and complexity of diamond drilling. An alternative method to partially overcome these blind zones is the application of the Terzaghi correction or Terzaghi weighting, which is used to stablish an approximate indication of the relative proportion of the structural features where a single drill hole or scan line orientation has created bias in the orientation of the structural data. This can be done by assessing the relative proportions of the individual structures intersected in the drillhole by a series of equations, however, the process has already been computerized and incorporated into stereographic projection software's (e.g., Rocscience DIPS) (Read & Stacey, 2009).

2.2.2 Televiewer Logging

Optical (OTV) and acoustic (ATV) televiewers provide continuous and oriented 360° images of the drill hole walls during diamond drilling (Figure 4), which allows the characterization of the orientation, character, and relation of lithologic and structural features of the rock mass (Read & Stacey, 2009; Thomas et al., 2015).

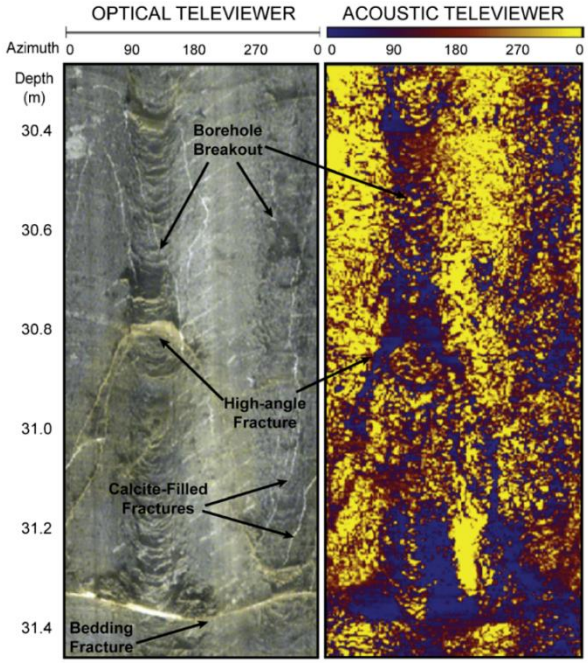

Figure 4. OTV and ATV images (DesRoches, 2014).

OTV imaging systems implement lights to illuminate the drill hole, and a reflector placed in a transparent cylindrical window to focus a 360° slice of the drill hole wall. The

reflector makes part of a charge-coupled device (CCD) camera that measures the intensity of the color spectrum to differentiate the lithology and structures present in the wall of the drill hole, which are viewed directly in OTV images. As for ATV systems, they emit an ultrasonic pulse-echo and record the transit time and amplitude of the acoustic signal reflected from structural or lithological features which are intersected by the bore hole as photographic-type images (Weir, 2015; Read & Stacey, 2009).

2.2.3 Digital Imaging

The implementation of laser imaging and 3D digital photogrammetric technologies for structural mapping has increased drastically over the last few years as they have enabled a rapid, accurate, safe, and low-cost way to perform geological mapping at bench and inter-ramp scale. The technique integrates 3D digital data with 2D visual data to generate spatially accurate representations of the surface topology of the rock (Figure 5). This allows the measurement of structural properties such as orientation, length, and spacing remotely without disrupting mining operations (Sturzenegger et al., 2011).

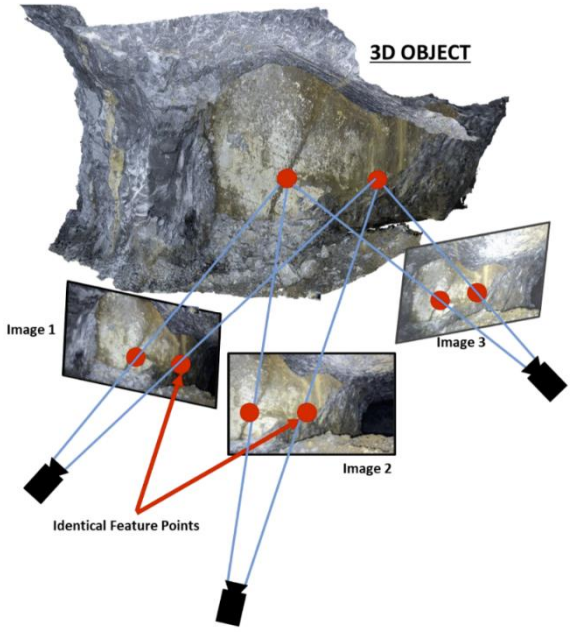

Figure 5. Use of 3D photogrammetry to identify points in a 3D space (Bishop, 2020).

Additional benefits of digital photogrammetry are its efficiency, fast application, and remote access capability (Skycatch, 2021). These have allowed the integration of the technique with mine planning software's, allowing the data to be used in real time for mine planning, design, and operational applications. The method has become an established routine for mapping exposed rock faces in open-pit and underground environments (Read & Stacey, 2009).

2.3 Structural Features

The compilation and interpretation of structural data is made through a structural model that describes the orientation and spatial distribution of the defects that might influence the stability of the pit slopes. Due to the different scale of geotechnical structures and discontinuities across the mine site, the structural model for stability analyses should be arranged to describe: the major structural features that are used to subdivide the mine site into structural domains; and the minor structural features that are found within the defined structural domains (Read and Stacey, 2009).

2.3.1 Major Structures

From the major structures, faults can be defined as the most significant structures when designing an open pit as they can define the boundaries of different structural domains, and additionally control the overall stability of the open pit (Obregon, 2020). Faults are defined as fracture zones or surfaces where displacement is recognizable. Red & Stacey (2009) suggest the following scale for faults for slope design purposes:

Table 2. Suggested scale of fault magnitude (Read and Stacey, 2009).

Length (m)	Description
<1	Minor (small scale)
1-10	Bench
10-100	Bench to Inter-ramp
100-1000	Inter-ramp to Overall
>1000	Mine scale to regional

Additional to the scale, faults must also be characterized according to the kinematic movement of the hanging wall and the foot wall. According to Anderson's Theory of Faulting (1905), the three types of faults are normal, thrust and strike-slip faults.

Another common type of major structure found in deformed rocks are folds, which are formed when planar features such as bedding planes are deflected into curviplanar or curvilinear structures. This type of deformation is associated to bending and buckling flexuring mechanisms, which are developed due to compressive stresses (Read & Stacey, 2009). As for their classification, folds are mainly grouped according to their geometric characteristics into anticline, syncline, and monocline type folds (Malik, 2018).

2.3.2 Fabric Structures

A rock's fabric is the geometric and spatial configuration of component features within the rock. Structures such as joints, minor faults, micro-bedding, folding, and schistosity are used to characterize the bench scale structural fabric (Twiss & Moores, 2007; Read & Stacey, 2009).

In terms of slope stability, the most common and significant fabric structures are joints, which are defined as opening fractures, that are sharp and/or abrupt breaks of rock that lack a measurable displacement. The walls that define the structure will separate creating an opening, that in some cases can be filled by precipitants creating a structure called "vein" (Mandl, 2005; Cloos, 2014).

Although joints can occur individually, they are typically developed as joint sets. These can be defined as groups of joints that share a tendency in their orientation (dip angle and dip direction), spacing, and physical properties, which all together can be indicators of the structural control that the rock has gone through (Mandl, 2005). Identifying joint sets is crucial for slope stability as their orientations with the excavation slopes may generate unfavorable conditions where the bench faces could fail along the discontinuity surfaces or pair of intersecting discontinuities (Read & Stacey, 2009).

2.4 Stereographic Analyses for Structural Geology

Due to the impact of structural geological features in slope stability, it is fundamental to make an accurate interpretation of the structures. This can be challenging as it usually requires the application of descriptive geometry to have a three-dimensional image that represents the real shape and orientation of the structures. However, it's been recognized that the stereographic projection technique provides an accurate solution to this difficulty (Lisle & Leyshon, 2004; Wyllie & Mah, 2004).

During geotechnical studies, the stereographic projection technique is constantly preferred as it provides a graphical way of displaying structural data, which comes necessary when recognizing and interpretating patterns of dominant orientations. Additionally, it allows data to be analyzed by multiple standard geometrical constructions, including the kinematic analysis used for slope stability analysis (Lisle & Leyshon, 2004). The result of a stereographic projection is the stereogram, which is a representation of three-dimensional orientations in a flat surface, in which structural lines

are represented by points and structural planes by a circular arc (great circles). An alternative to represent the orientation of a plane will be the pole to the plane (Figure 6), which is the point located on the surface sphere. It is is intersected by a radial line in a direction normal to the plane (Wyllie & Mah, 2004).

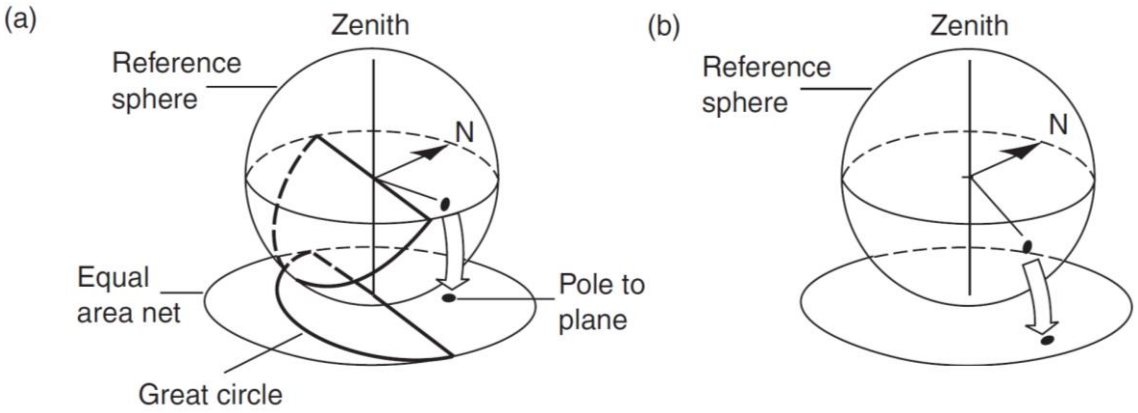

Figure 6. Equal area projections of plane and line: (a) plane projected as great circle and corresponding pole; (b) line projected as pole (Wyllie & Mah, 2004).

The method has shown to be easily adapted to computational solutions, resulting in its incorporation into multiple commercial software packages such as the Rocscience Inc. program DIPS (Read & Stacey, 2009). DIPS is a software designed for the graphical and statistical analysis of orientation data, which additionally allows to perform kinematic analysis of rock blocks. Hence, the software was chosen for the analyses of this study.

2.4.1 Orientation Variability

All natural discontinuities present variations in their orientations, which results in scatter of the poles within a pole plot. This inherent characteristic can make the identification of structural trends difficult when there are multiple discontinuity sets within a dataset. To overcome this, contouring of the pole concentrations is applied in pole plots to show the density of structures on a stereogram (Wyllie & Mah, 2004; Lisle & Leyshon, 2004).

The most known and widely used methods for density calculation are the Schmidt distribution method and the Fisher distribution method, which are both incorporated into the Rocscience DIPS software for pole plot contouring. The Schmidt distribution is known as the classical method, characterized for assigning a constant influence value of one to each pole. This method is generally recommended for large datasets. As for the Fisher distribution, it is characterized by assigning a normal influence value to each pole over the surface of the sphere, rather than a point value as in the Schmidt distribution.

Recommended for small datasets as it tends to suppress any undue influence that a single measurement may generate over a group of data (Rocscience, 2023).

2.5 Failure Modes in Open Pit mines

In open pit mines, the potential harm and consequences of a slope failure is mainly associated to the geotechnical structures involved, as well as the volume of the material released and the occurrence of the failure. Three main failure modes are recognized for open pit mines according to the scale of the slope instability (Figure 7).

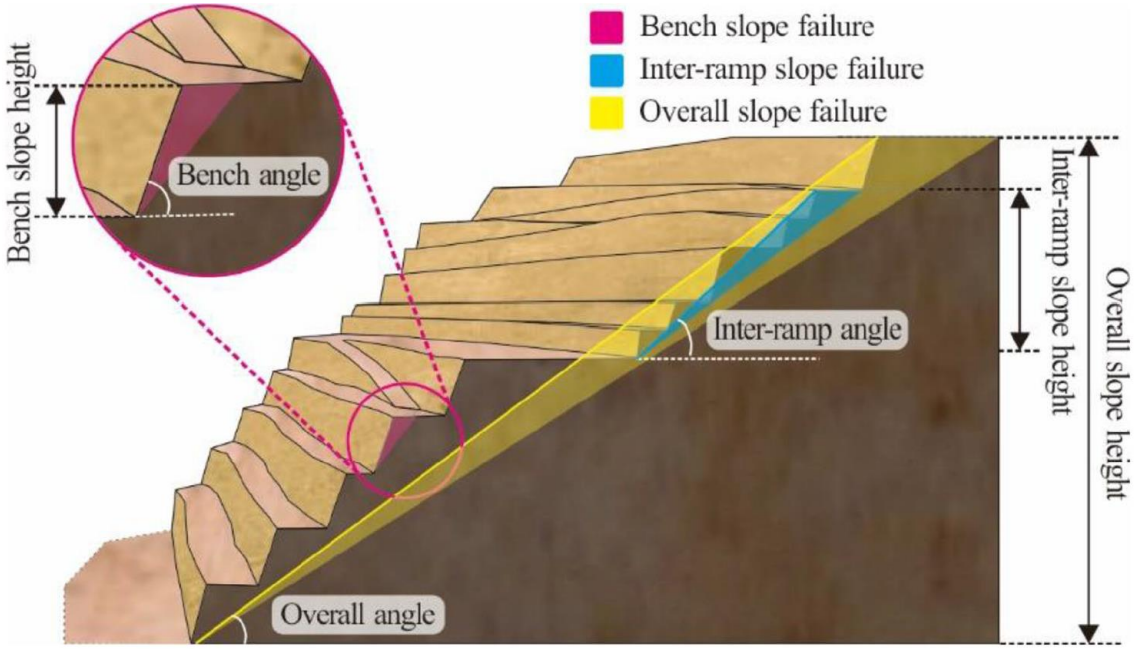

Figure 7. Different modes of slope failures in open-pit mines (Du, 2022).

(1) Bench slope failure: Local slope failures that involve merely a single bench are common and acceptable during mining operations due to their minimum economic impact on production, which is mostly associated to the clean-up costs of the released material (Dos santo et al., 2019). These types of failures are recognized to be inevitable and permissible if their consequences are not significant to haulage roads, which means that the failures of benches located immediately above and below ramps should be of lower tolerance in comparison to the other benches of the system (Priest & Brown, 1983).

Bench-scale failures do not have a significant influence in the overall mining operations. However, they are the fundamental building blocks of a pit slope, where their geometry and behavior will often control the inter-ramp and overall slope design.

For this reason, the performance of bench slopes must be carefully analyzed for each specific design sector at a mine site (Read & Stacey, 2009).

(2) Inter-ramp slope failures: Failures involving multiple benches and ramps are much less acceptable during mining operations as their consequences are more significant, typically involving significant production losses, clean-up costs, and in some cases injuries to personnel and equipment (Dos santo et al., 2019). Therefore, slope performance assessments should be carried out periodically to evaluate that the design criteria applied is appropriate for the ground conditions (Read & Stacey, 2009).

As for the geological structures associated to inter-ramp failures, they typically include the presence of two or more intersecting discontinuities, such as highly persistent bedding planes and/or joint sets that extend over the bench scale and interact with major structures (i.e., faults). At this scale, a significant consideration of the rock mass strength is required as well, especially in cases of weak or incompetent rock (Read & Stacey, 2009; Mitma, 2020).

(3) Overall slope failures: The most severe case of slope failure in an open pit is the overall slope failure as its repercussions may include injuries and fatalities of the working personnel, damage to operating equipment, loss of the geotechnical structures at every scale, and loss of the ore reserves and/or increased ore dilution (Dos santo et al., 2019). The economic impact of an overall-slope failure is typically irreversible, modifying completely the life of mine plan and economic turnover

The overall-slope design considers mainly the overall rock mass strength of the pit and the major geological structures cross-cutting the slope. The main purpose of its design is to avoid rotational shear failures that occur through the rock mass itself, and rock slope failures developed from sliding along pre-existing discontinuities (Mitma, 2020). Performance assessments are continuously carried out through the implementation of monitoring systems such as InSAR (Interferometric Synthetic Aperture Radar) and SAR (Synthetic Aperture Radar) radars (Kotavaara et al., 2023). Periodic geotechnical assessments are carried out as well to verify that the built-in slope geometries are in compliance with the slope design and the major geological structures of the deposit (Read & Stacey, 2009).

2.6 Structurally Controlled Failure Mechanisms

The structurally controlled failure mechanisms are principally gravity-driven processes that lead to the kinematic sliding of rock blocks along the rock mass discontinuities. These are typically associated to low stress environments such as those found in shallow open pit mines. The evaluation of these mechanisms is generally performed at a bench scale for highly jointed rock masses to analyze planar sliding, wedge sliding, and toppling (Mitma, 2020). Nevertheless, inter-ramp and overall slopes also require kinematic analysis of their rock blocks as they are susceptible to developing planar and wedge type failures due to the influence of intermediate and major geological structures.

2.6.1 Planar Failure

A typical planar failure (Figure 8) consists of a rock block that slides out of a slope face from a single plane that is dipping out of the slope face.

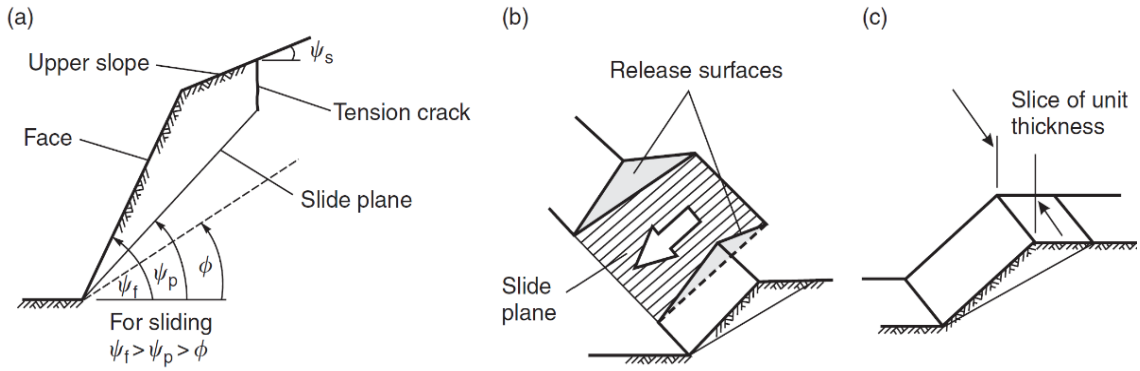

Figure 8. Geometry of a slope exhibiting a planar failure. (a) Cross section showing planes that form a planar failure; (b) release surfaces at the end of the failure plane; (c) unit thickness slide used for stability analysis (Wyllie & Mah, 2004).

For a planar failure to occur, it is required to satisfy the following geometrical conditions described by Wyllie & Mah (2004):

(1) The plane from which the sliding occurs must strike parallel or near parallel (within approximately ±20°) to the actual slope face.

(2) The plane sliding must "daylight" in the slope face, meaning that the dip of the plane is required to be less than the dip of the slope face ($\varphi_p < \varphi_f$).

(3) The dip of the sliding plane must be greater than the angle of friction of the plane ($\varphi_p > \emptyset$).

(4) The upper end of the sliding surface must intersect the upper slope or terminate in a tension crack.

(5) The release surfaces that provide negligible resistance to the sliding must be present in the rock mass in order to define the lateral boundaries of the slide.

2.6.2 Wedge Failure

The wedge failure mode is the result of the interaction between multiple discontinuities, in which their line of intersection daylights into the slope face (Figure 9).

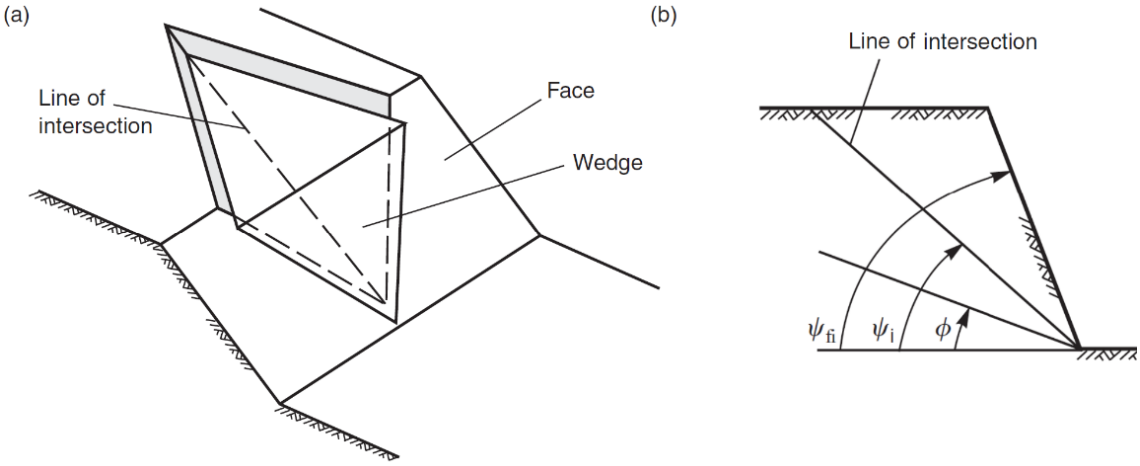

Figure 9. Geometry of a wedge failure. (a) Pictural view of wedge failure; (b) Cross-cut section of the slope showing the line of intersection (Wyllie & Mah, 2004).

The main conditions for a wedge failure to occur are described by Wyllie & Mah (2004):

(1) Two planes generate a line of intersection with an orientation defined by its trend (α_i) and its plunge (φ_i).

(2) The plunge of the line of intersection must be less than the dip of the slope face, and additionally be steeper than the average friction angle of the two slide planes (i.e., $\varphi_{fi} > \varphi_i > \emptyset$). The inclination or dip of the slope face (φ_{fi}) is measured in the view of the right angles in respect to the line of intersection.

(3) The dip direction of the line of intersection must be in direction out of the face of the slope for the sliding to be feasible.

2.6.3 Toppling Failure

For toppling failure to be developed, it is required that a highly persistent and regularly spaced set of discontinuities dips steeply into the slope face and additionally strikes sub-parallel to it (Piteau & Martin, 1982). The effect of the structural discontinuities such as joints, bedding planes, and faults will create weak planes in the rock mass that promote the kinematic rotation of blocks (Hungr et al., 2014). Toppling failures are generally classified into three types: flexural, blocky and blocky-flexural toppling (Goodman and Bray, 1976).

In open pit mines where the depth of the slopes is progressively increasing, minor toppling-type movements can eventually develop into substantial failures that impact geotechnical structures at an inter-ramp and overall-scale (Wyllie & Mah, 2004). An illustration of the progressive toppling mechanism is presented in Figure 10.

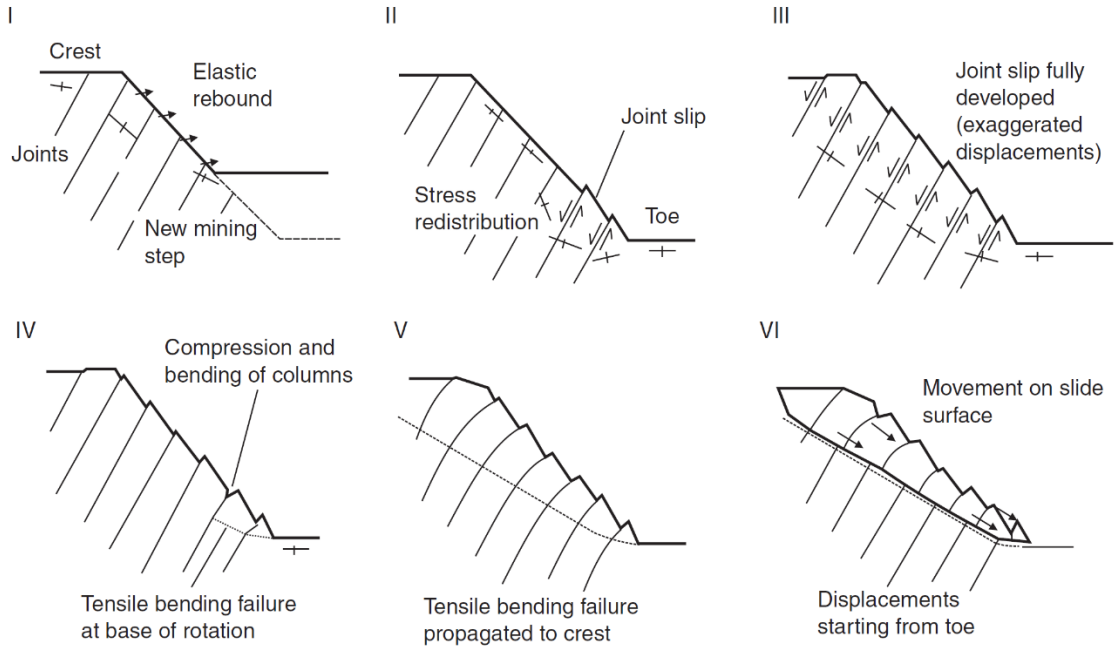

Figure 10. Failure stages for large-scale toppling failure in a slope (Sjöberg, 2000).

2.7 Identification of Failure Mechanisms

The different types of failure mechanisms are associated to different geological structures that should be recognized during the early stages of a project to avoid potential instability problems in the design of the pit slopes. These structural patterns can be recognized using stereographic pole plots as its shown in Figure 11. However, when assessing each specific failure mode, it is required that the cut face of the slope is included in the stereo plot as

the sliding is only possible to occur as the result of the movements of the rock blocks towards the slope face created by the cut (Wyllie & Mah, 2004).

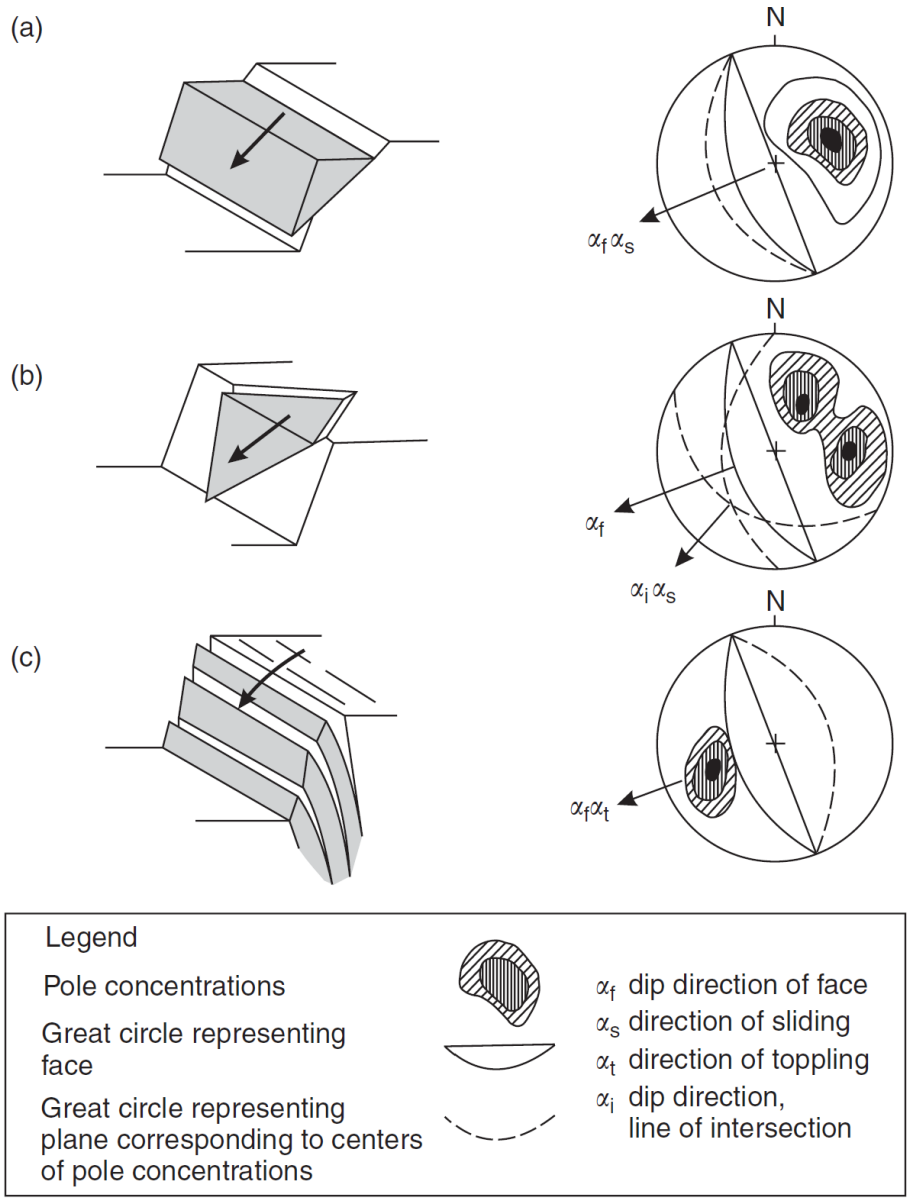

Figure 11. Main types of failure modes and their associated structural geology conditions. (a) plane failure in rock mass containing persisting joints that strike parallel and dip out of the slope face; (b) wedge failure of two intersecting discontinuity sets; (c) toppling failure by discontinuities dipping steeply into the slope face (Wyllie & Mah, 2004).

2.8 Kinematic Analysis

After identifying the potential failure modes according to the pole plot of the geological discontinuities, a kinematic analysis is carried out to examine in which direction a block may slide. This step is performed in the early stages of slope design to identify potentially unstable blocks, which is followed by a more detailed stability analysis that accounts for external forces (e.g., ground water, excavation disturbance, rock reinforcement) that can additionally have a significant impact in the stability (Wyllie & Mah, 2004).

2.8.1 Planar Failure Analysis

The planar sliding kinematic analysis evaluates the sliding of a rock block from a single plane, where potentially unstable blocks will be formed by a plane which dips at a lower angle than the slope face. However, to properly assess planar failure instabilities, additional consideration of the frictional resistance, daylighting, and lateral limits is required. These conditions should be plotted during the analysis (Wyllie & Mah, 2004).

Planar sliding kinematic analysis is performed in a stereogram where planes are plotted in terms of their plane normals (poles), where critical poles are indicated by the region inside the daylight envelope, outside the pole friction cone, and inside the lateral limits, also referred as the critical zone for planar sliding (Rocscience, 2023). Figure 12 exhibits the key components of a planar sliding kinematic analysis in a stereogram.

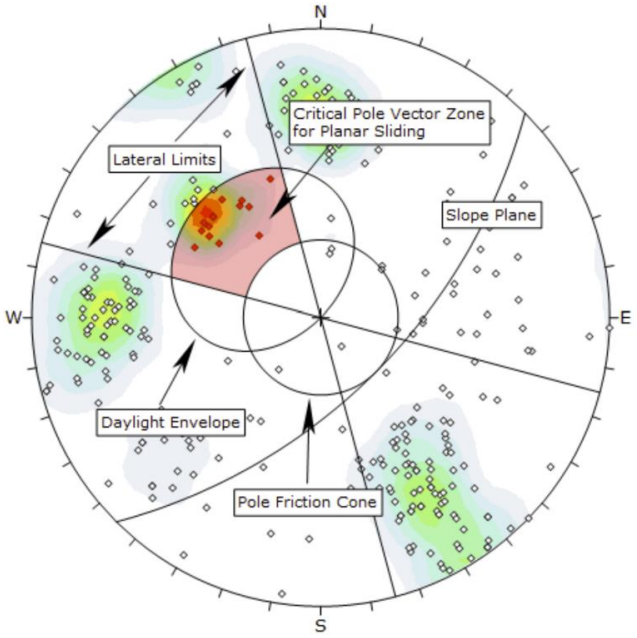

Figure 12. Components of a planar sliding kinematic analysis (Rocscience, 2023).

2.8.2 Wedge Failure Analysis

Similar to planar failure analysis, the kinematics for wedge failure are also analyzed from oriented-based data, angle of friction, and the orientation of the rock slope face. However, the assessment for wedge failure requires the consideration of the wedge sliding direction, which should be parallel to the intersection line generated by two sets of discontinuities to represent an unstable condition for wedge sliding. Unstable blocks for wedge sliding will then be indicated by the pole generated by the line of intersection of two discontinuities (Lisle & Leyshon, 2004).

As for the daylighting and frictional conditions, the pole of the intersection line will be required to daylight the slope face; and the frictional resistance that needs to be overcome will require that the plunge of the intersection line generated by the two discontinuities is greater than the friction angle of the rock mass (Wyllie & Mah, 2004; Lisle & Leyshon, 2004). Same as in planar sliding, a critical zone for wedge sliding is defined (Figure 13), which is enclosed by the region inside the plane friction cone, and the outside of the slope plane. Intersections that fall in this critical zone will then represent wedges that satisfy the frictional and kinematic conditions required for wedge sliding. The primary critical zone (highlighted in red) represents the wedges that can slide on either two planes or one plane; the secondary critical zone (highlighted in yellow) represents the wedges that can only slide on one plane (Rocscience, 2023).

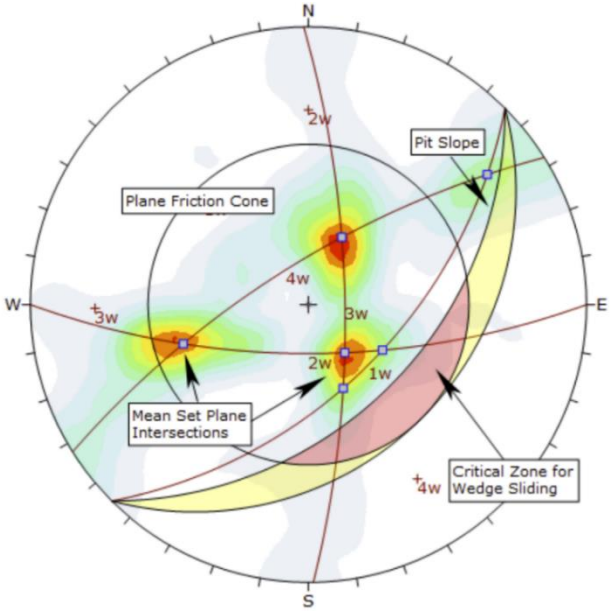

Figure 13. Wedge sliding kinematic analysis (Rocscience, 2023).

2.8.3 Toppling Failure Analysis

Goodman and Bray (1976) describe three types of toppling modes that can be encountered in the field. These should be carefully distinguished as there are two distinctive methods for their stability analysis (i.e., direct toppling and flexural toppling analysis).

(1) Block toppling: Characterized for occurring in rocks of high strength, where individual columns are formed by a set of discontinuities dipping steeply into the slope face, and a secondary set of widely space joints that define the column height. Failure occurs as the short columns forming the toe of the slope are pushed forward by the load of the longer and overturning columns behind (Wyllie & Mah, 2004). The procedure to

analyze block toppling is defined as direct toppling kinematic analysis, its key elements are presented in Figure 14.

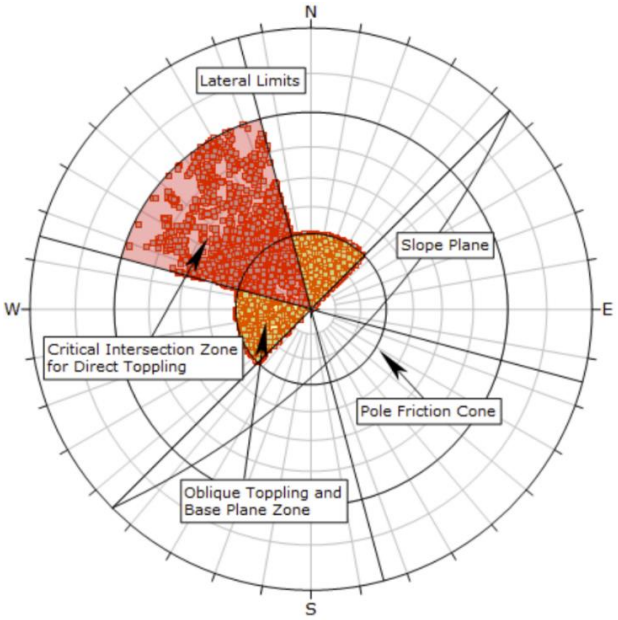

Figure 14. Direct Toppling kinematic analysis (Rocscience, 2023).

(2) Flexural Toppling: Characterized by continuous columns of rock separated by well-developed steeply dipping fractures. Failure and/or break occurs in flexure as they bend forward. Typical of thinly bedded shales and slates (Wyllie & Mah, 2004). The key elements to perform a flexural toppling kinematic analysis are presented in Figure 15.

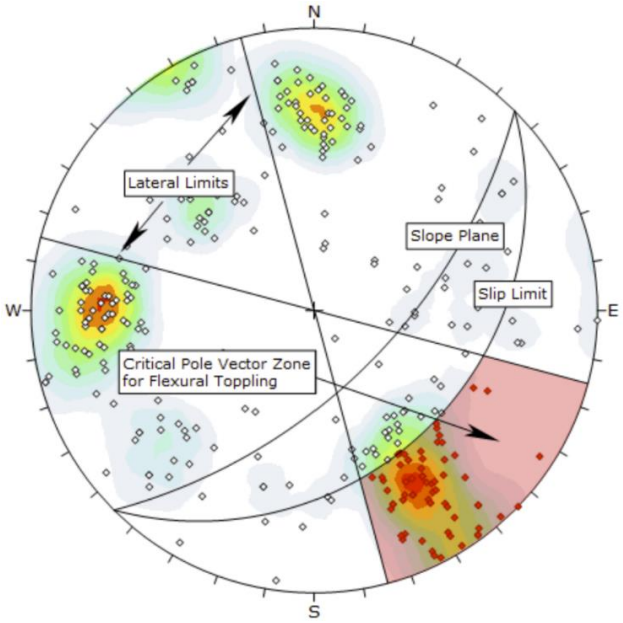

Figure 15. Flexural Toppling kinematic analysis (Rocscience, 2023).

(3) Block-Flexural Toppling: Characterized by continuous flexure occurring along large columns divided by multiple cross joints i.e., involvement of both flexural and block toppling mechanisms. Failure occurs as a result of accumulated displacements on the cross-joints (Wyllie & Mah, 2004).

3 MINE BACKGROUND

Kevitsa is an operating, large-scale Ni-Cu-PGE open pit mine, located approximately 140 km north of the Artic Circle in the Municipality of Sodankylä, in which the main town is reached by road 41 km to the south-west, and the nearest village Petkula is located 8 km to the west of the mine property. A location map is presented in Figure 16.

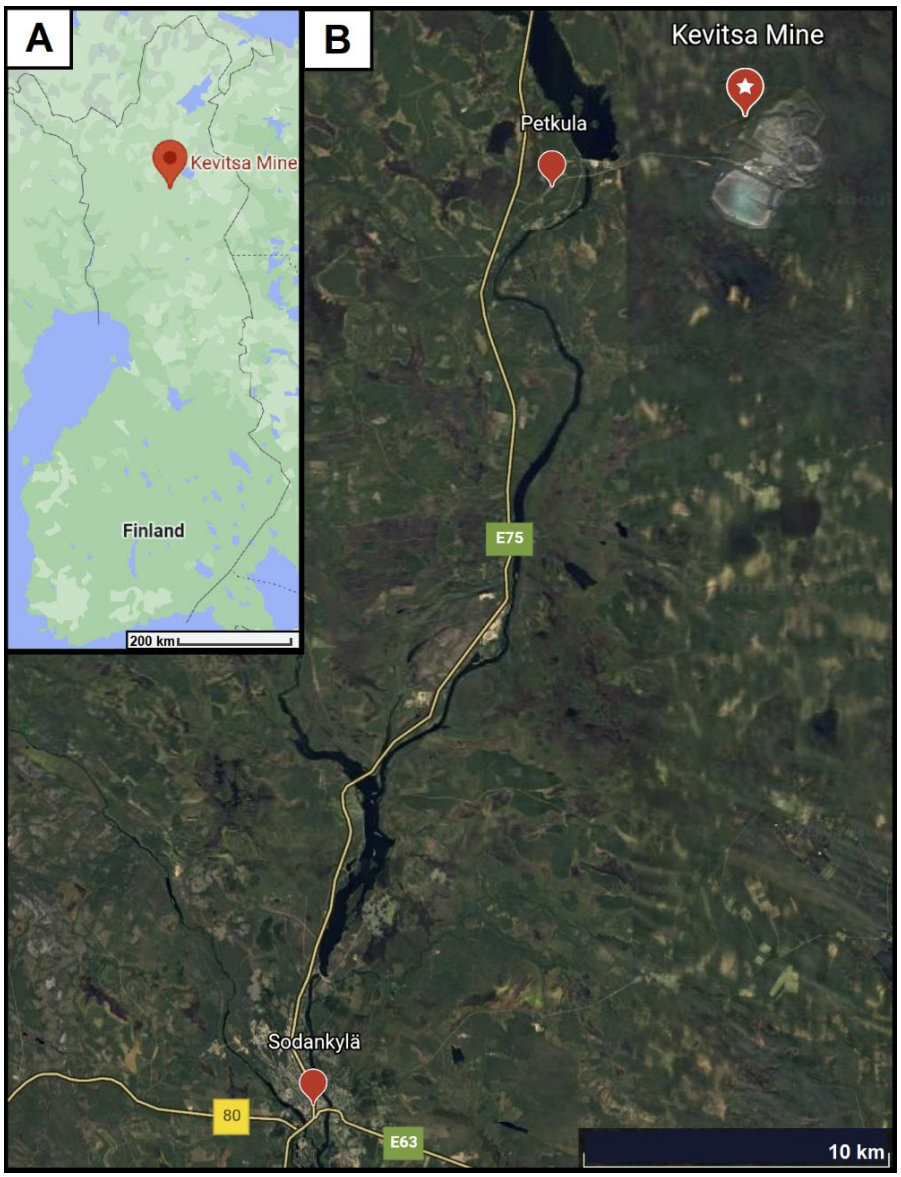

Figure 16. (A) Location of the Kevitsa mine in Finland. (B) Location of the Kevitsa mine in Sodankylä.

Exploitation of the Kevitsa deposit started in 2012, where mining operations were initiated by First Quantum Minerals (FQM) who were the previous owner before Boliden was purchased the mine in 2016 (SRK, 2019). Since then, the mine production of the Kevitsa Mine has increased yearly, achieving total values of 73.59 Mt and 257.59 Mt for ore and waste production respectively by 31 December 2021 (Berthet, 2021).

3.1 Regional Geology

The Kevitsa igneous complex is hosted in the Central Lapland Greenstone Belt (CLGB) (Figure 17), which is a Paleoproterozoic volcano-sedimentary sequence that forms one of the largest known Paleoproterozoic greenstone belts. It covers an area of roughly $35000km^2$ that extends from Norway through Finnish Lapland to the western part of Russian Karelia (Niiranen et al., 2014; Hanski & Huhma, 2005).

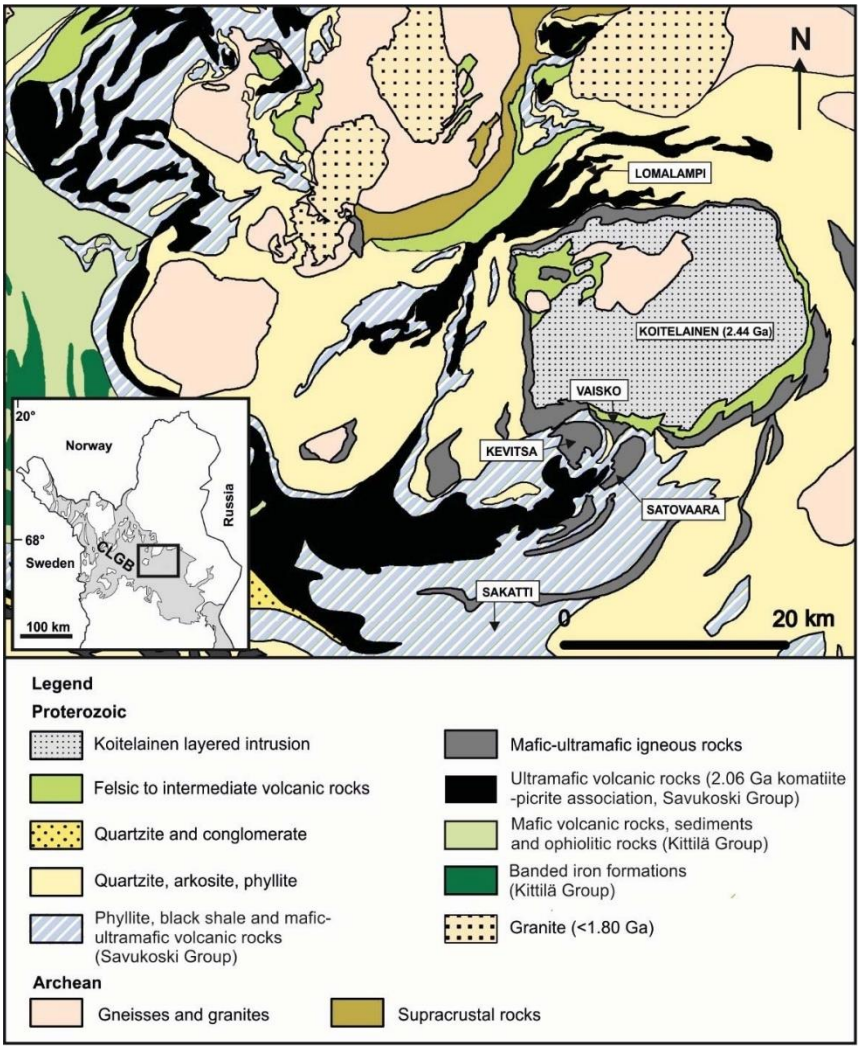

Figure 17. Location of the Kevitsa intrusion in the Central Lapland greenstone belt (CLGB) (Luolavirta et al., 2017).

The CLGB is recognized to be a highly prospective area for magmatic ore deposits, where the ore occurrences in northern Finland share multiple features with others Paleoproterozoic greenstone belts globally (Eilu et al., 2007).

The CLGB is subdivided into seven stratigraphic groups, described from oldest to youngest as: Salla, Onkamo, Sodankylä, Savukoski, Kittilä, Lainio, and Kumpu (Räsänen et al. 1996); which have undergone through multiple episodes of folding and thrusting (Lappalainen & White, 2010). The Savukoski Group, which hosts the Kevitsa intrusive

complex, represents a major marine transgression dominated by supracrustal rocks, black schists, phyllites, tuffites, mafic metavolcanics, and the uppermost unit of ultramafic volcanics (Lappalainen & White, 2010). A minimum age of 2060 Ma has been determined for the Savukoski Group pelitic metasediments from the crosscutting ultramafic intrusive bodies (Mutanen & Huhma, 2001). In addition to the Kevitsa intrusion, other noteworthy magmatic deposits have been discovered in the volcano-sedimentary sequence of the Savukoski Group such as the Sakatti Cu-Ni-PGE deposit and the komatiite-hosted Lomalampi PGE-(Ni-Cu) deposit (Brownscombe et al., 2015; Törmänen et al., 2016).

3.2 Local Geology

The Kevitsa intrusion (Figure 18) is a layered, mafic-ultramafic complex dated at 2058 ± 4 Ma (Zircon U-Pb geochronology), hosted within a deformed greenschist-facies volcano-sedimentary sequency (Mutanen & Huhma, 2001).

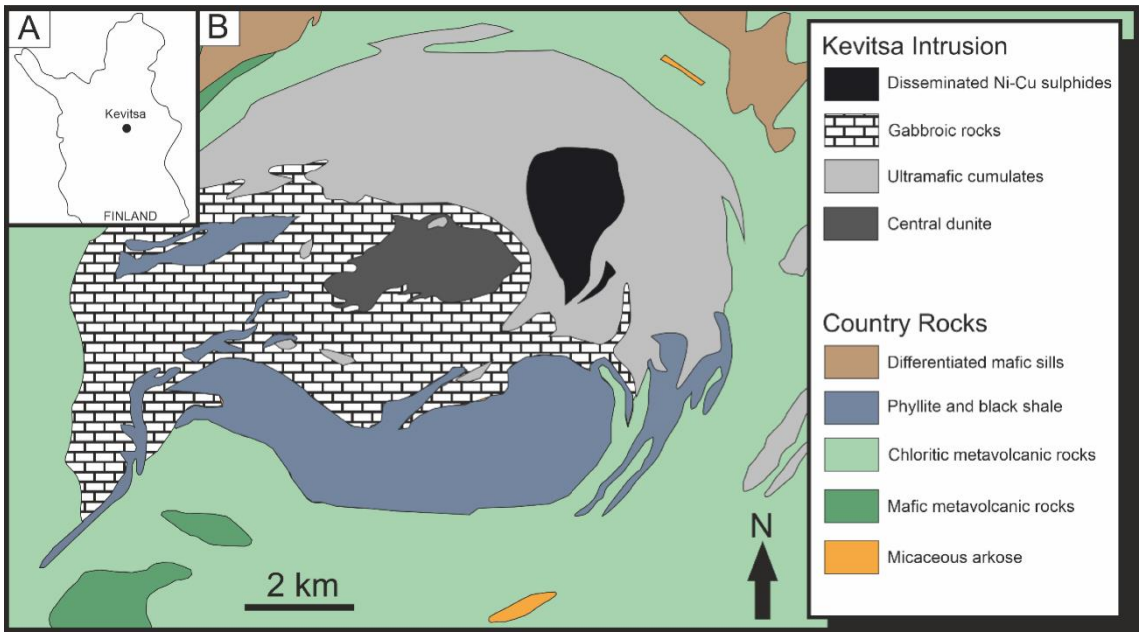

Figure 18. (A) Location of the Kevitsa intrusion in Finland. (B) Geological map of the Kevitsa intrusion (McDonald, 2020).

The body of the intrusion extends to about 2 km in depth, consisting mainly of gabbros, pyroxenites, olivine websterites, and clinopyroxenites; which are surrounded by supracrustal rocks such as mafic volcanics, phyllites and carbonaceous schists. The general stratigraphy of the intrusion consists of gabbroic rocks at the top, which are located to the South-west side of the underlaying ultramafic units. Dunite bodies are also found in the middle of the deposit and in the bottom of the intrusion which are discordant to the magmatic layering (Berthet, 2021; Gray et al., 2016).

The Kevitsa area has undergone several tectonic and metamorphic events which are evident in the intrusion and in the country rocks (Hölttä et al. 2007). A key feature of the area is the NNE-SSW trending Satovaara Fault and its associated structures which have deformed the eastern margin of the Kevitsa Intrusion (Gray et al., 2016). Metamorphism episodes have modified the rocks mineralogy, in which amphibole alteration of ferromagnesian minerals such as olivine, orthopyroxene, and clinopyroxene is very common and overprints the majority of the Kevitsa mineralization. Other alteration minerals include chlorite, serpentine, carbonate, talc, and epidote, from which the last two have been identified to be associated to late fractures and veins (talc), and faults and shear zones (epidote) (Gray et al., 2016).

3.3 Structural Model

Since the beginning of open pit mining at Kevitsa, multiple studies with varying approaches have been developed to characterize structural features such as faults, joint sets, alteration zones, weakness zones, geotechnical domains, and potential instabilities. These have been developed internally, and by various consultants, where results point out distinct structural orientations for major and minor structures, as well as weakness zones that comprise brittle deformations and/or alteration zones (Pabst, 2023). Further details about the previous models can be found in Jigsaw (2009), WSP (2014 and 2015), and Booth (2015).

The latest structural models (2018, 2020, and 2023) were produced by the Kevitsa Mine Geology Department to review the large-scale structures, and understand their control in the lithology, mineralization, and alteration of the intrusion.

The structural models from 2018 and 2020 mainly focused on diamond core images, and an additional interpretation of the pre-mining topography, 3D photogrammetry, Sirovision mapping, and X-ray Diffraction (XRD) mineralogy. These models were updated in 2023 with new structural data acquired by diamond drilling, acoustic televiewer logging, 2D seismic survey, pit photogrammetry, rock falls interpretation, and the initial results of the present kinematic study.

The following subsection summarizes the interpreted structures from the Kevitsa Structural Interpretation 2023 (Pabst, 2023), which are considered for the structural interpretation and kinematic analysis of this study.

3.3.1 Major Structures

(1) NE trending faults

The NE trending faults are regional structures of high confidence. They are indicated by pre-mining topography lineations, seismic profiles, and drillhole interpretations (geochemistry and brittle deformation).

NE-flt-rv1: Defined as a continuous "band" and modelled as a thin vein, fault RV1 (Figure 19) is modelled according to thick core intervals (1.5-2m) of dense fractured rock which are found in zones that matched elevated concentrations of talc and sulphide.

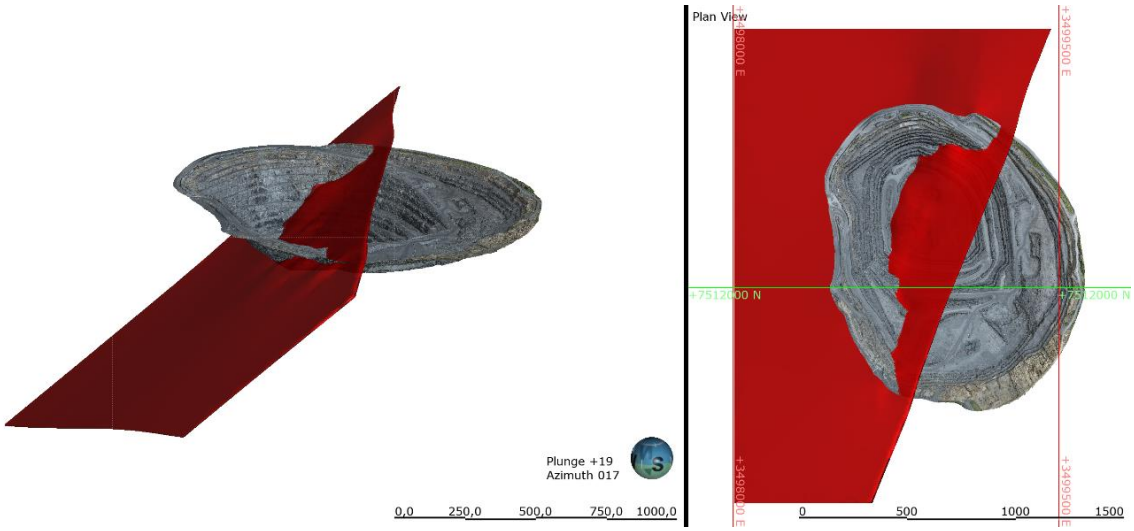

Figure 19. Fault NE-flt-rv1 in the 3D view of the 2022 photogrammetry pit.

NE-flt-2_014: Previous interpretations were based on brittle core fracturing, filled veins, and spatially random talc enrichment. In 2023 the structure was re-interpreted (Figure 20) following a larger wedge failure that exposed a wall face / joint surface not previously visible; and further re visiting of drillholes around the area.

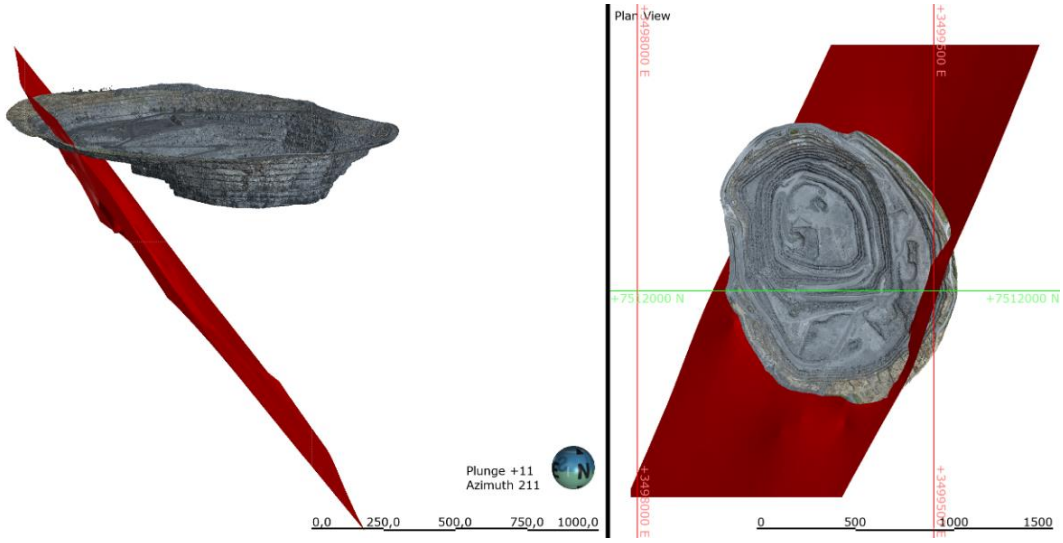

Figure 20. Fault NE-flt-2_014 in the 3D view of the 2022 photogrammetry pit.

(2) EW trending faults

EW-flt-1_001: Interpreted in 2018 and 2020 in the eastern part of the pit as a strongly fractured and sheared fault recognizable in drill core. The fault exposes a weathered lineation in the pre-mining topography. In 2023 the fault was found to have a low diopside concentration, and a joint set with similar orientation. Terminated against NE-flt-1_014 and NE-flt-rv1 (Figure 21).

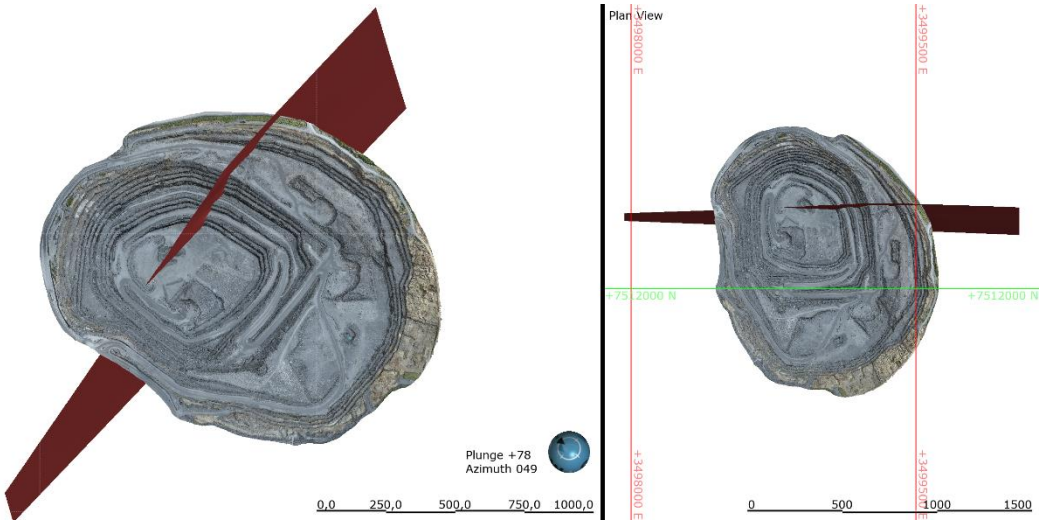

Figure 21. Fault EW-flt-1_001 in the 3D view of the 2022 photogrammetry pit.

(3) ENE trending regional faults

ENE-flt-1_012: Fault ENE-flt-1_012 surface (Figure 22) had been modelled using traces in the east and south pit walls in 2018, with no clear traces in the southern pit wall. The 2023 review suggests that at a regional scale the fault appears to separate two 'Ni-S-PGE-rich' mineralization domains and its orientation is similar to regional trends from geophysics. The fault could be terminated against NE-flt-rv1 and be a local expression.

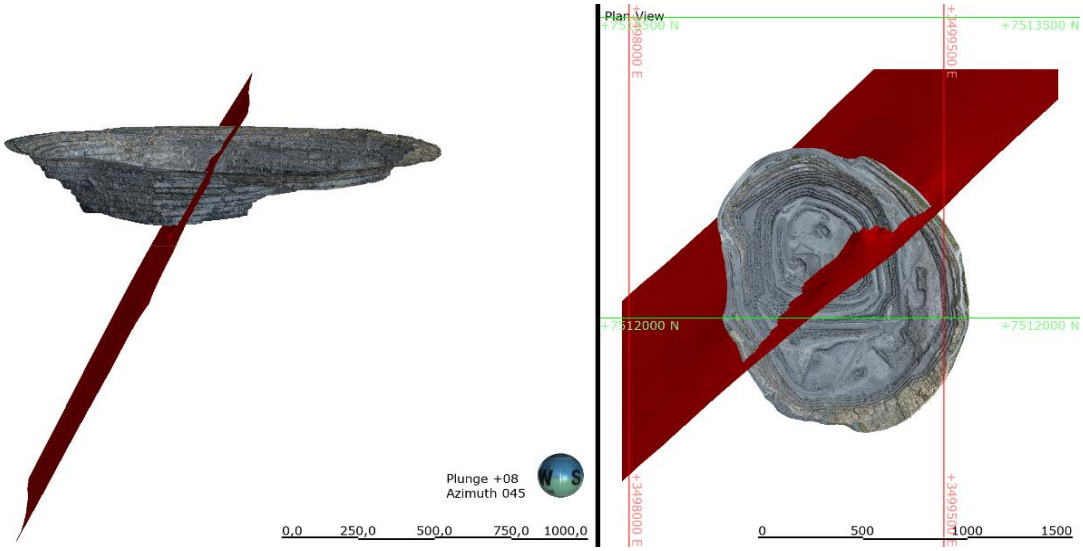

Figure 22. Fault ENE-flt-1_012 in the 3D view of the 2022 photogrammetry pit.

(4) NS trending dykes and faults

NS-flt-1_002: Initially modelled using assays and XRD mineralogy, characterized by near vertical dolomitic (massive to mélange like to fractures) veins. No real evidence is observed in pit photogrammetry in forms of dyke/veins/joints/fault. Modelled in 2023 (Figure 23) as a thin zone, up to several decimeters.

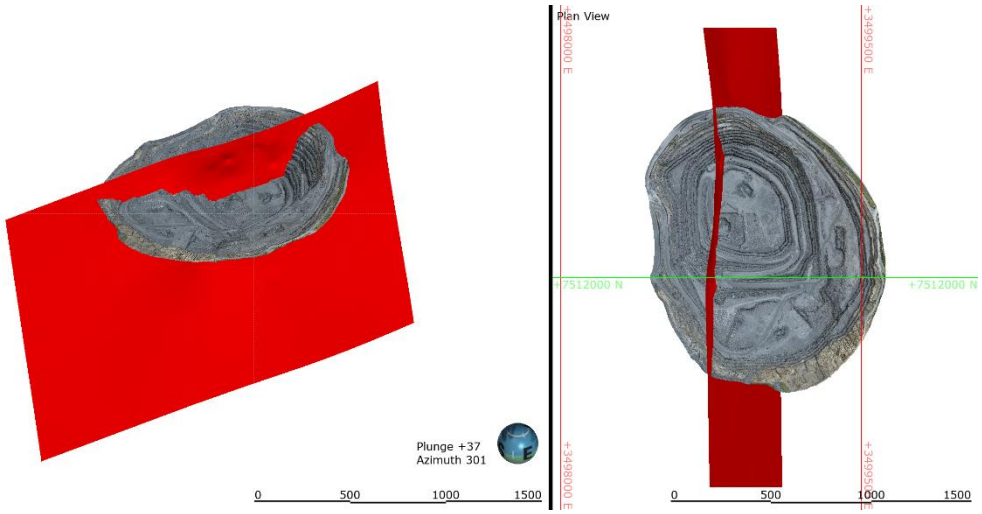

Figure 23. Fault NS-flt-1_002 in the 3D view of the 2022 photogrammetry pit.

NS-flt-2_009: Interpreted following high talc XRD signatures, and near-vertical dolomitic and talc-rich pegmatite-dyke-like veins in drill core. Structure is well visible in the pre-mining surface, orthophoto, pit walls, and in drill core (Figure 24).

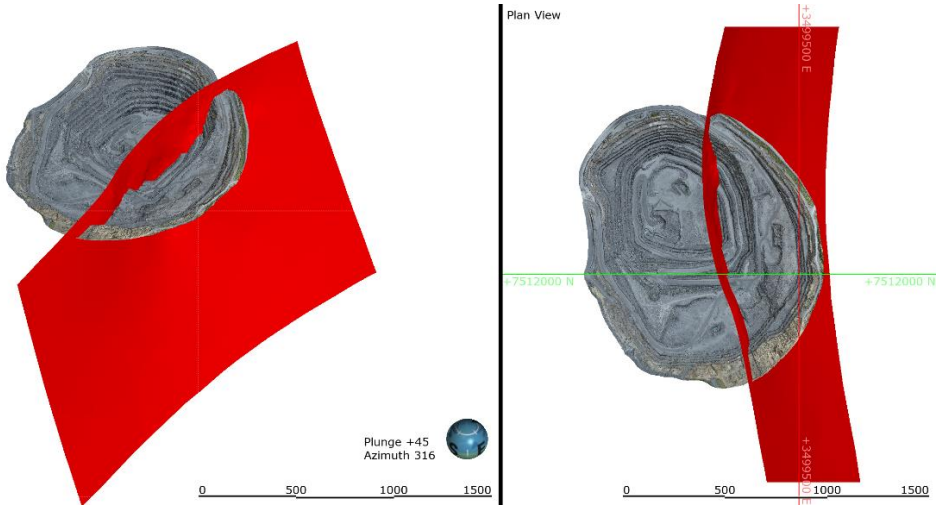

Figure 24. Fault NS-flt-2_009 in the 3D view of the 2022 photogrammetry pit.

NS-flt-3_010 and splay: Fault NS-flt-3_010 is defined as a near vertical partly dolomitic pegmatite-dyke-like, which is steeply dipping and nearly NS striking. True thickness of the dyke varies from 10cm to less than 50cm. Geochemistry (talc, magnetite, low diopside) suggests at least one splay modelled as Splay off flt_010 (Figure 25).

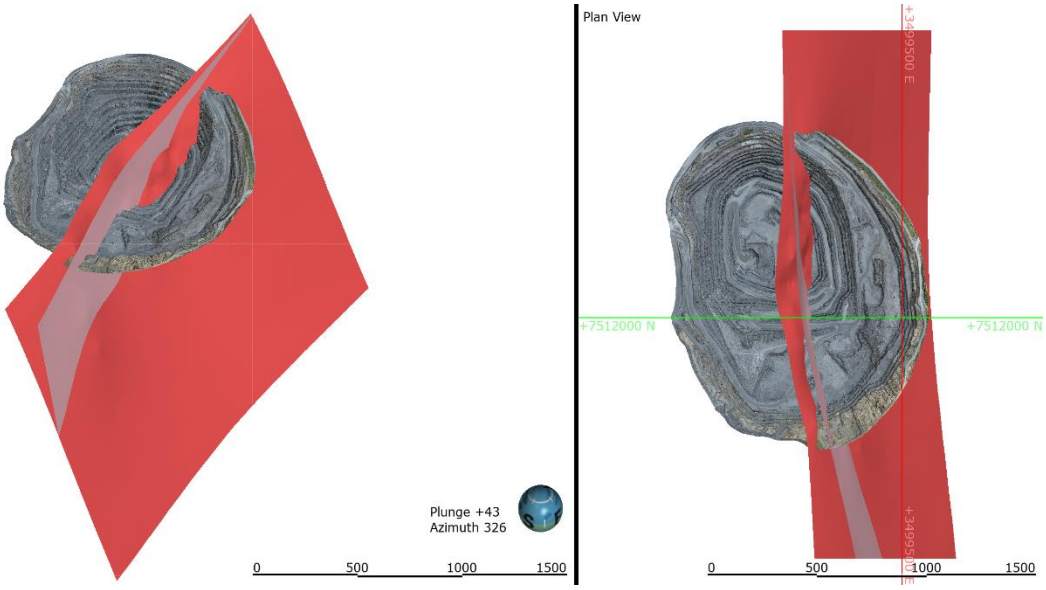

Figure 25. Fault NS-flt-3_010 (red) and Splay (pink) in the 3D view of the 2022 photogrammetry pit.

NE-flt-5_019: The interpretation of NE-flt-5_019 in the 2018 review defines it as a NS trending steeply dipping fault located in the west of the deposit (Figure 26), which is subparallel to other NS trending dykes and faults (suggested by often brittle shear zone characteristic). The 2023 review suggests that the fault does not exist as a vein or fault as no geochemical or structural evidence could be identified with confidence. However, its complete existence is not discarded, and an additional review is suggested.

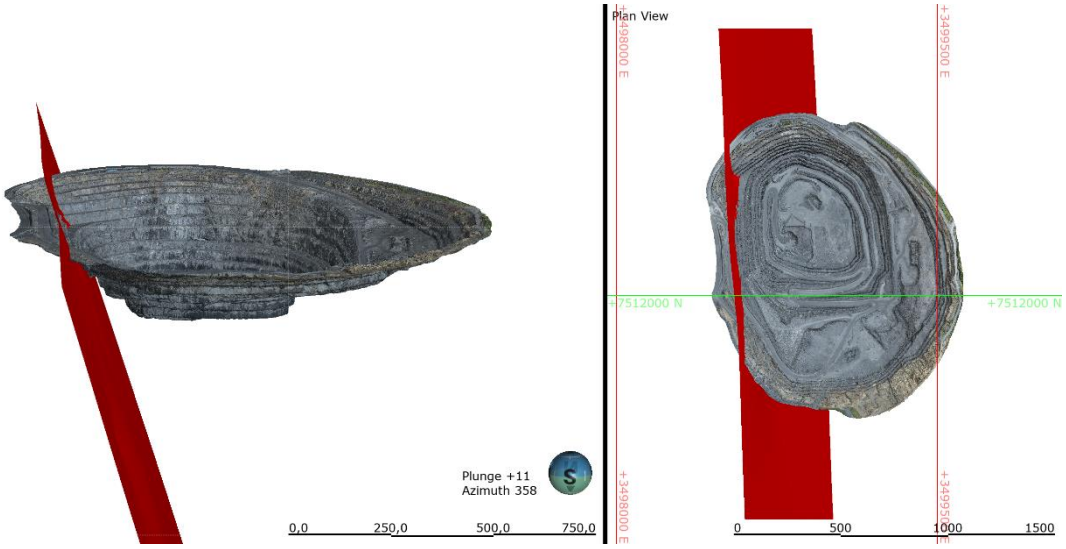

Figure 26. Fault NS-flt-5_019 in the 3D view of the 2022 photogrammetry pit.

3.3.2 Minor Structures

NE trending joints, steeply SE dipping: A major joint set with an orientation of roughly 80/140 was identified through the entire pit area using 3D photogrammetry and in drill core during 2023.

Structure NE-flt-3_018, previously interpreted as a fault, was suggested to be part of this joint set during the 2023 structural interpretation. This is because previous interpretations on drill core were not indicative enough to call this structural feature a local fault. Figure 27 shows the tendency in spacing and persistence of the joints.

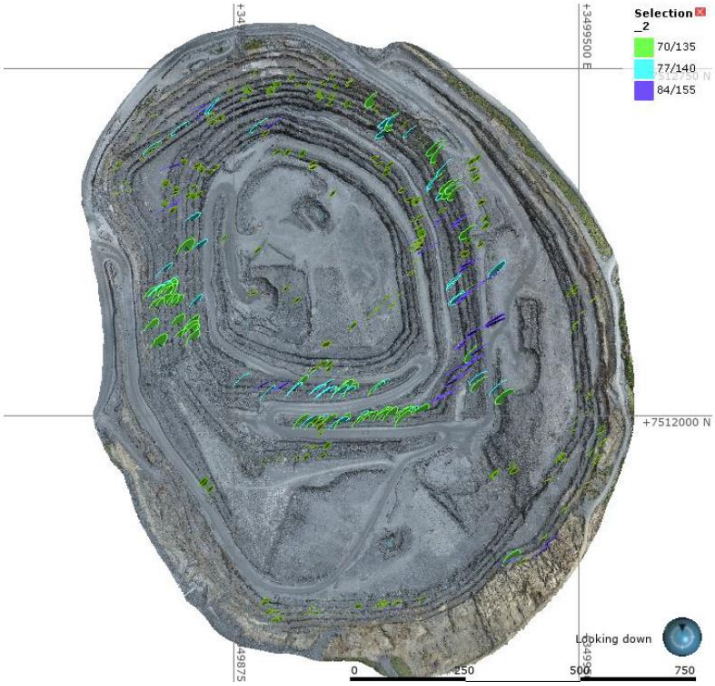

Figure 27. NE trending joints, steeply SE dipping in the plain view of the 2022 photogrammetry pit (Pabst, 2023).

NW trending joints, steeply SW dipping: A major joint set with an average orientation of 80/220 was identified during 2023 (Figure 28) through a review of Sirovision mapping, photogrammetry pit plane picks, and core structures.

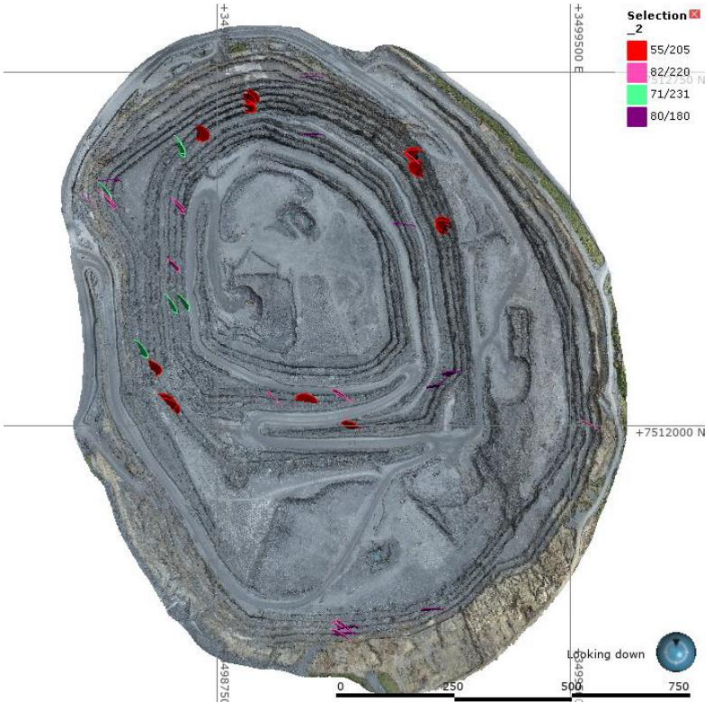

Figure 28. NW trending joints, steeply SW dipping in the plain view of the 2022 photogrammetry pit (Pabst, 2023).

Structure NW-flt-1_005, previously interpreted as a fault, was suggested to be part of this joint set during the 2023 structural interpretation. A review of the location of the previous modelled meshes did not show any evidence to suggest its existence.

NNW trending joints, near vertical: A major joint set with an average orientation of 80/70 (Figure 29) was observed throughout the deposit in 2023, which shared the orientation with the previous interpreted fault NNW-flt-1_003. Due to the low confidence of the fault as no evidence in historical orthophoto and geochemistry was seen, the fault was suggested to be part of the joint set.

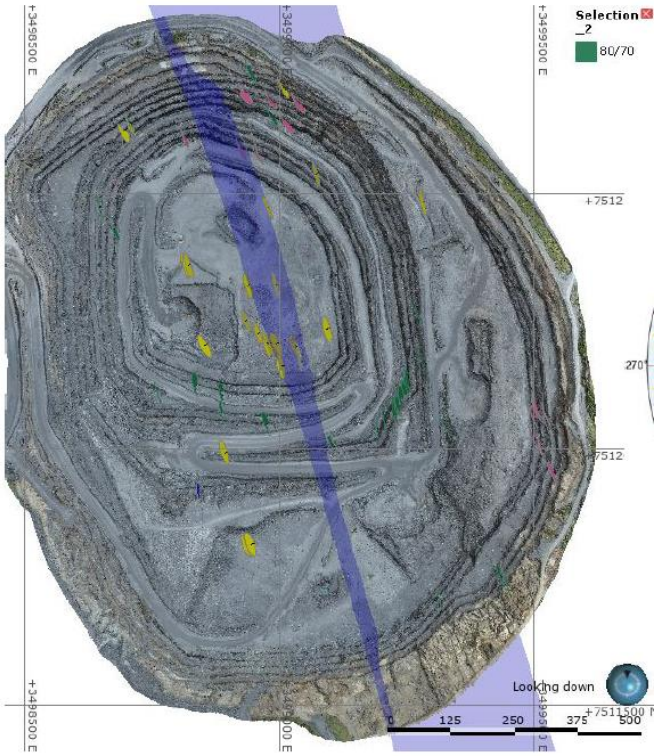

Figure 29. NNW trending joints, near vertical, with NNW-flt-1_003 (in blue) in the plain view of the 2022 photogrammetry pit (Pabst, 2023).

WNW trending joints, shallowly NNE dipping: In the 2018 structural interpretation, the structures WNW-flt-1_008 and WNW-flt-2_020 were interpreted as faults using drill cores with minor indication from pit photogrammetry. They had been defined as brittle fractures of limited lateral extent. However, no talc enrichment was observed, and in numerous drill holes quartz-rich or calcitic veining was used as the "fault location" due to no other evidence.

The 2023 review of photogrammetry and drill core logging suggests that the two features could be part of a wider spaced joint set (Figure 30) that is visible through the entire deposit with an average orientation of 35/40.

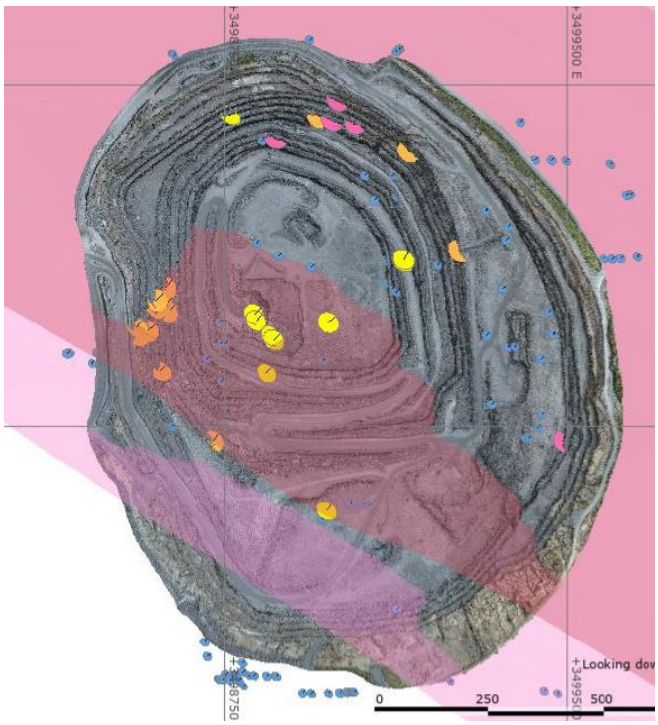

Figure 30. WNW trending joints, shallowly NNE dipping, with WNW-flt-1_008 (pink) and WNW-flt-2_020 (red) in the plain view of the 2022 photogrammetry pit (Pabst, 2023).

NS trending joints, steeply E dipping: A major joint set with an average orientation of 60/95 (Figure 31) was observed throughout the deposit in 2023, which had been previously identified in diverse structural interpretations (WSP, 2014). This joint set was found to share the orientation with structure NS-flt-4_015, which had been interpreted with no geochemical signature and just occasional pit wall joint planes in the north. The 2023 interpretation suggested that the structure makes part of a NS trending joint set which is steeply E dipping.

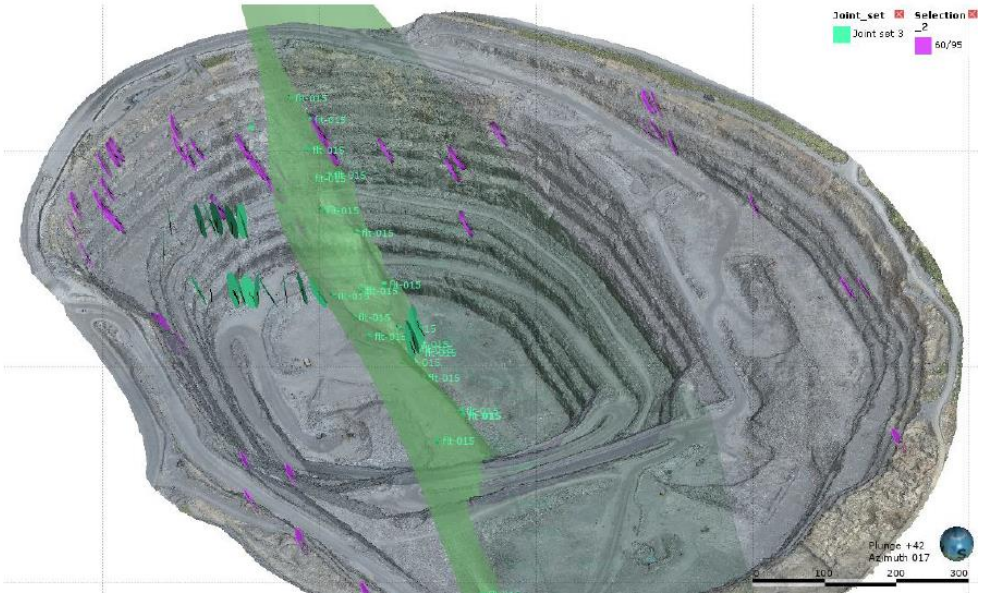

Figure 31. NS trending joints, steeply E dipping, with fault NS-flt-4_015 (green) in the 3D view of the 2022 photogrammetry pit (Pabst, 2023).

3.4 Inferred Palaeostresses of the Kevitsa Structures

The most recent genetic models proposed for the brittle structures and fracture zones of the Kevitsa deposit were developed by Lindqvist (2017) and are shown in Figure 32.

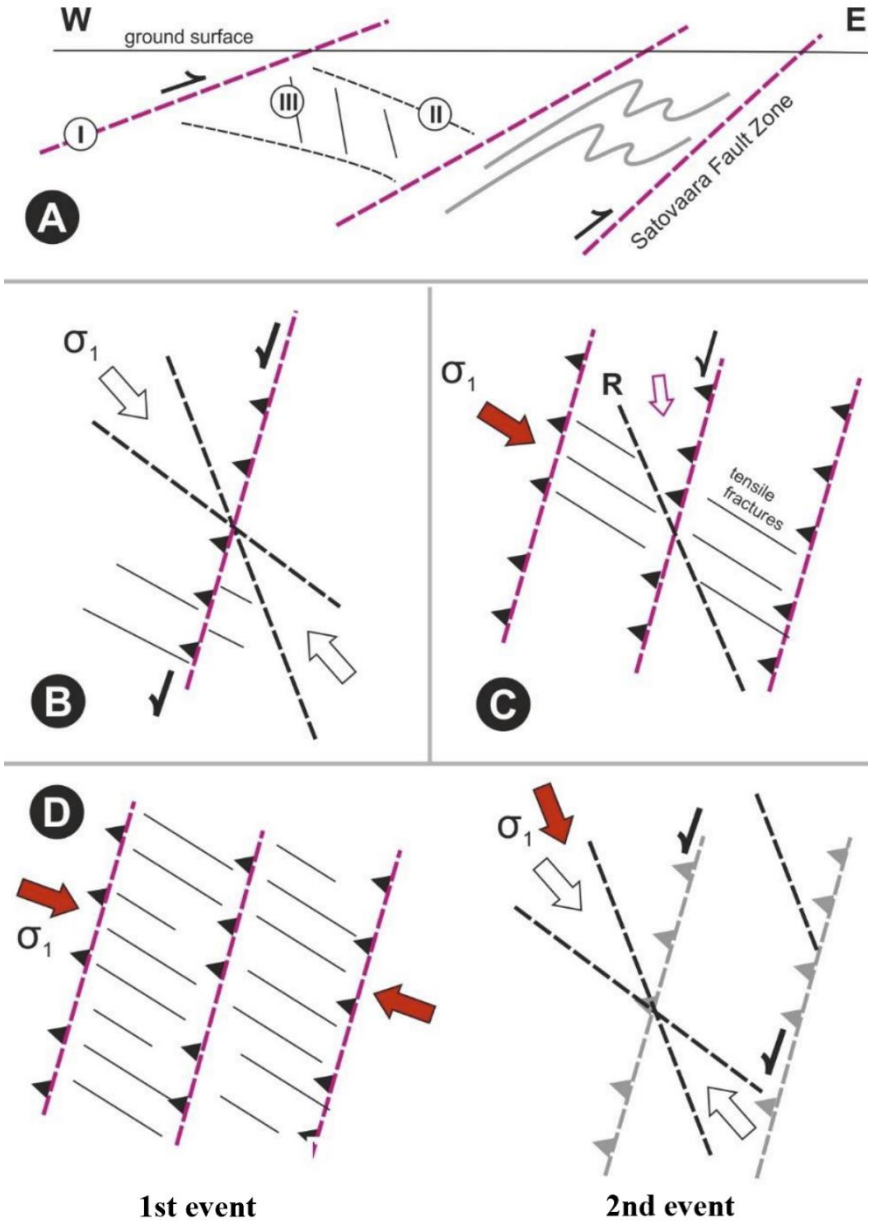

Figure 32. Inferred fault network arrangements and palaeostress scenarios proposed for the Kevitsa structures (Lindqvist, 2017).

The first scenario is described by: (A) A WNW-ESE vertical section illustrating the network of first, second, and third order structures; (B) Left-lateral transpressive deformation with a NW-SE compressive component, developing major WNW-dipping reverse faults, and secondary shear structures; and (C) NW-SE transpression resulting in WNW-dipping dip-slip zones and tensile fractures. Second scenario (D) proposes two separate tectonic events, consisting of a WNW-ESE compressional stress resulting in WNW-dipping structures, followed by an NNW-SSE rotational field stress.

3.5 Mining Methods

The Kevitsa mine is a conventional, moderate-size open pit mining operation using pit truck and shovel, preceded by drilling and blasting followed by stockpiling and waste dumping. BKMOY owns a mining fleet and uses contractors to assist ore re-handling on the run of mine (ROM) pad for primary crusher feed (Grey et al., 2016). The Kevitsa mine started mining operations in autumn 2011, when Hartikainen was contracted to mine waste from stage 1. Mining has proceeded from initial excavation: stage 1 and stage 2 have been mined out and stage 4 mining has started in 2019. An additional strategic project was held during 2022 to revise the life of the mine with the feasibility of a possible expansion to an additional pushback, stage 5 (Berthet, 2021).

According to Grey et al. (2016) the mining sequence broadly follows the sequence of events:

(1) Grade control RC holes delineate the ore zones.

(2) Blast patterns are designed to reduce material throw and ore dilution. A Blast Master planning process controls the sequence of operation.

(3) When possible, ore and waste are blasted and mined separately as fragmentation requirements vary significantly. Blast movement monitoring is in place to minimize dilution and ore loss for mixed blasts.

(4) Waste removed on each 12 m bench prior to the mining of ore, removal of waste in the successive cutbacks utilizes planned bulk systems of operation.

(5) Trim blasts and perimeter blasting utilized to ensure pit wall profiles are cut to the correct angle and wall damage minimized.

(6) Face shovels load rocks into 225 t class trucks. Ore is hauled from the pit to the finger stockpiles. This is an integral part of the feed sequence as it ensures that ore blending can be achieved, haulage efficiencies can be maximized, and operational flexibility is enhanced at all times.

4 METHODOLOGY

4.1 Sectorization of the Stage 5 design

The present study follows the methodology developed by WSP (2014, 2015) for the kinematic analyses of stages 1 to 4 of the Kevitsa open pit mine. The approach evaluates the risk of structural failure in the planned open-pit stages according to sectors defined by the pit wall orientations. The goal of this approach is to analyze if the dominant joint sets vary across the mine, and if the observed discontinuities together with the proposed excavation slopes create unfavorable conditions where the slopes can fail along the discontinuity surfaces or pair of intersecting discontinuities.

The sectorization and modelling of the study was carried out in LeapfrogGeo 2021.2.5 (Seequent limited) using the mesh surface "Stage5_V1B (2) - 3. PIT DESIGN_STAGE DESIGN SURFACE_E" (Figure 33) which is the latest design generated for the Stage 5.

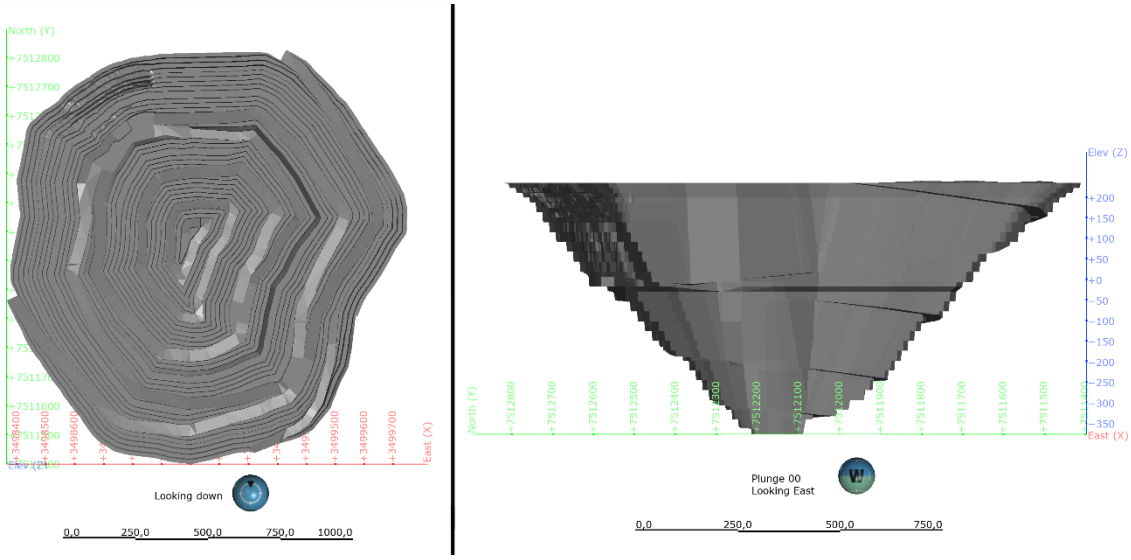

Figure 33. Stage 5 design of the Kevitsa open pit mine.

Six predominant slope orientations were identified from the mesh surface, defining six sectors and/or main pit walls of the Stage 5 design (North, North East, North West, South, South West, and South East walls). These were additionally corroborated by measuring the orientation of multiple bench faces throughout the pit. To constrain the structures from each sector, a geological model was constructed using fault surfaces as boundaries between the pit walls. This model incorporated a distance function in the output volumes to control the structures considered according to their distance to the mesh surface of the Stage 5 design. The output volumes use different color "lithologies" to create differentiation (Figure 34).

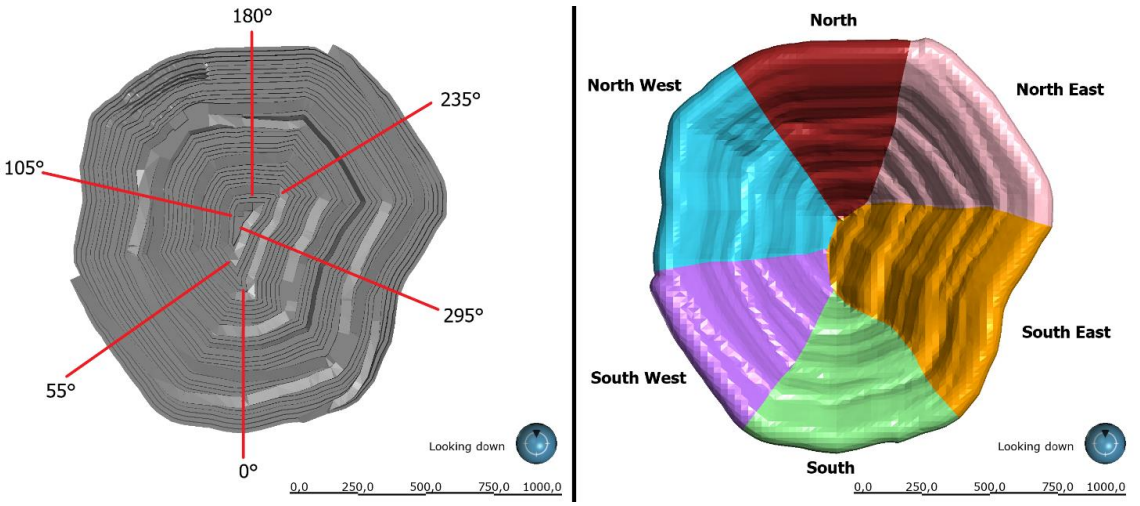

Figure 34. Main slope orientations of the Stage 5 design (left). Output volumes of the designated sectors using a 50m distance function (right).

It should be highlighted that defining the sectors for the study recognized an inter-ramp slope in the upper Northwest corner of the pit, which has already been reached by the current mine layout (Figure 35). As the orientation of this slope highly differs from the orientation of the proposed excavation slopes of the Stage 5, it was assigned partially to the North West and North walls. The slope is considered during the analyses using kinematic sensitivity ranges (bench scale) and treated individually (inter-ramp scale).

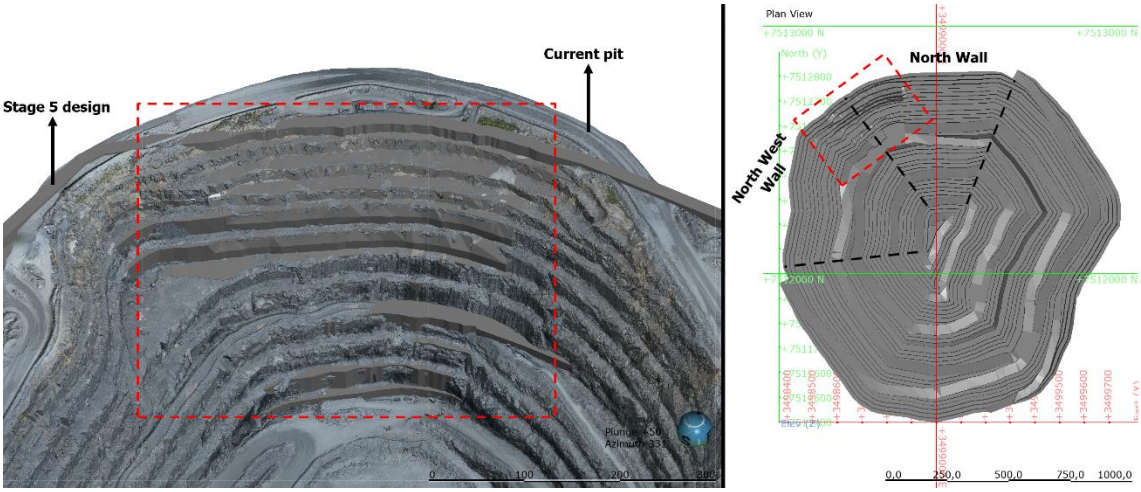

Figure 35. Designation of inter-ramp slope to the North West and North walls (right). Comparison of inter-ramp slope in Stage 5 design vs Current pit (left).

4.2 Compilation of Structural Data

A key objective of the study was to characterize the minor and intermediate discontinuities of the Kevitsa deposit, because they are the main inputs for the kinematic analyses at bench and inter-ramp scale. Therefore, structural data were collected from three different sources representing different sampling strategies. The data compiled forms a comprehensive database that establishes a relationship between the structural features at depth and at surface.

4.2.1 Structural Mapping from 3D photogrammetry

Photogrammetry mapping was performed to collect structural data from the pit walls of the mine, which corresponds to a planar sampling technique that provides information about the structural features at surface. As the kinematic analyses are aimed to evaluate the final layout of the future Stage 5, the structural mapping was limited to areas within a 200m distance to the actual Stage 5 design mesh (Figure 36).

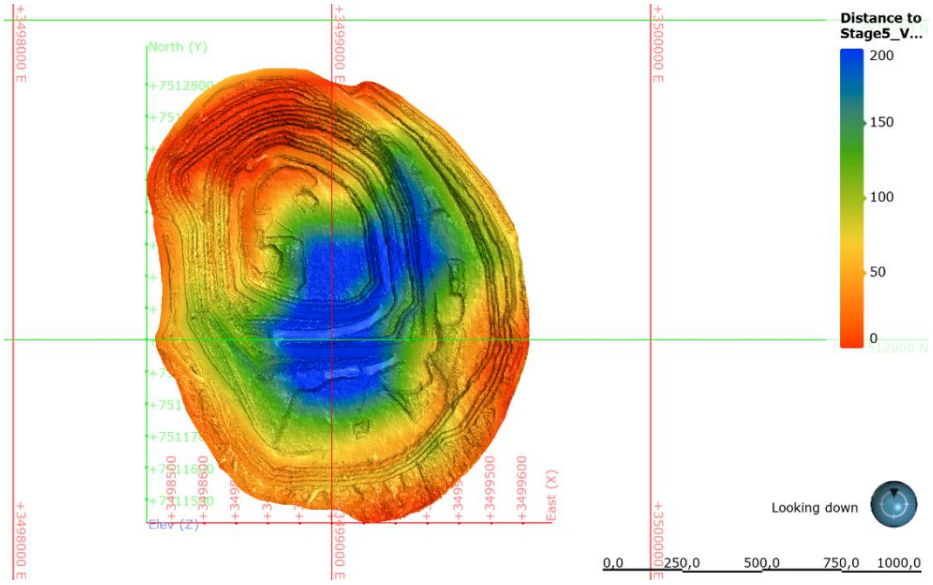

Figure 36. 3D view of the 2022 photogrammetry pit displayed according to its distance to the Stage 5 design.

The latest 3D pit photogrammetry available was used to measure structural planes from the pit walls using LeapfrogGeo, which corresponds to the "Kevitsa 2022-06 Photoscan deliverables" provided by Fractuscan in 2022. The procedure for data collection is shown in Figure 37, which involves identifying structural planes that corresponded to natural fractures, and must be carefully differentiated from blast walls. A measure of the structural plane is then taken by drawing a disk with the same orientation of the plane.

Figure 37. Procedure for measuring structural planes in LeapfrogGeo 2021.2.5

A total of 1440 structural planes were measured from the photogrammetry mapping. This were compiled with an additional 745 measurements previously made by Sonja Pabst (Resource Geologist Specialist) making a total of 2185 used in the kinematic analyses. Their location is presented in Figure 38.

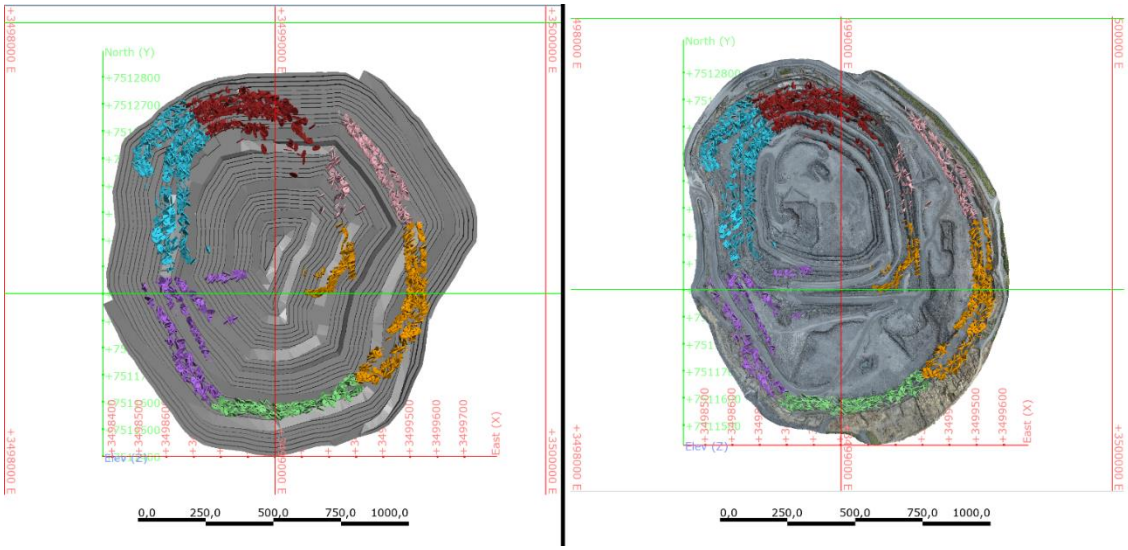

Figure 38. Upper view of Structural data compiled from 3D photogrammetry by sectors colors in: Stage 5 design (left), Pit photogrammetry of 2022 (right).

4.2.2 Selection of Structural Data Acquired through Drill Core Logging

The diamond-drill core logging database from the Kevitsa mine was used to obtain structural data at depth, as it corresponds to a linear sampling technique that collects information of the rocks from the sub-surface. From oriented structures, only those logged as "JT / joint – undifferentiated" were considered, as they represent open, near open, and healed rock joints. These were additionally filtered to select only the structures measured with high confidence in the orientation quality (HC), located within a 50m distance to the Stage 5 mesh. The initial filtering limited the number of structures to 8052 measurements from 137 different drill cores. However, it was recognized that there was a significant discrepancy in the number of rock joints present in each sector. To address this and ensure a more even distribution of data around the pit, filtering parameters were added and/or modified according to the data available in each sector.

To limit the high number of joints in the North, North East, North West, and South Eastern sectors, the structures were filtered according to the Joint alteration number (Ja) and Joint roughness coefficient (JRC) designated during logging. This criterion was selected to highlight potential failure joints. In contrast, the amount of high confidence structural data from the Southern sector was significantly lower in comparison to the other sectors. This required that the range of distance between the structural data from the Southern sector

and the Stage 5 design mesh surface was extended to 100m. A dataset of 5061 rock joints logged from 124 drill cores was then generated.

Furthermore, as the drill cores had been logged by multiple geologists over time, a systematic review of the corresponding core photos was made, where every 10 structures and/or every 20 meters (whatever happened first) a JT measure was checked to verify if it corresponded to a rock joint. An example of the structures is presented in Figure 39.

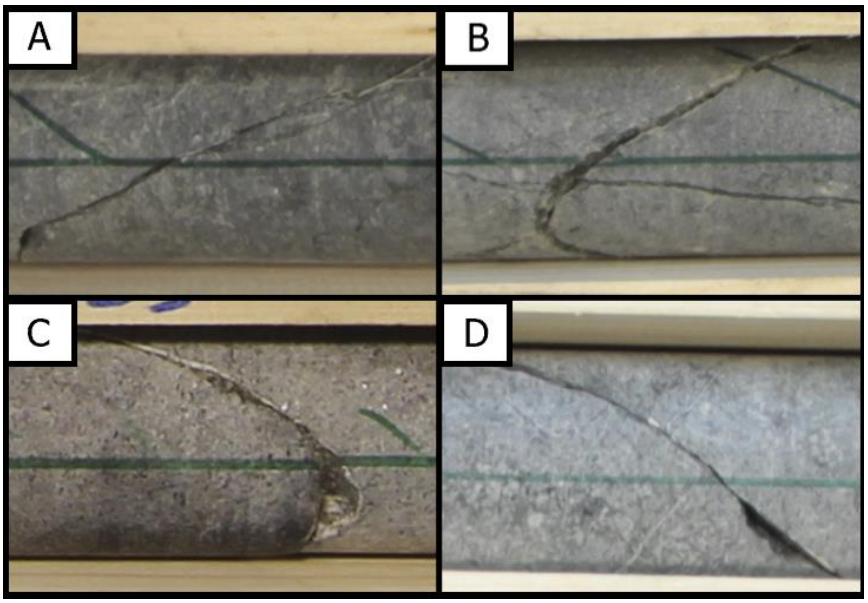

Figure 39. Core photos of structures logged as JT. (A) Drill core KEV17027; (B) Drill core KEV18002; (C) Drill core KEVX19015; (D) Drill core KEVX19020.

Conclusively, a definitive dataset for the diamond drill core data was generated, compiled in the Excel CSV file "DD_structural_data_kinematics_Stage5". Table 3 presents the characteristics of the data according to each sector.

Table 3. Characteristics of structural data compiled from diamond drill core logging.

SECTOR	FILTERS	DISTANCE OF DATA TO STAGE 5 MESH	# OF JOINTS
North	JA>=2	<50M	1030
North East	JA>=2	<50M	822
North West	JA>2	<50M	826
South		<100M	834
South East	JA>=2, JRC<2	<50M	871
South West		<50M	678
Whole Pit			5061

Figure 40 exhibits the distribution of the structural data compiled from the diamond drill core logging records in the Stage 5 mesh surface.

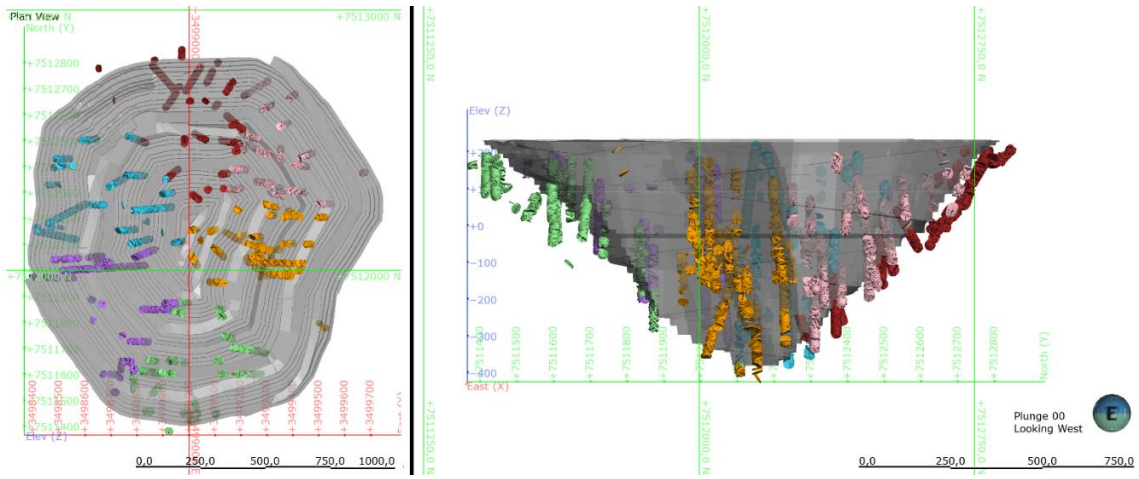

Figure 40. Structural data compiled from diamond drill core logging records by sectors colors in the Stage 5 design.

4.2.3 Selection of Structural Data Acquired through Televiewer Logging

The structural data collected by Sonja Pabst from ATV logging of drill holes KEV22001, KEV22002, KEV22003, and KEV22004 was used for the kinematic analyses of the study. Similar to the diamond drill core logging data, the structural data corresponds to sub-surface data obtained from a linear sampling technique. As the data is intended to characterize the rocks at depth, only the fractures located within a 50m distance to the Stage 5 design mesh were considered. This resulted in a dataset of 303 measurements from the North, North East, and North West sectors (Figure 41).

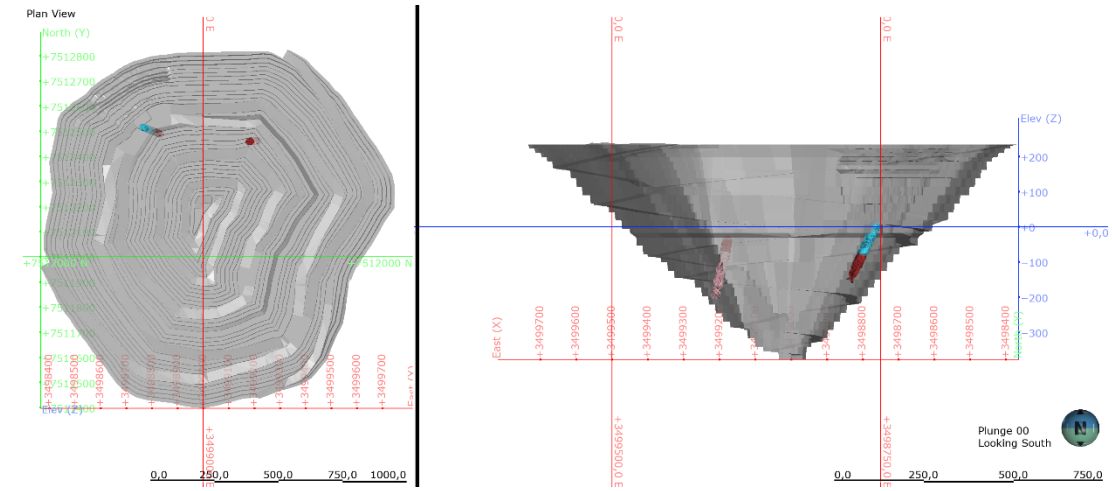

Figure 41. Structural data compiled from ATV logging records by sectors colors in the Stage 5 design.

4.3 Identification and Structural Interpretation of Joint Sets

After the datasets from each source are defined, the rock joints measurements were plotted in terms of dip/dip direction using Stereonet Plots in Rocscience DIPS. The data was grouped into discontinuity sets using the cluster analysis tool. A specific stereo net plot was generated for each source of data (3D photogrammetry, diamond-drill core

logging, and acoustic televiewer logging), with the intention of identifying discontinuity clusters over multiple datasets. This could suggest that the structural features observed at surface (planar data) could be present at depth (linear data).

Terzaghi weighting was applied as a corrective measure in the stereo net plots of the diamond-drill core and acoustic televiewer datasets to consider the drill hole orientations.

In the case of the joint sets and structures measured from 3D photogrammetry, these were validated with the implementation of the LIS GeoTec software tool from RIEGL. The tool is a RiSCAN Pro Plugin that detects clusters of dominant surface orientations from laser scan data (RIEGL, 2020). The plugin was applied to analyze the dominant surface orientations from the point cloud of the September 2022 Kevitsa pit scan (Figure 42).

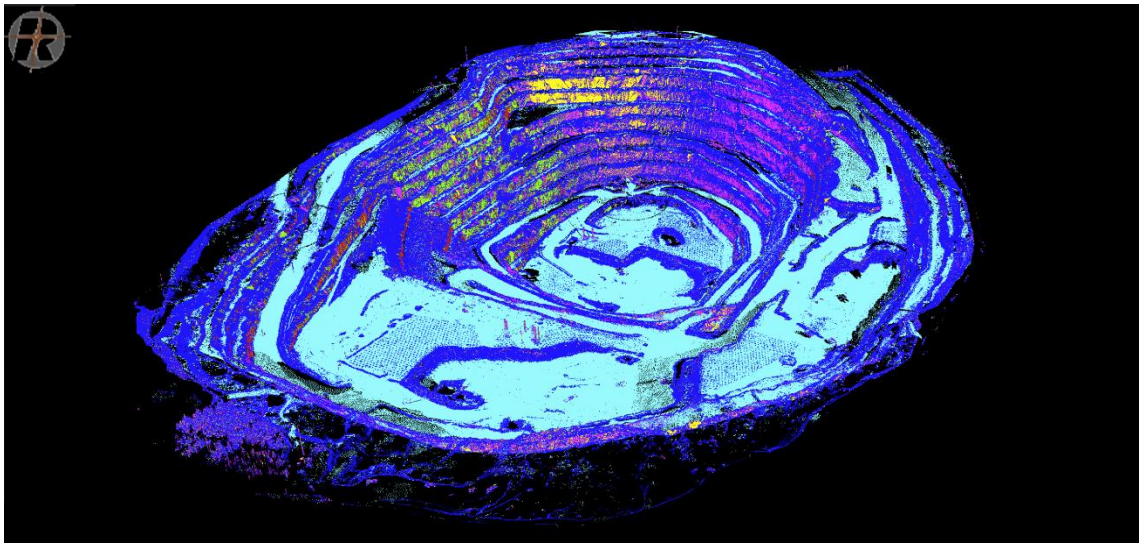

Figure 42. Visualization of the September 2022 Kevitsa pit scan in terms of LIS Discontinuity Sets attribute.

After identifying the discontinuity sets in each dataset, a structural interpretation was conducted on joint sets visible in both linear and planar datasets, as these could potentially impact the stability of the Stage 5 pit. These were labelled with specific letters (e.g., SET A) for a clear tracking. The interpretation conducted involved analyzing properties such as the orientation, persistence, and spacing of the discontinuities, as this would provide a better understanding of their structural and geotechnical condition.

4.4 Kinematic Analysis of Rock Blocks

Kinematic analyses by means of stereographic projections were conducted for the different-scale slopes of the Stage 5 pit using the software Rocscience DIPS. Analyses were run separately for each sector using only the structures from each area.

4.4.1 Kinematic Analysis of Bench Slopes

The stability of the bench-scale slopes was evaluated according to the effect of the minor discontinuities compiled from photogrammetry mapping, diamond drill-core logging, and acoustic televiewer logging. Analyses were conducted separately for each sector and according to the nature of the data, i.e., for the photogrammetry data (planar dataset) and the diamond-drill core and acoustic televiewer data (linear dataset). A summary of the data analyzed during the bench-scale kinematic analyses is presented in table 4.

Table 4. Summary of structural data used in the bench-scale kinematic analyses.

LINEAR DATA		PLANAR DATA	
SECTOR	**# OF JOINTS**	**SECTOR**	**# OF JOINTS**
North	1122	North	429
North East	899	North East	216
North West	960	North West	604
South	834	South	235
South East	871	South East	444
South West	678	South West	257
Whole Pit	5364	Whole Pit	2185

Initially, stereo net plots were constructed with each dataset to identify dominant joint orientations in each sector. Then, planar, wedge, and toppling failure modes were evaluated using bench face angles of 70°, 75°, 80°, 85°, and 90°. To consider the variability in the dip direction of the bench slopes from each sector, kinematic sensitivity analysis charts were examined in Rocscience DIPS (as shown in Figure 43). This provided a better understanding of the areas within each sector that represent a higher risk for slope failure.

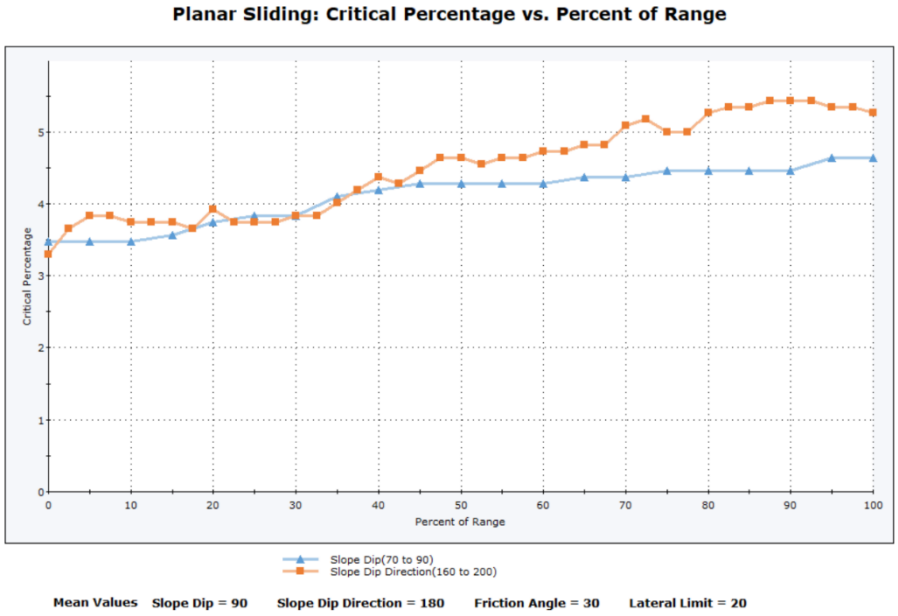

Figure 43. Planar Sliding - Kinematic Sensitivity Analysis chart for the linear data of the North sector using a ±20° range. Bench azimuth of 200° represents a higher instability.

The overall results of the kinematic analyses of the bench-scale slopes correspond to:

(1) Identification of predominant joint sets and critical intersections in each sector.

(2) Number of critical joints as a risk of planar sliding, wedge sliding, flexural toppling, and direct toppling. This means that the higher the percentage of critical joints, the higher the risk for failure is.

4.4.2 Kinematic Analysis of Inter-ramp Slopes

The stability of the inter-ramp scale slopes was evaluated according to the effect of the intermediate and major structures characterized for the Kevitsa deposit (Table 5). The intermediate structures correspond to the joint sets that were recognized to have a multi-bench structural condition (defined in section 5.2); and the major structures correspond to the large-scale features modelled in the Kevitsa Structural Interpretation 2023.

Table 5. Structural features considered for the inter-ramp scale kinematic analyses.

MAJOR STRUCTURES	INTERMEDIATE STRUCTURES
NE-flt-rv1	SET A
NE-flt-2	SET D
EW-flt-1	SET E
ENE-flt-1	SET F
NS-flt-1	SET G
NS-flt-2	
NS-flt-3	
NS-flt-5	
Splay-flt-010	

Planar and wedge failure modes were evaluated in each sector according to the major structures cross cutting each inter-ramp slope, and the joint sets identified in that sector during the bench-scale kinematic analyses. This involved measuring the local orientation of the major structures in the slope, the inter-ramp slope angle (IRA), and the height of the slope described in terms of elevation i.e., meters relative level (mRL).

Example: The upper inter-ramp of the northern wall (+234mRL to -10mRL, ~ 51° IRA) is being intersected by structures NS-flt-1, NS-flt-2, NS-flt-3, and NE-flt-rv1 (Figure 44). Therefore, they are considered for the analysis of the slope. Additionally, as joint sets A, D, E, F, and G were identified in the northern sector during the bench-scale kinematic analyses, they are considered as well. Kinematic analyses are then performed to evaluate planar and wedge failure modes in the slope according to the designated azimuth of the north sector (180°) and the inter-ramp angle of the slope (51°). The structures considered are plotted as planes according to the local orientation of the structures intersecting the

slope (major structures), and the mean orientation of the joint sets (intermediate structures).

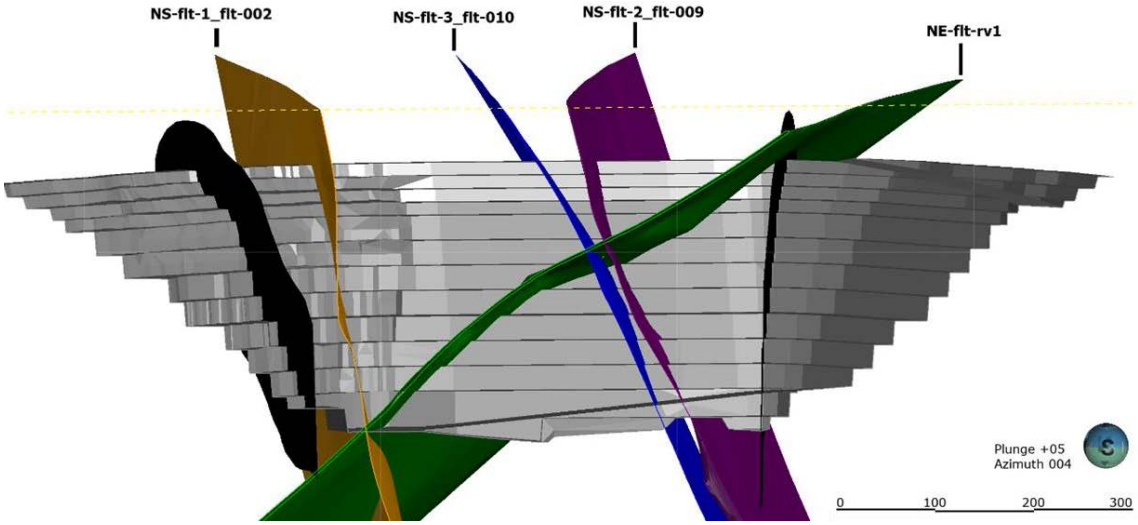

Figure 44. Major structures cross cutting the upper inter-ramp of the Northern wall.

The overall results of the kinematic analyses of the inter-ramp scale slopes correspond to:

(1) Identification of critical conditions (i.e., orientation, daylighting, location, continuity) of the intermediate and major structures that could represent a potential risk for developing slope failures in the inter-ramp slopes of the Stage 5 pit.

(2) Identification of critical intersections between joint sets and major structures that could potentially develop a multi-bench wedge failure.

4.4.3 Kinematic Analysis of Overall Slopes

The stability of the overall-scale slopes was assessed by considering the impact of the major structures modelled and interpreted in the Kevitsa Structural Interpretation 2023 (Pabst, 2023).

The assessment involved determining the orientation of the structural features in the slope, and the overall slope angle (OSA). Planar and wedge failure modes were evaluated for each sector according to the structures that intersected the overall slopes. The analyses are similar to those conducted for the inter-ramp scale slopes, and the results highlight the critical conditions and intersections of the major structures that could potentially lead to slope failures.

5 RESULTS

5.1 Dominant Joint Orientations

The main orientations of the minor discontinuities were identified in stereo nets of equal area projection. Structures were grouped into sets represented with the letter “m” for mean set planes, or the letter 'w' for weighted mean set planes.

Joint sets from diamond-drill core logging data (5061 structures)

The diamond-drill core dataset uses the Schmidt distribution for contouring due to the high number of rock joints. 14 joint sets were identified in the stereo net (Figure 45).

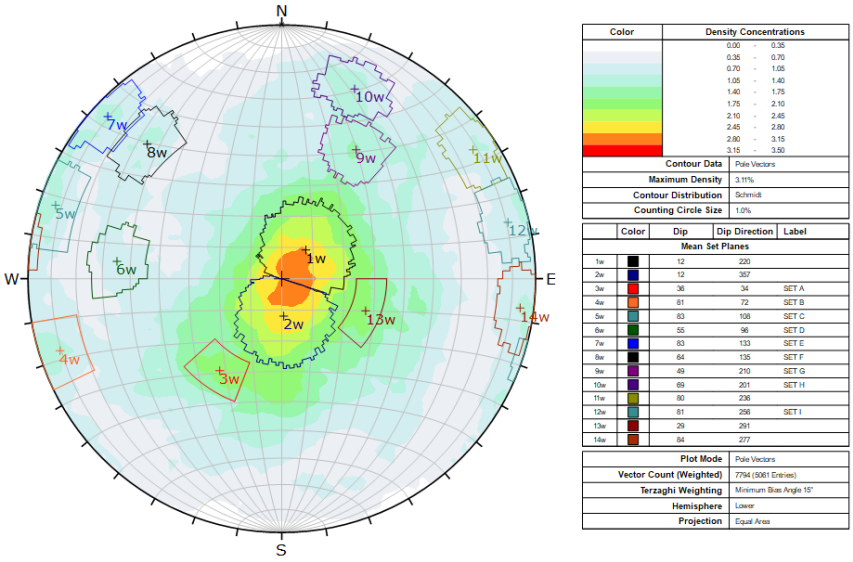

Figure 45. Stereo net of joint sets identified from diamond-drill core logging data.

Table 6 summarizes the joint sets identified with its corresponding labels. The stereo net with the structure’s poles is additionally presented in Appendix 1.

Table 6. Joint sets identified from diamond-drill core logging data.

SET	DIP	DIP DIRECTION	# OF JOINTS	LABEL
1w	12	220	507	
2w	12	357	521	
3w	36	34	111	SET A
4w	81	72	52	SET B
5w	83	108	47	SET C
6w	55	96	59	SET D
7w	83	133	41	SET E
8w	64	135	58	SET F
9w	49	210	111	SET G
10w	69	201	59	SET H
11w	80	236	55	
12w	81	256	53	SET I
13w	29	291	115	
14w	84	277	58	

Joint sets from photogrammetry mapping data (2185 structures)

The photogrammetry mapping dataset uses the Schmidt distribution for contouring due to the high number of rock joints. 14 joint sets were identified (Figure 46).

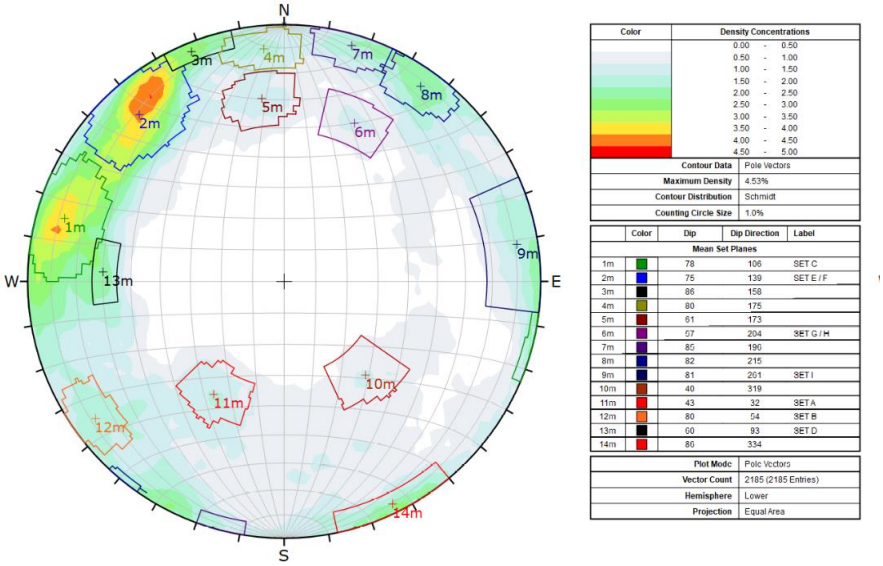

Figure 46. Stereo net of joint sets identified from photogrammetry mapping data.

The stereo net and data clusters of the photogrammetry mapping data were additionally compared with those obtained from applying the LIS GeoTec software tool from RIEGL in the September 2022 Kevitsa pit scan (Figure 47).

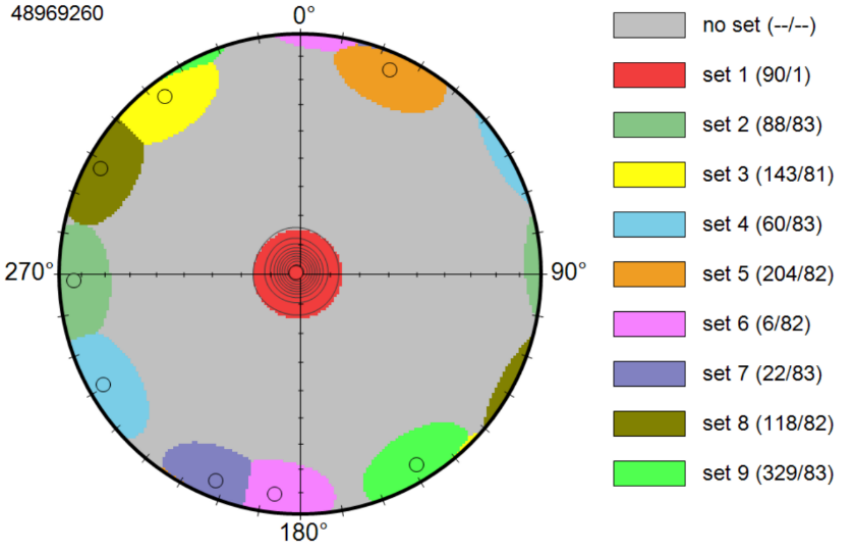

Figure 47. Dominant surface orientations from the September 2022 Kevitsa pit scan. Extracted from the LIS Geotech tool.

Comparison of the stereo nets exhibits a clear match in data clusters allocated in the North West quadrant of the diagrams (Set 1m and Set 8; Set 2m and Set 3), considering an angular variation of $\pm 20°$ (contemplated due to measurement bias of photogrammetry mapping). The matching plane orientations indicate the possible major joint sets of the deposit, suggesting a need for further examination. Additionally, they validate the structural mapping performed in the 3D photogrammetry, and the joint sets identified.

Table 7 summarizes the joint sets identified with its corresponding labels. The stereo net with the structure's poles is additionally presented in Appendix 2.

Table 7. Joint sets from photogrammetry mapping data.

SET	DIP	DIP DIRECTION	# OF JOINTS	LABEL
1m	78	106	237	SET C
2m	75	139	243	SET E / F
3m	86	158	31	
4m	80	175	44	
5m	61	173	42	
6m	57	204	28	SET G / H
7m	85	196	53	
8m	82	215	74	
9m	81	261	110	SET I
10m	40	319	31	
11m	43	32	50	SET A
12m	80	54	56	SET B
13m	60	93	50	SET D
14m	86	334	53	

Joint sets from acoustic televiewer logging data (303 structures)

The acoustic televiewer logging dataset uses the Fisher distribution for contouring due to the limited number of rock joints. 7 joint sets were identified (Figure 48).

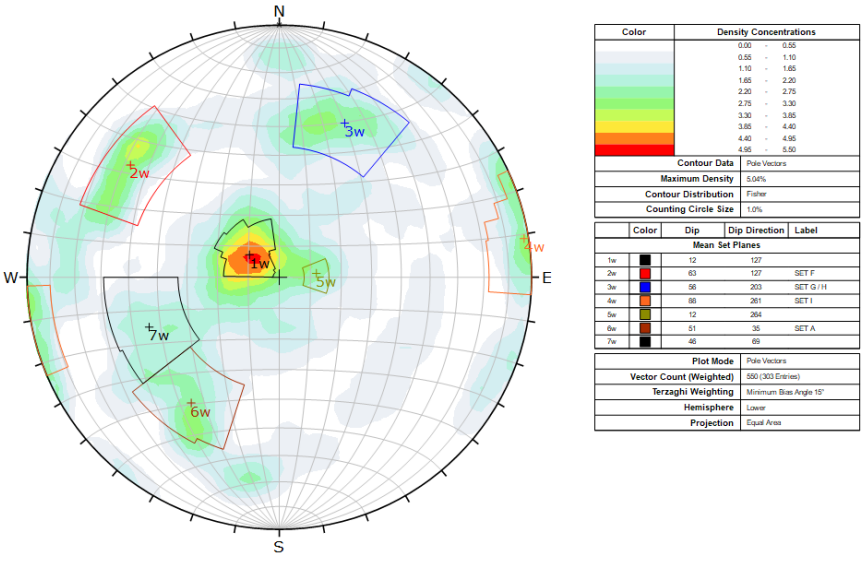

Figure 48. Stereo net of joint sets identified from acoustic televiewer logging data.

Table 8 summarizes the joint sets identified with its corresponding labels. The stereo net with the structure's poles is additionally presented in Appendix 3.

Table 8. Joint sets from acoustic televiewer logging data.

SET	DIP	DIP DIRECTION	# OF JOINTS	LABEL
1w	13	122	31	
2w	63	127	14	SET F
3w	56	203	21	SET G / H
4w	88	261	14	SET I
5w	12	264	11	
6w	48	66	17	
7w	52	33	15	SET A

5.2 Characterization of Joint Sets

Once the dominant joint orientations were identified, a structural and geotechnical interpretation was conducted in the joint sets observed in both linear and planar data (Table 9) due to their potential impact in the stability of the Stage 5 pit.

Table 9. Dominant joint sets considered for structural and geotechnical interpretation.

	Diamond-drill core		Acoustic televiewer		Photogrammetry	
SET	**DIP**	**DIP DIRECTION**	**DIP**	**DIP DIRECTION**	**DIP**	**DIP DIRECTION**
A	36	34	52	33	43	32
B	81	72			80	54
C	83	108			78	106
D	55	96			60	93
E	83	133			75	139
F	64	135	63	127		
G	49	210	53	203	57	204
H	69	201				
I	81	256	88	261	81	261

SET A: The structures from SET A have been identified in all datasets and can be described as west-northwest trending fractures that dip moderately towards the northeast. Their average persistence is of ~35m, and in some cases reaches up to 65m (Figure 49). The structures spacing varies greatly over the pit, ranging from 20m to more than 100m.

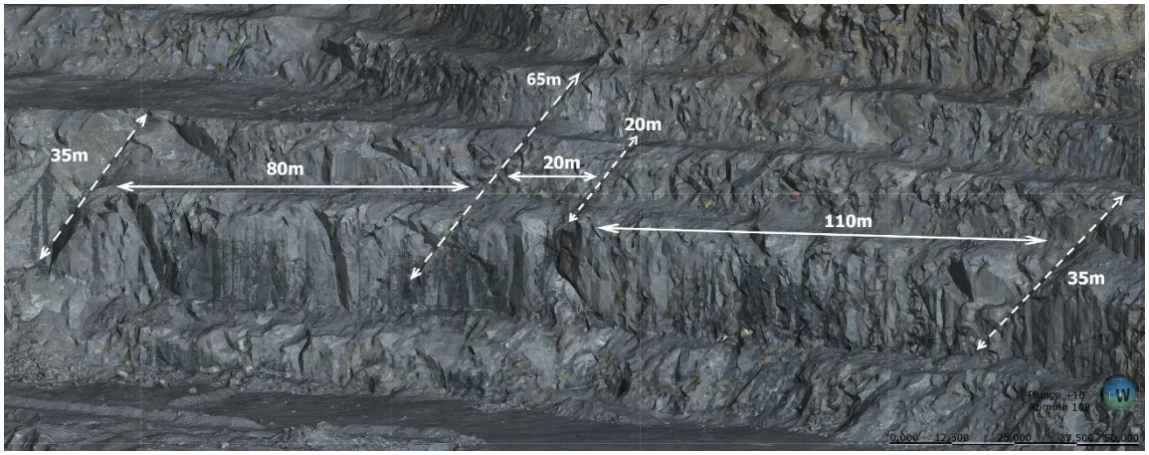

Figure 49. 3D view of the 2022 pit photogrammetry. Set A structures persistence in the southeastern section of the pit.

Visualization of both planar and linear data exhibits an even distribution of the structures all over the pit, with some local concentrations in the north section, and in the south-east section where its persistence is more prominent. The fractures persistence seems to be limited by structures from SET E and SET F in the west wall of the pit, which have a near-perpendicular dip direction in regards structures from joint set A (Figure 50).

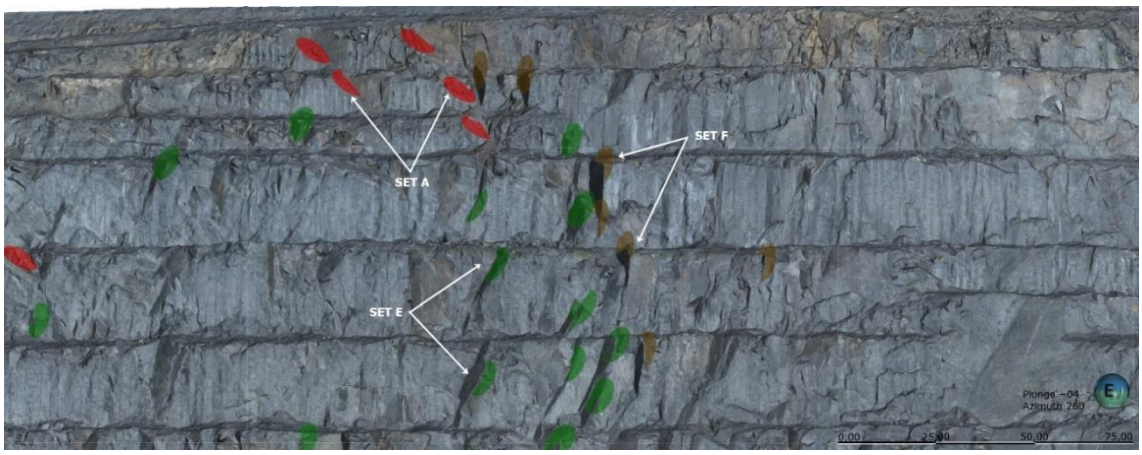

Figure 50. 3D view of the 2022 pit photogrammetry. Set A (red) limited by Set E (green) and Set F (orange).

Conclusively, fractures from SET A can be classified as intermediate structures with a potential to impact the stability of the inter-ramp slopes. Their persistence is predominantly orientated in a dip/dip direction of 50/30 (as measured from the pit photogrammetry) which is considered for the inter-ramp scale kinematic analyses.

SET B: The structures from SET B can be described as north, northwest trending fractures that dip near vertical. Examination of the structures suggest that they are associated to the vein system of the deposit, and more specifically to vein NS-flt-2_009 as they share a near-parallel orientation. Additionally, they are densely concentrated towards the east of the major structure where an average spacing of 10-15m can be measured (Figure 51).

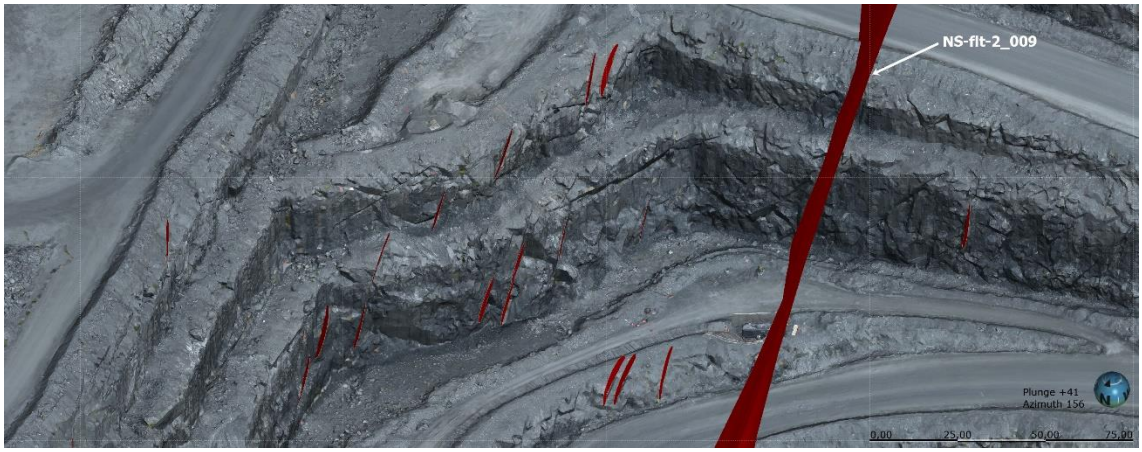

Figure 51. 3D view of the 2022 pit photogrammetry. Concentration of structures from Set B towards east of NS-flt-2_009 in the southeastern section of the pit.

The fractures persistence along their strike seems to be limited to the bench scale, and their length ranges from 15-30m. Multiple wedge-type failures of bench scale involving the structures from SET B can also be recognized (Figure 52), which suggests a potential

instability risk for the bench slopes, and an additionally safety risk for the haulage road located in the south-eastern section of the current pit.

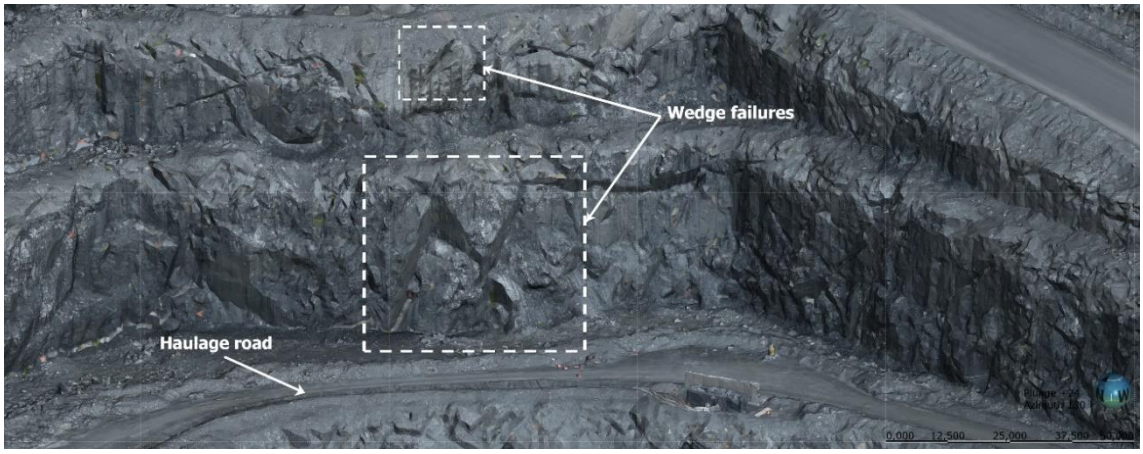

Figure 52. 3D view of the 2022 pit photogrammetry. Wedge failures involving Set B fractures in the southeastern section of the pit.

SET C: Structures from SET C can be described as northeast trending fractures that are steeply dipping towards the south east. The density of the structures is greater in the planar dataset in comparison to the linear dataset as its orientation makes it difficult to be measured in core.

The fractures are relatively small, averaging a length of 5m, and extending up to 10m in some cases. The spacing can be consistently measured in the northwestern section of the pit where fractures present an average spacing of 10-15m (Figure 53).

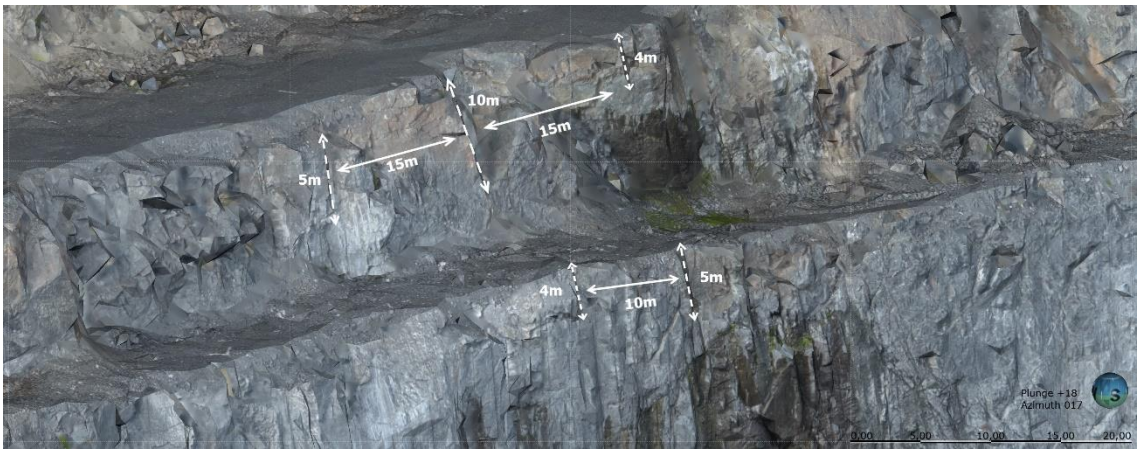

Figure 53. 3D view of the 2022 pit photogrammetry. Length and spacing of structures from Set C in the northwestern section of the pit.

The structures persistence is limited to the bench scale, which means that they don't represent a risk for the inter-ramp slopes. However, multiple bench scale wedge failures of different sizes are associated to the structures (Figure 54).

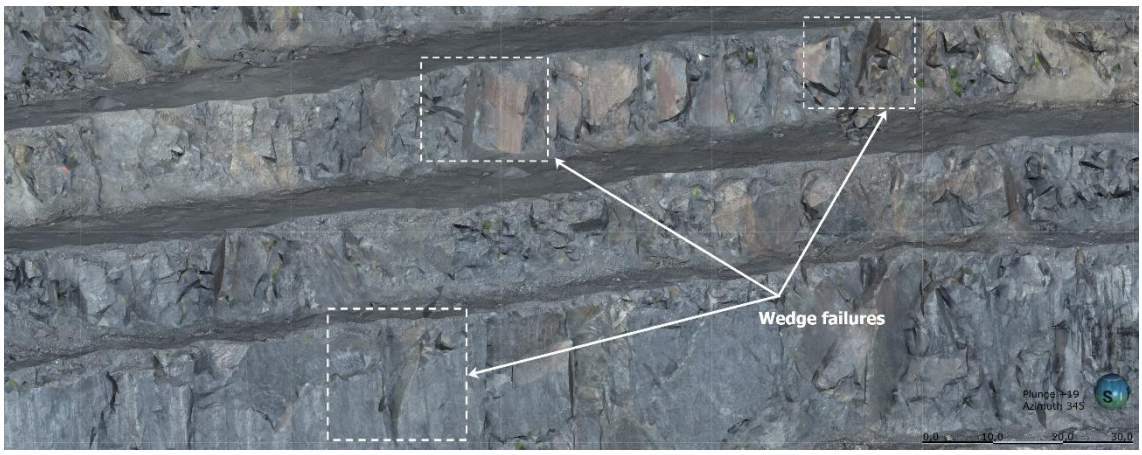

Figure 54. 3D view of the 2022 pit photogrammetry. Wedge failures involving structures from Set C in the northwestern section of the pit.

SET D: The structures from SET D can be described as highly persistence fractures that dip moderately steeply towards the east, with a semi-perpendicular trend to NE-flt-rv1.

From both planar and linear data, it can be observed that fractures with an average orientation of ~60/95 are distributed all over the deposit. Expressions of the structures in the north wall of the pit show a consistent multi-bench persistence that reaches up to 100m. Additionally, the structures seem to be widely space, where the average spacing distance is greater than 80m (Figure 55).

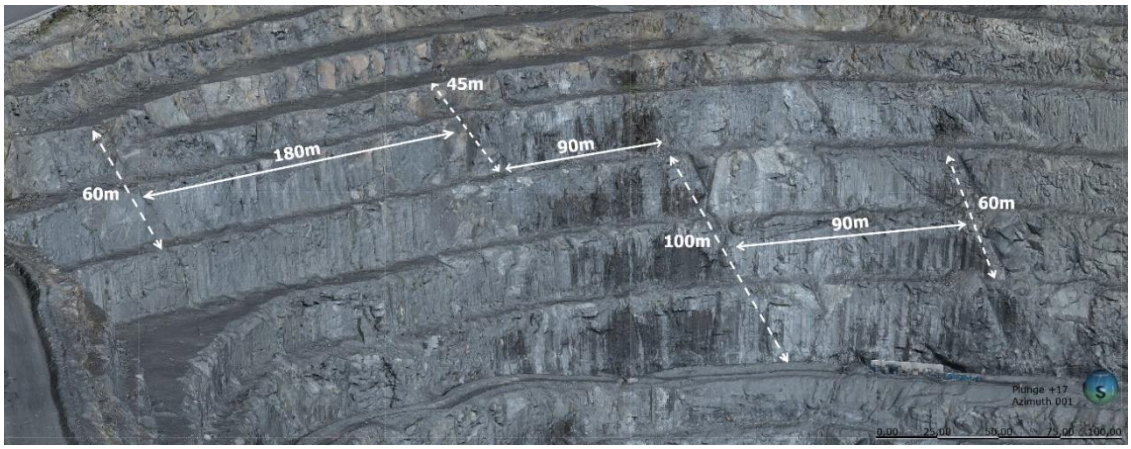

Figure 55. 3D view of the 2022 pit photogrammetry. Persistence and spacing of the structures from Set D in the northern section of the pit.

The persistence and spacing of the structures from SET D suggest that they extend over a significant area of the mine site, and additionally may have a potential impact on the stability of the inter-ramp slopes. The structures are also found generating bench-scale wedge failures with fractures dipping towards the south west (Figure 56).

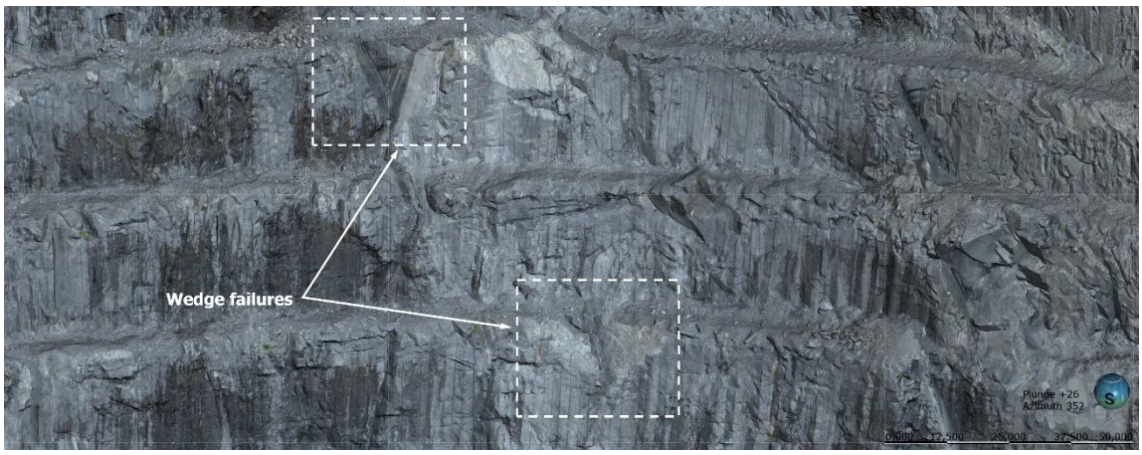

Figure 56. 3D view of the 2022 pit photogrammetry. Wedge failures involving structures from Set D in the north section of the pit.

SET E & SET F: Examination of structures from SETS E and F suggest that they may belong to the same structural domain, constituting a major joint set of the deposit where the structures can be described as north-east trending joints that dip steeply towards the south-east with a 20° variation. The fractures have been previously recognized in multiple studies of the Kevitsa deposit (WSP 2015; Pabst 2023), where they have been grouped as a dominant joint set.

Structures from SETS E and F were grouped into a singular joint set by the cluster analysis of the photogrammetry mapping data; and the LIS GeoTec analysis of the September 2022 pit scan. However, further differentiation was possible by observing the diamond-drill core data stereo net, which revealed two clusters with a slight orientation difference. Upon examining the pit photogrammetry, it was recognized that the main difference between the joint sets is that SET E structures appear to be steeper (as shown in Figure 57), while their trend, spacing, and location remain closely associated.

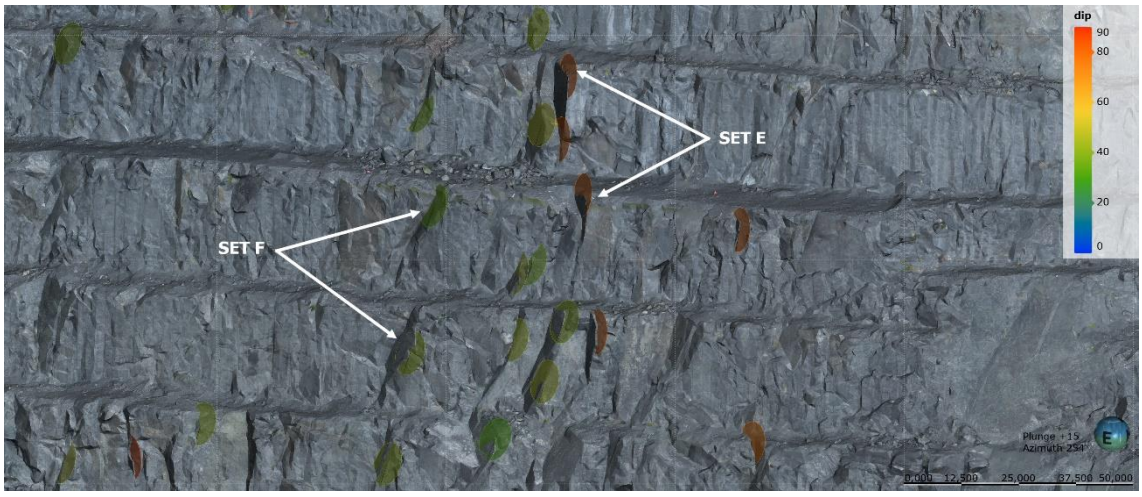

Figure 57. 3D view of the 2022 pit photogrammetry. Structures from Set E and Set F visualized according to their dip in the western wall of the pit.

The structures from SETS E and F have a multi-bench condition as their persistence extends up to 100m in the east wall of the pit, and up to 150m in the west wall of the pit (Figure 58).

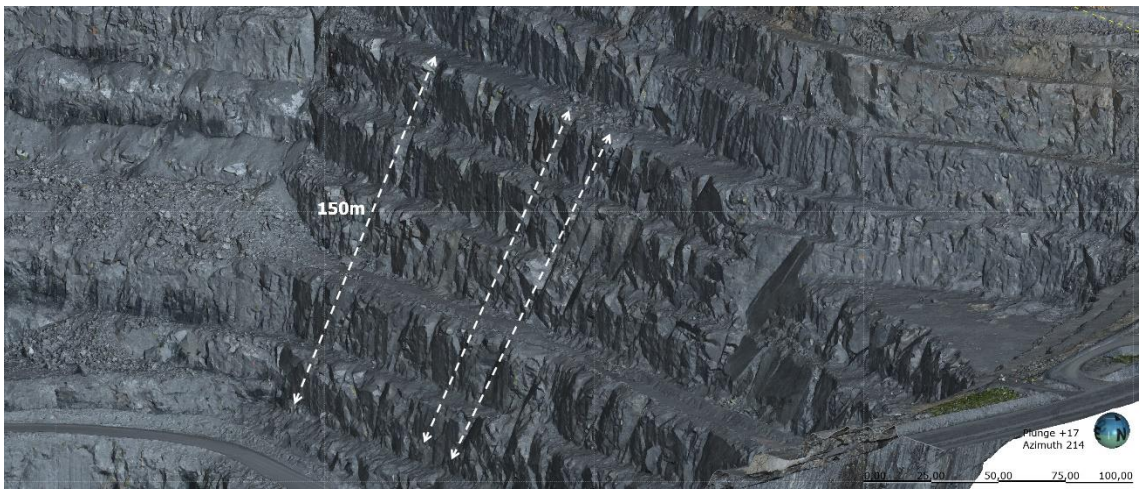

Figure 58. 3D view of the 2022 pit photogrammetry. Persistence of structures from Set E and Set F in the western wall of the pit.

The fractures are observed to be developed parallel to each other and can be easily traced along their strike, with an average spacing that ranges from 5-20m. The consistency in the orientation, persistence, and spacing characteristics indicate that the structures from SETS E and F belong to a major-systematic joint set of the Kevitsa deposit, with a high potential to impact the stability of the inter-ramp slopes of the current pit and the Stage 5 pit. Nevertheless, due to the significant dip variation between the joint sets, they are singularly considered for the inter-ramp scale kinematic analyses with an orientation of 80/140 and 65/135 (Set E and F, respectively) which betters adjust to their persistence.

SET G & SET H: The joint sets G and H are presented as two different data clusters in the diamond-drill core data stereo net, which are differentiated by an approximate angular variation of 20° in their dip. However, these seem to be expressed as singular data clusters in the photogrammetry mapping and acoustic televiewer data stereo nets. Joint set G had already been recognized in previous studies (WSP, 2014; Pabst, 2023).

The structures can be generally described as northwest trending joints that dip towards the south west, whereas SET H structures dip at a steeper angle in comparison to SET G. Both joint sets seem to be more prominent at depth, as their fracture density is more significant in the linear dataset (diamond-drill core and acoustic televiewer data) than in the planar dataset (photogrammetry mapping data) as exhibited in tables 6, 7, and 8.

From the pit photogrammetry it can be observed that the fractures occur as local-minor concentrations where SET H structures have a relatively smaller spacing (Figure 59).

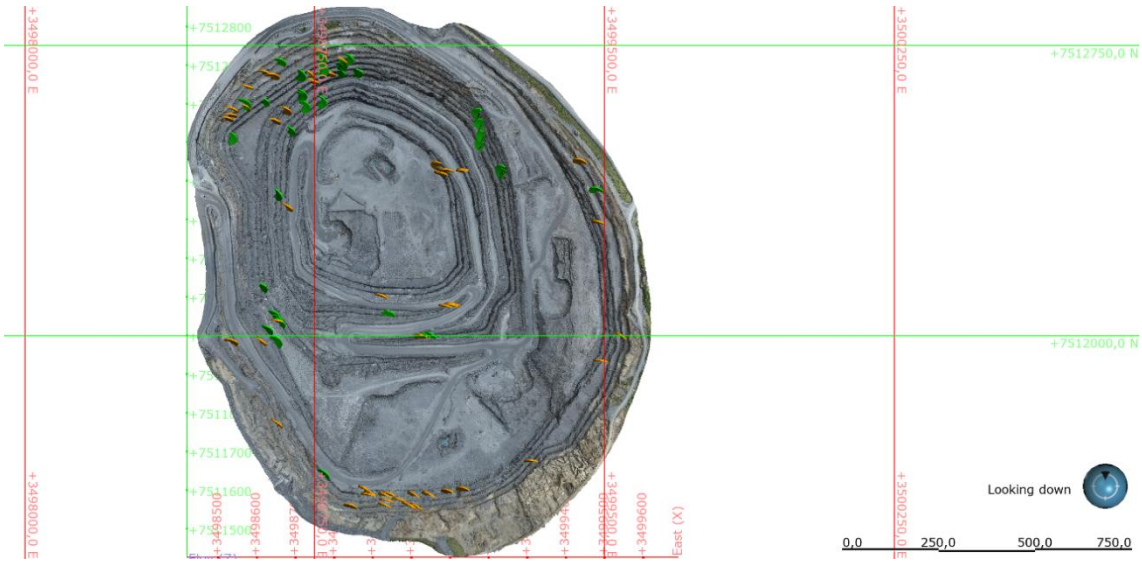

Figure 59. Plain view of the 2022 pit photogrammetry. Structures from Set G (green) and Set H (orange).

Structures from joint set G are mostly observed at surface in the north and north western sections of the pit, with a minor but significant occurrence in the north east. In general, the fractures are limited to the bench-scale with a fracture length of ~25m. However, wedge-type failures can be recognized involving the structures where the fractures persistence extends over the bench scale (+80m). This is visible in the north and north east sections of the pit (Figure 60).

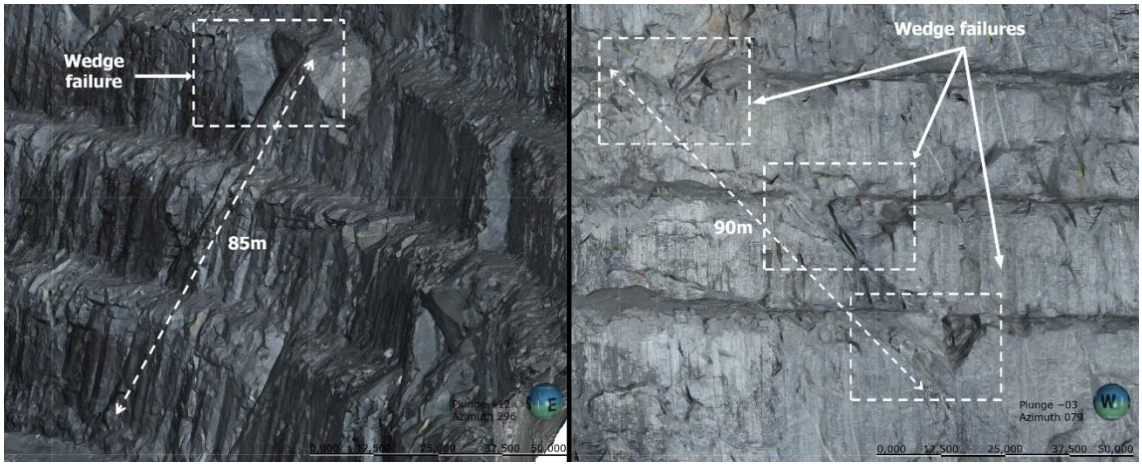

Figure 60. 3D view from the 2022 pit photogrammetry. Persistence of Set G structures. Northern wall of the pit (right). Eastern wall of the pit (left).

These expressions of great persistence indicate that SET G has a multi-bench condition and can have a potential impact on the stability of the inter-ramp slopes. Therefore, it is considered for their kinematic analyses with an orientation of 50/210.

As for structures from joint set H, they are observed in the north west and southern sections of the pit. At south it can be observed consistently that the fractures are relatively small (~5m) with an average spacing of 15-20m (Figure 61). They are not observed to be persistence over multiple benches and are not associated to any significant rock falls.

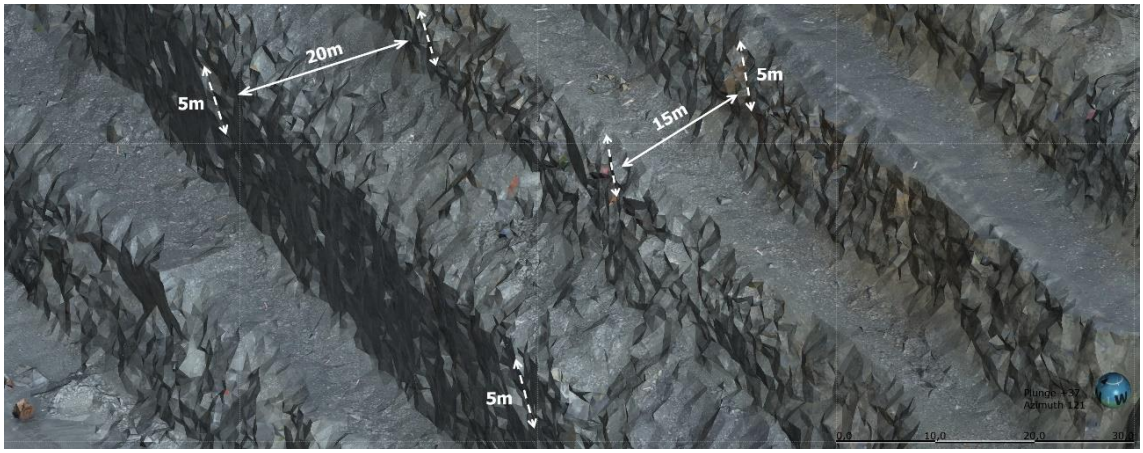

Figure 61. 3D view from the 2022 pit photogrammetry. Length and spacing of Set H structures in the southern section of the pit.

Due to the significant differences in length, spacing, and persistence between structures from SETS G and H, it is very unlikely that they belong to the same domain even thought their orientation is closely associated.

SET I: Structures from SET I can be described as near vertical fractures that trend towards the north west. They occur locally in the northwest, southwest, and southeastern sections of the pit. Most of the structures are allocated in the northwestern section, where they are found parallel to each other with a consistent length of ~5-10m and an average spacing of ~5m (Figure 62).

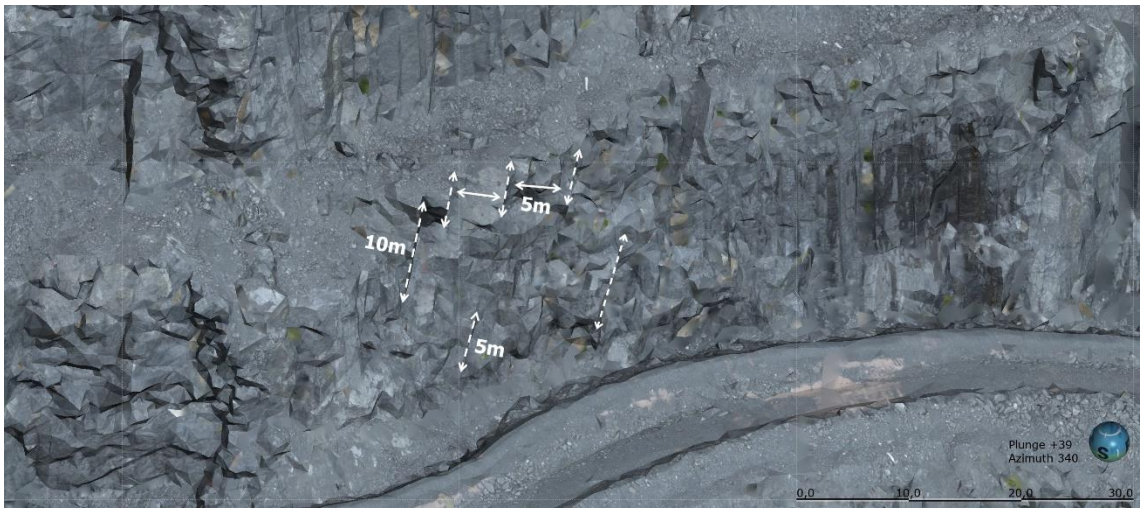

Figure 62. 3D view from the 2022 pit photogrammetry. Length and spacing of Set I structures in the northwestern section of the pit.

The structures are not associated to any rock falls of significant volume. However, they can generate minor wedge-type failures in combination with south west dipping fractures; and acting as lateral release surfaces for planar failures (Figure 63). Their size and persistence are also limited to the bench-scale.

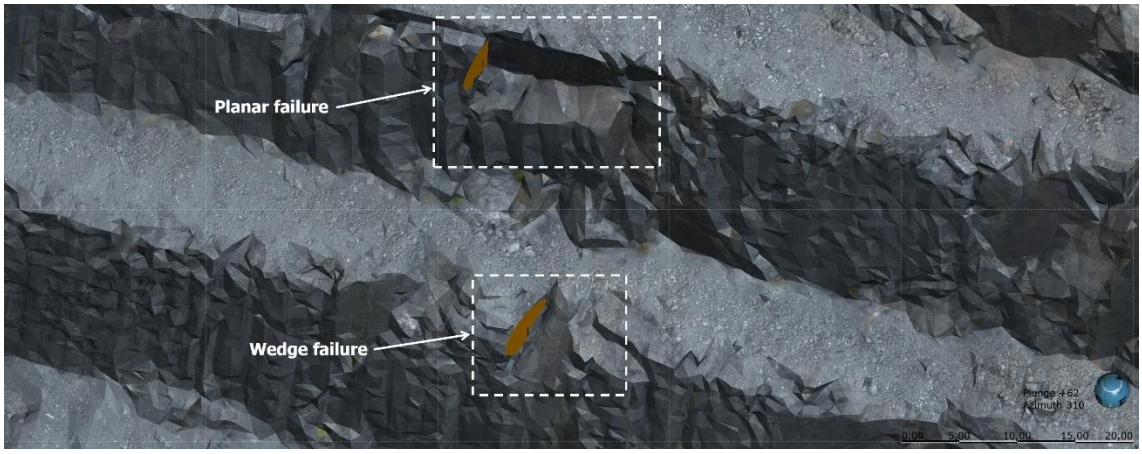

Figure 63. 3D view from the 2022 pit photogrammetry. Wedge and planar failures involving structures from Set I (orange) in the northwestern section of the pit.

5.3 Bench Slope Scale Stability Analysis

The stability analysis at bench scale evaluates planar, wedge, and toppling failure modes through stereo nets of equal angle projection. A friction angle of 30° was used for the analyses which corresponds to the lowest value measured from shear tests of discontinuities performed to six core specimens of the Kevitsa deposit (HUT, 2006). Terzaghi weighting was applied to consider the drill hole orientations.

5.3.1 North Sector

Dominant orientations of the minor discontinuities are presented in Table 10.

Table 10. Joint sets identified from the linear and planar data of the northern sector.

LINEAR DATA (1122 JOINTS)					PLANAR DATA (429 JOINTS)				
SET	**DIP**	**DIP DIRECTION**	**# OF JOINTS**	**ID**	**SET**	**DIP**	**DIP DIRECTION**	**# OF JOINTS**	**ID**
1w	9	243	139		1m	85	99	44	SET C
2w	13	42	143		2m	63	93	47	SET D
3w	54	99	23	SET D	3m	44	25	27	SET A
4w	38	30	52	SET A	4m	70	56	37	
5w	61	53	48		5m	71	118	23	
6w	79	130	22	SET E	6m	73	140	28	SET E / F
7w	51	203	25	SET G	7m	85	194	17	
					8m	54	206	13	SET G
					9m	35	323	12	
					10m	55	343	12	

The stereo nets constructed for the kinematic analyses are shown in Figure 64 and 65.

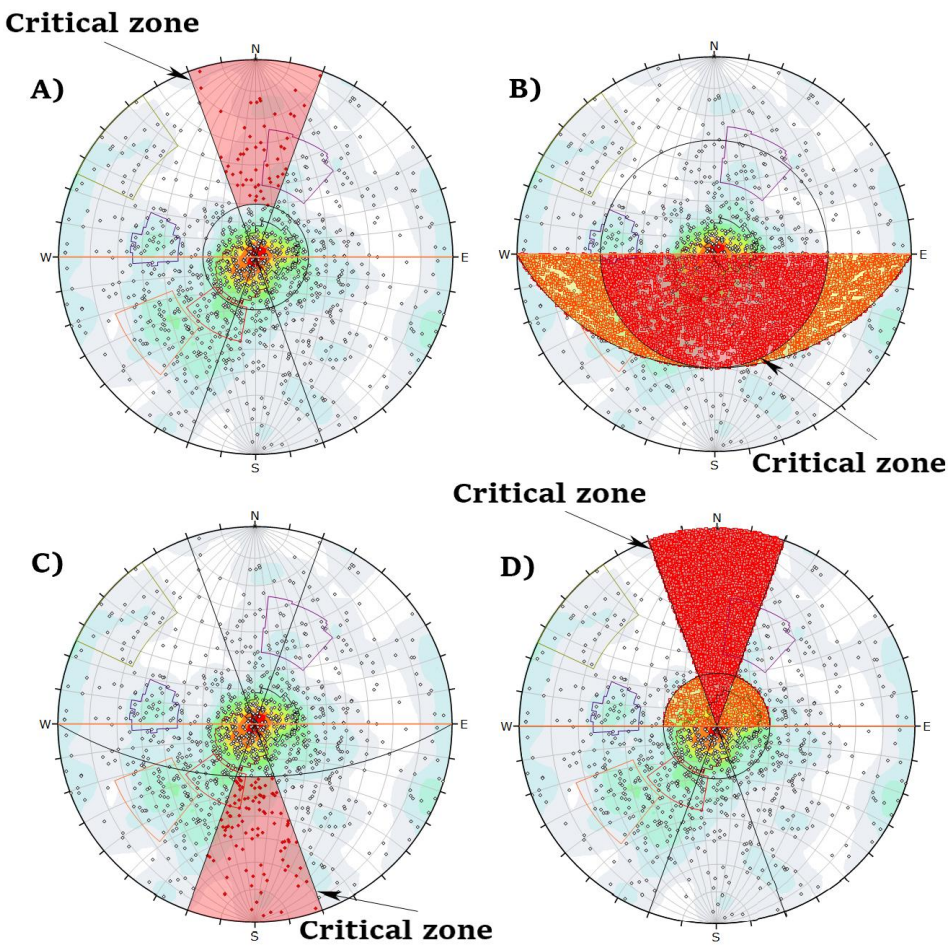

Figure 64. Kinematic analyses of the linear data of the northern sector using a 90° slope angle. (A) Planar sliding. (B) Wedge sliding. (C) Flexural Toppling. (D) Direct Toppling.

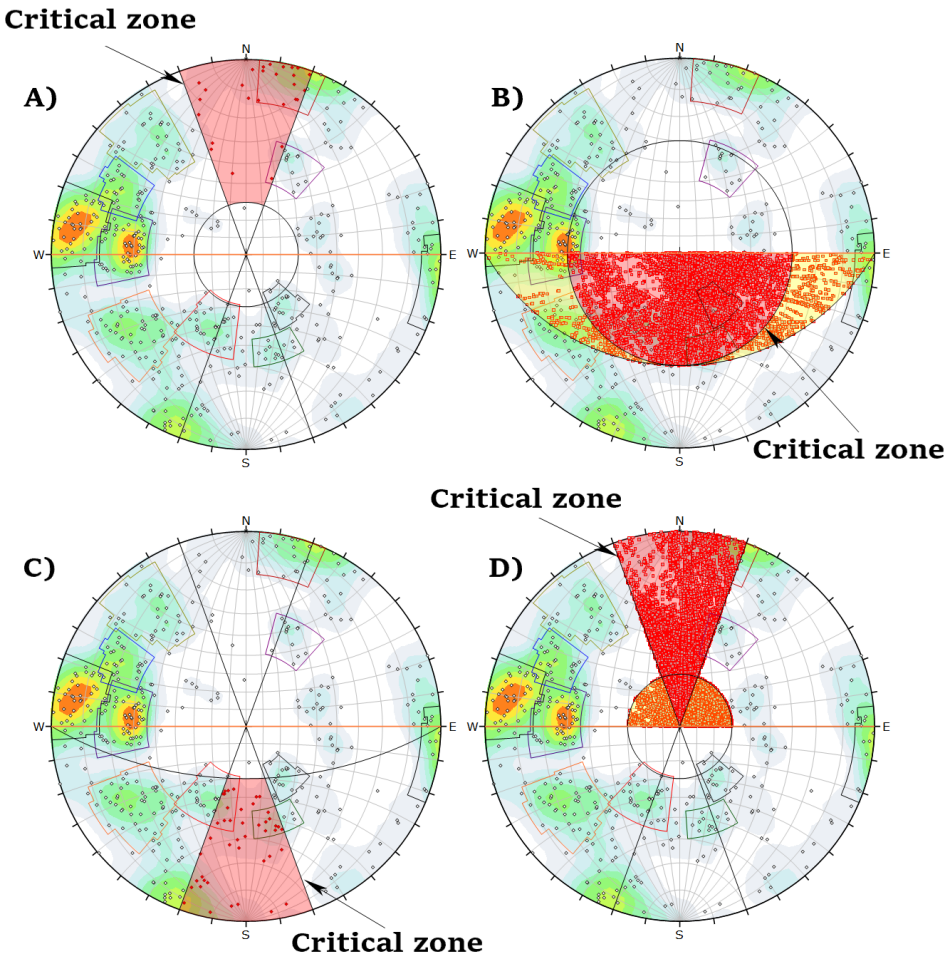

Figure 65. Kinematic analyses of the planar data of the northern sector using a 90° slope angle. (A) Planar sliding. (B) Wedge sliding. (C) Flexural Toppling. (D) Direct Toppling.

Linear data stereo nets (Figure 64) exhibit fracture populations dominated by sub-horizontal fractures with two main orientations (sets 1w and 2w), which do not represent a structural failure risk for the benches of the north sector. In contrast, dominant fractures from the planar data are mostly moderate to steeply dipping (sets C and D). However, their poles are not found considerably within the critical zone of any failure mode.

Table 11 presents the analyses results for the north sector (180° slope dip direction). Risk for each failure mode is represented by the quantities (percentages) of critical joints.

Table 11. Risk of planar, wedge, flexural toppling, and direct toppling failure modes.

	LINEAR DATA				PLANAR DATA			
	PLANAR	WEDGE	F. TOPPLING	D.TOPPLING	PLANAR	WEDGE	F. TOPPLING	D.TOPPLING
70°	3,93 %	9,58 %	5,78 %	7,18 %	1,17 %	14,17 %	7,69 %	12,84 %
75°	4,76 %	11,08 %	6,62 %	8,78 %	1,17 %	17,43 %	8,39 %	13,50 %
80°	5,65 %	13,19 %	7,44 %	10,49 %	2,33 %	21,81 %	8,62 %	14,01 %
85°	5,88 %	14,47 %	8,19 %	12,61 %	3,96 %	27,15 %	10,26 %	14,49 %
90°	6,14 %	**15,77 %**	8,99 %	14,81 %	6,29 %	**32,92 %**	10,26 %	15,04 %

The overall results from the analyses are consistent between the linear and planar data. Planar sliding and flexural toppling exhibit a low risk due to the small amount of south-dipping and north-dipping structures (respectively). Wedge sliding presents the highest risk, followed by direct toppling. The risk for planar, flexural toppling, and direct toppling failure becomes higher towards the east of the sector, while for wedge failure towards the west (from kinematic sensitivity charts). Figure 66 presents the matrix of critical intersections for wedge sliding at 90° slope dip (stereo nets in Appendix 4 and 5).

LINEAR DATA								PLANAR DATA									
SET	1w	2w	D	A	5w	E	G	SET	C	D	A	4m	5m	E/F	7m	G	9m	10m
1w								C										
2w								D										
D								A										
A								4m										
5w								5m										
E								E/F										
G								7m										
								G										
								9m										
								10m										

Figure 66. Matrix of critical intersections of joint sets for wedge sliding. Intersections in primary critical zone (red). Intersections in secondary critical zone (yellow).

5.3.2 North East Sector

Dominant orientations of the minor discontinuities are presented in Table 12.

Table 12. Joint sets identified from the linear and planar data of the northeastern sector.

LINEAR DATA (899 JOINTS)					PLANAR DATA (216 JOINTS)				
SET	DIP	DIP DIRECTION	# OF JOINTS	ID	SET	DIP	DIP DIRECTION	# OF JOINTS	ID
1w	64	124	52	SET F	1m	78	106	43	SET C
2w	81	130	10	SET E	2m	73	140	33	SET E/F
3w	54	85	37	SET D	3m	67	34	17	
4w	40	56	26		4m	68	303	8	
5w	13	258	35		5m	85	205	9	SET H
6w	29	292	72						
7w	49	292	46						
8w	49	226	32	SET G					
9w	73	197	21	SET H					
10w	89	240	22						

The stereo nets constructed for the kinematic analyses are shown in Figure 67 and 68.

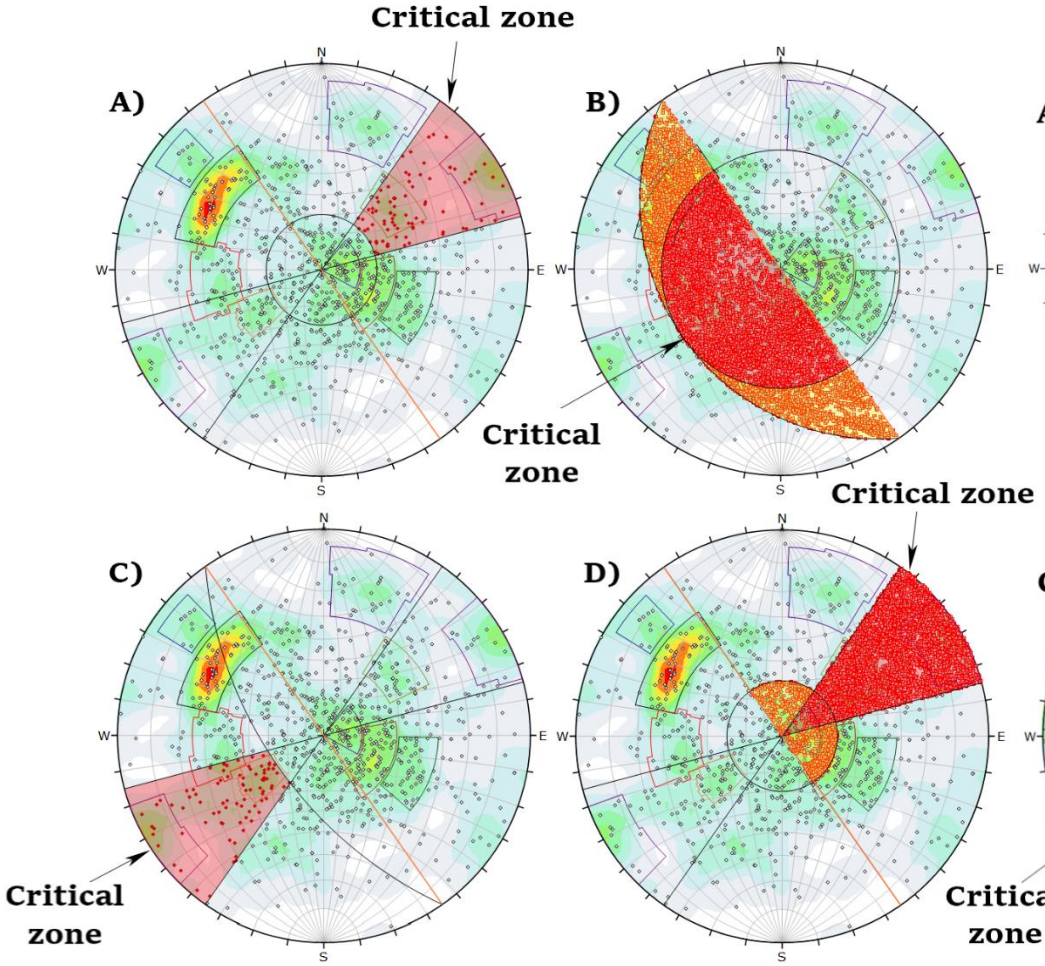

Figure 67. Kinematic analyses of the linear data of the northeastern sector using a 90° slope angle. (A) Planar sliding. (B) Wedge sliding. (C) Flexural Toppling. (D) Direct Toppling.

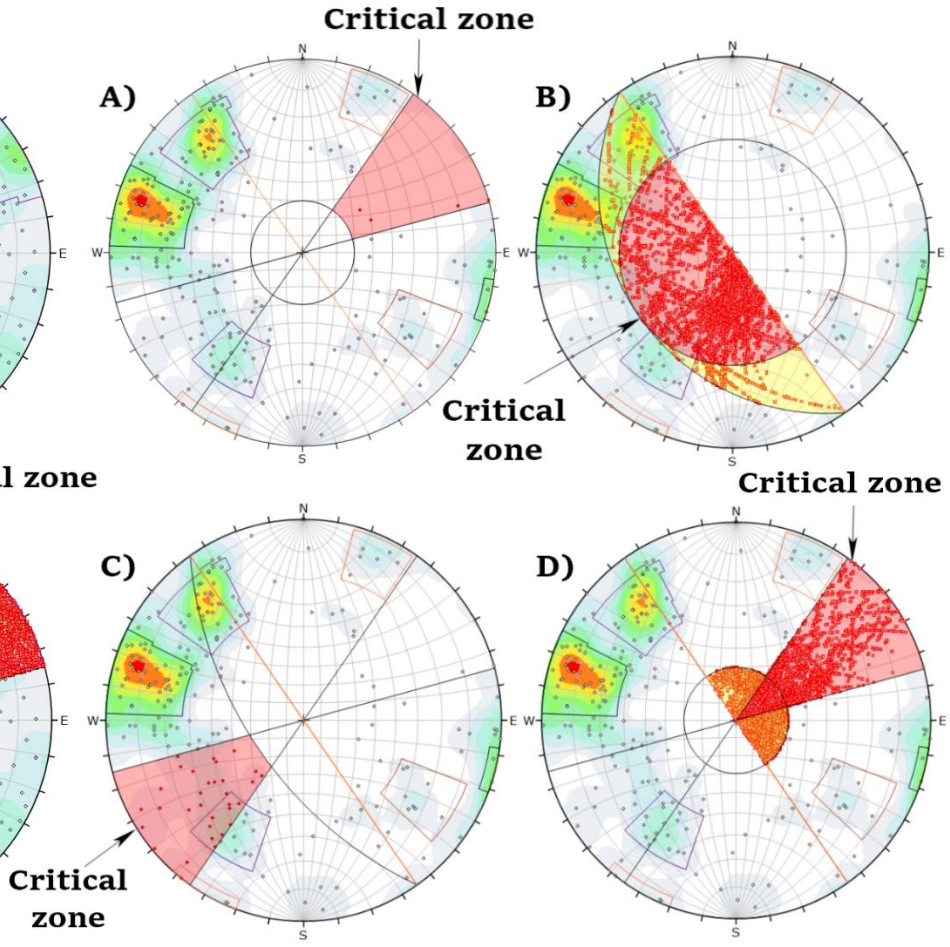

Figure 68. Kinematic analyses of the planar data of the northeastern sector using a 90° slope angle. (A) Planar sliding. (B) Wedge sliding. (C) Flexural Toppling. (D) Direct Toppling.

Structures from both linear and planar data exhibit significant density concentrations in the NW quadrant, corresponding to fractures from joint sets E, F, and C. However, they do not represent a direct structural failure risk for the benches of the north east sector. Linear data stereo nets (Figure 67) suggest a risk of planar failures from structures from joint sets G and H, as they are allocated in the critical zone for planar sliding.

Table 13 presents the analyses results for the northeast sector (235° slope dip direction).

Table 13. Risk of planar, wedge, flexural toppling, and direct toppling failure modes.

	LINEAR DATA				PLANAR DATA			
	PLANAR	WEDGE	F. TOPPLING	D.TOPPLING	PLANAR	WEDGE	F. TOPPLING	D.TOPPLING
70°	5,91 %	16,02 %	7,40 %	7,14 %	0,93 %	11,98 %	12,96 %	18,06 %
75°	6,40 %	17,93 %	8,35 %	8,13 %	0,93 %	14,41 %	12,96 %	18,51 %
80°	7,08 %	20,34 %	9,05 %	9,15 %	0,93 %	16,99 %	13,89 %	18,95 %
85°	8,10 %	22,88 %	9,97 %	10,19 %	1,39 %	19,85 %	14,81 %	19,35 %
90°	9,13 %	**25,46 %**	10,85 %	11,33 %	1,85 %	**23,98 %**	14,81 %	19,75 %

Results indicate that the risk for planar sliding is relatively low. However, it is associated to structures from SET G which are recognized to have a multi-bench condition. Toppling modes present a moderately low risk, which is greater in the planar data. Wedge sliding presents the highest risk (from both linear and planar data). Kinematic sensitivity charts indicate a higher risk of wedge sliding towards the southeast of the sector, and a higher risk of planar sliding towards the north west. Toppling modes remain constant within a ±20° angular variation in the dip direction of the slopes. Figure 69 presents the matrix of critical intersections for wedge sliding at 90° slope dip (stereo nets in Appendix 6 and 7).

LINEAR DATA											PLANAR DATA					
SET	**F**	**E**	**D**	**4w**	**5w**	**6w**	**7w**	**G**	**H**	**10w**	**SET**	**C**	**E/F**	**3m**	**4m**	**H**
F											**C**					
E											**E/F**					
D											**3m**					
4w											**4m**					
5w											**H**					
6w																
7w																
G																
H																
10w																

Figure 69. Matrix of critical intersections of joint sets for wedge sliding. Intersections in primary critical zone (red). Intersections in secondary critical zone (yellow).

5.3.3 North West Sector

Dominant orientations of the minor discontinuities are presented in Table 14.

Table 14. Joint sets identified from the linear and planar data of the north west sector.

LINEAR DATA (960 JOINTS)					PLANAR DATA (604 JOINTS)				
SET	**DIP**	**DIP DIRECTION**	**# OF JOINTS**	**ID**	**SET**	**DIP**	**DIP DIRECTION**	**# OF JOINTS**	**ID**
1w	22	208	88		1m	80	103	59	SET C
2w	15	129	67		2m	70	124	55	SET F
3w	61	134	11	SET F	3m	83	142	26	SET E
4w	45	178	28		4m	61	177	26	
5w	53	208	42	SET G	5m	66	228	36	
6w	62	228	29		6m	89	225	56	
7w	82	272	38		7m	80	255	32	SET I
8w	43	303	32		8m	46	314	22	
9w	16	353	44		9m	39	44	14	SET A
10w	37	38	32	SET A	10m	58	85	31	SET D

The stereo nets constructed for the kinematic analyses are shown in Figure 70 and 71.

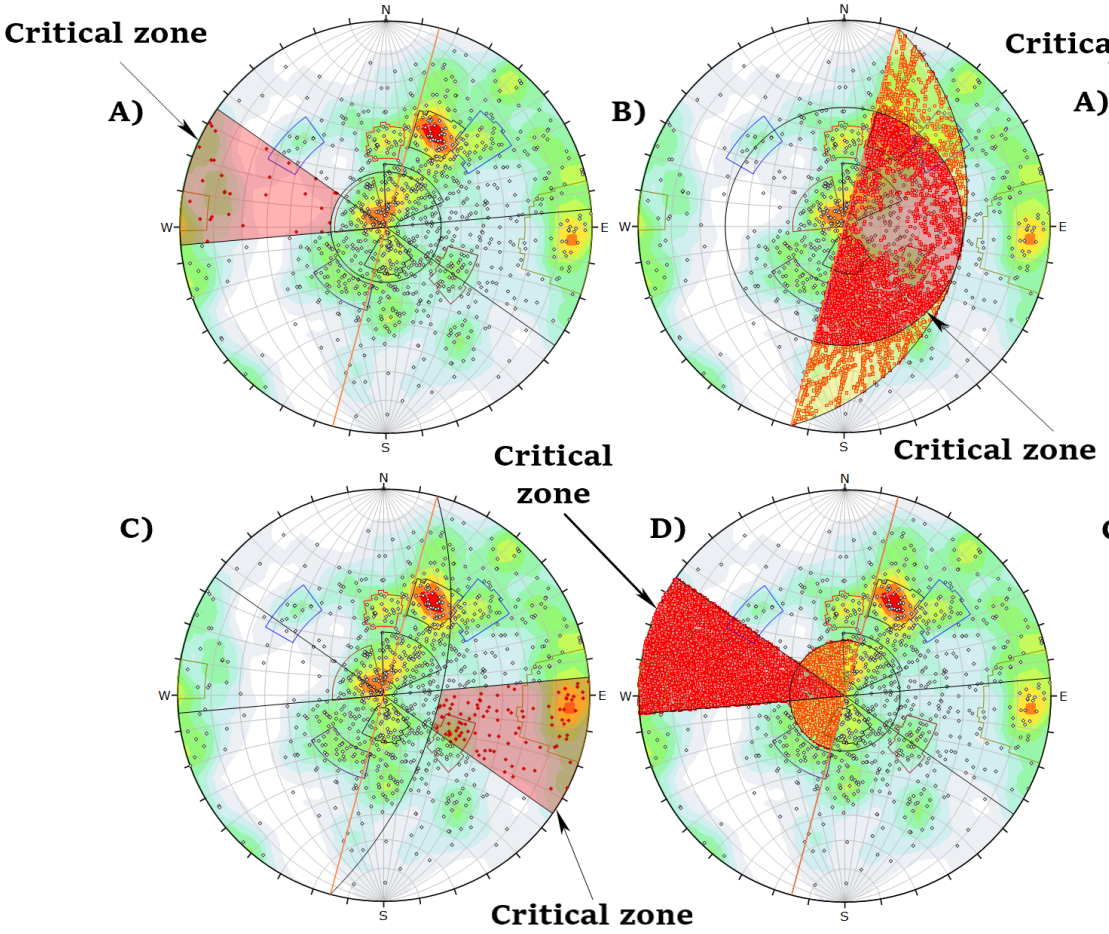

Figure 70. Kinematic analyses of the linear data of the northwestern sector using a 90° slope angle. (A) Planar sliding. (B) Wedge sliding. (C) Flexural Toppling. (D) Direct Toppling.

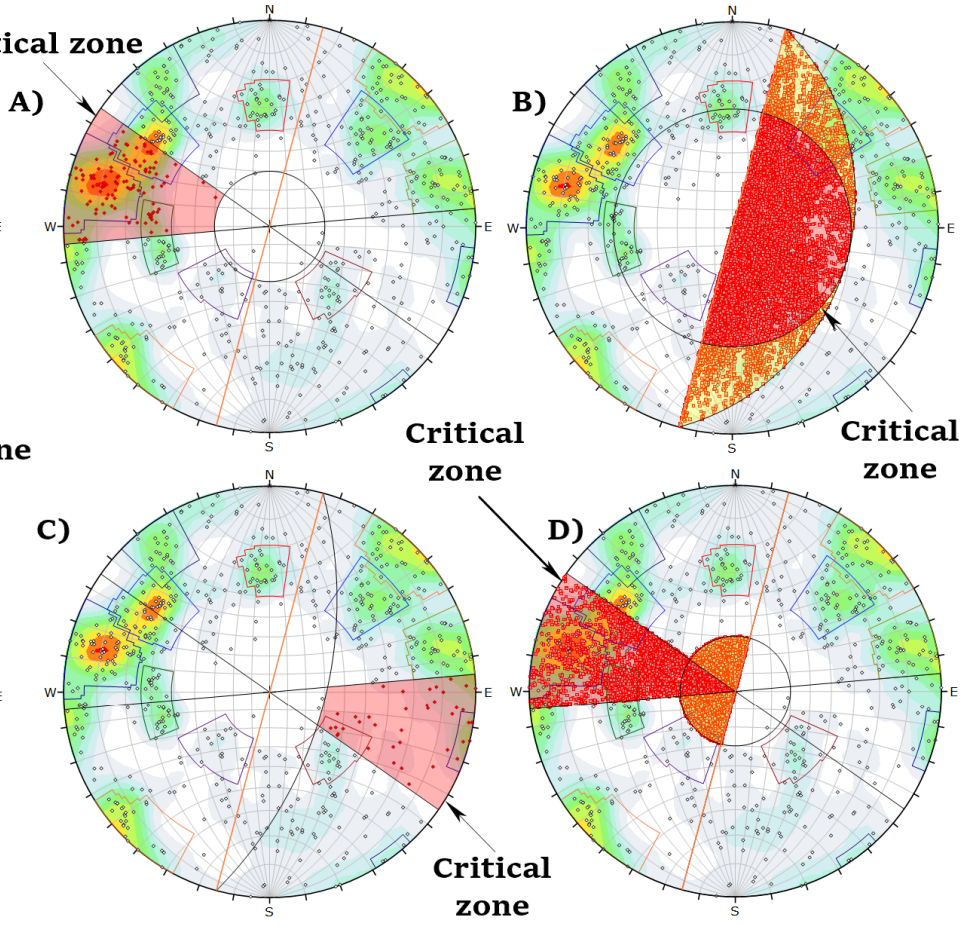

Figure 71. Kinematic analyses of the planar data of the northwestern sector using a 90° slope angle. (A) Planar sliding. (B) Wedge sliding. (C) Flexural Toppling. (D) Direct Toppling.

The structures from the linear data stereonets (Figure 70) are mostly allocated in the NE quadrant, corresponding to moderately steep fractures that dip towards the south west. These do not represent a direct structural failure risk for the benches of the north west sector. In comparison, planar data stereo nets exhibit high density concentrations of structures from Set C and E, which represent a direct risk for planar and wedge failures in the bench slopes.

Table 15 presents the analyses results for the northwest sector (105° slope dip direction).

Table 15. Risk of planar, wedge, flexural toppling, and direct toppling failure modes.

	LINEAR DATA				PLANAR DATA			
	PLANAR	WEDGE	F. TOPPLING	D.TOPPLING	PLANAR	WEDGE	F. TOPPLING	D.TOPPLING
70°	1,39 %	9,51 %	7,21 %	7,36 %	6,62 %	23,10 %	5,13	6,97
75°	1,89 %	11,70 %	7,95 %	8,75 %	8,94 %	30,60 %	5,46	7,23
80°	3,14 %	14,58 %	8,90 %	10,28 %	12,58 %	38,91 %	5,96	7,44
85°	4,26 %	17,38 %	9,46 %	12,09 %	15,89 %	47,01 %	6,46	7,61
90°	5,29 %	**20,09 %**	9,94 %	14,07 %	18,05 %	**54,12 %**	6,46	7,79

Analyses results indicate a high influence of north-east trending joints in the bench slopes stability (Sets C, E, and F). These joints are responsible for multiple critical intersections for wedge blocks (Figure 72, Appendix's 8 and 9), which results in a very high risk for wedge sliding. Additionally, the moderate risk of planar failure is attributed to Sets C and F as they constitute most of the critical poles allocated in the planar sliding critical zone. Toppling modes do not represent a significant risk. Towards the north-east of the sector (benches dip direction reaches 140°), the planar failure risk decreases and the wedge failure risk increases (from Kinematic sensitivity charts).

LINEAR DATA											PLANAR DATA										
SET	1w	2w	F	4w	G	6w	7w	8w	9w	A	SET	C	F	E	4m	5m	6m	I	8m	A	D
1w											C										
2w											F										
F											E										
4w											4m										
G											5m										
6w											6m										
7w											I										
8w											8m										
9w											A										
A											D										

Figure 72. Matrix of critical intersections of joint sets for wedge sliding. Intersections in primary critical zone (red). Intersections in secondary critical zone (yellow).

5.3.4 South Sector

Dominant orientations of the minor discontinuities are presented in Table 16.

Table 16. Joint sets identified from the linear and planar data of the south sector.

LINEAR DATA (834 JOINTS)					PLANAR DATA (235 JOINTS)				
SET	DIP	DIP DIRECTION	# OF JOINTS	ID	SET	DIP	DIP DIRECTION	# OF JOINTS	ID
1w	17	350	66		1m	84	211	57	
2w	10	88	46		2m	79	174	15	
3w	14	221	43		3m	65	150	16	SET F
4w	28	248	25		4m	77	137	5	SET E
5w	69	227	20		5m	70	76	5	
6w	65	144	8	SET F	6m	46	35	16	SET A
7w	81	123	10	SET E					
8w	80	90	7						
9w	36	30	26	SET A					
10w	77	268	20	SET I					

The stereo nets constructed for the kinematic analyses are shown in Figure 73 and 74.

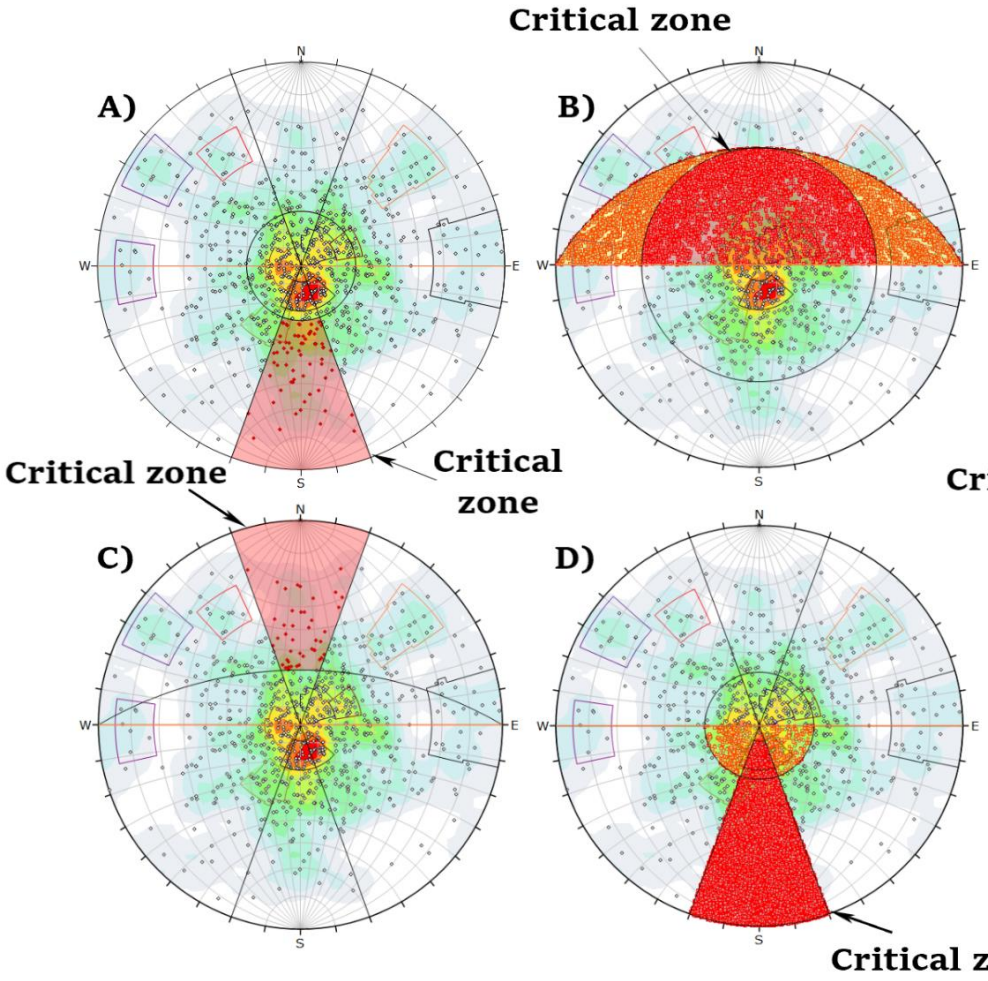

Figure 73. Kinematic analyses of the linear data of the southern sector using a 90° slope angle. (A) Planar sliding. (B) Wedge sliding. (C) Flexural Toppling. (D) Direct Toppling.

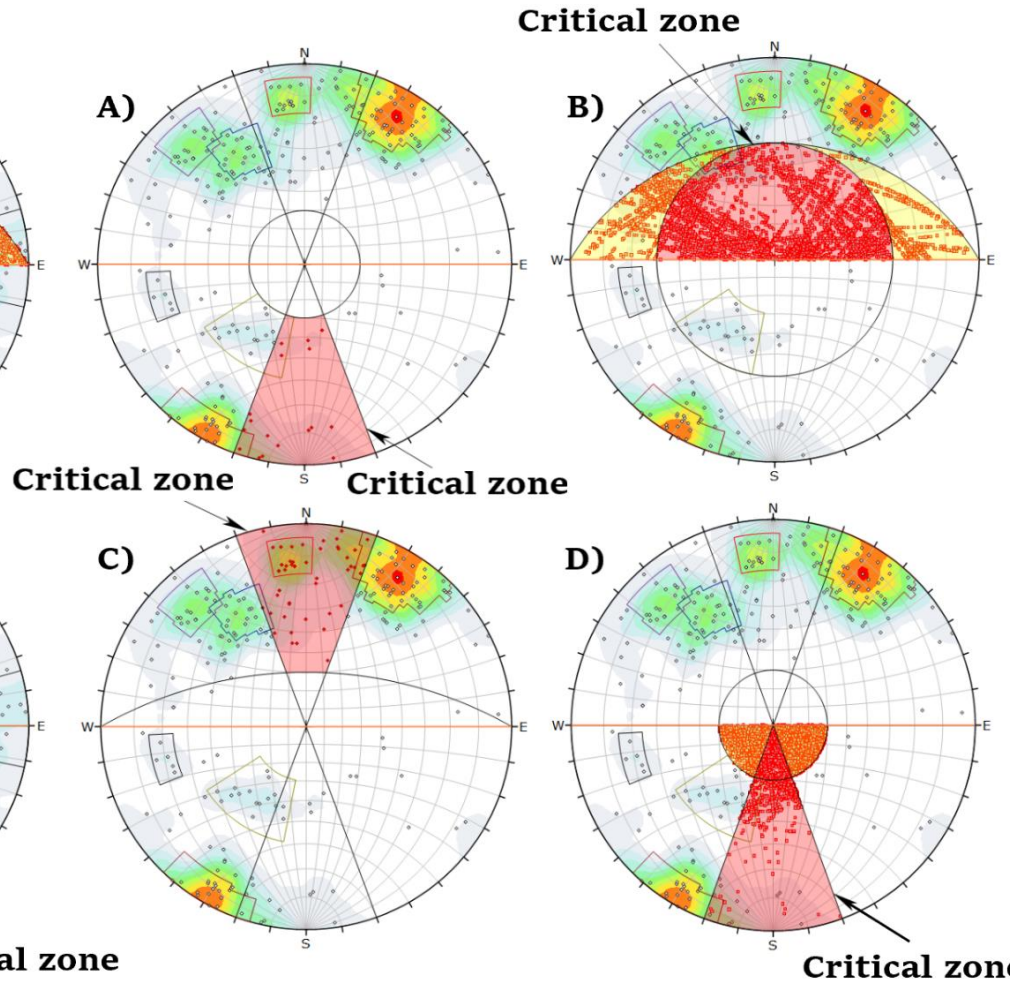

Figure 74. Kinematic analyses of the planar data of the southern sector using a 90° slope angle. (A) Planar sliding. (B) Wedge sliding. (C) Flexural Toppling. (D) Direct Toppling.

Stereonets constructed with the linear data (Figure 73) exhibit majority of sub-horizontal structures, where dominant fractures have an orientation of 17/350. Due to their relatively low dip, they do not represent a significant structural failure risk. As for the planar data structures, the greatest density concentrations are allocated in the NE quadrant, however, the structures are not found within the critical zone of any failure mode.

Table 17 presents the analyses results for the south sector (0° slope dip direction).

Table 17. Risk of planar, wedge, flexural toppling, and direct toppling failure modes.

	LINEAR DATA				PLANAR DATA			
	PLANAR	WEDGE	F. TOPPLING	D.TOPPLING	PLANAR	WEDGE	F. TOPPLING	D.TOPPLING
70°	7,77 %	16,88 %	3,59 %	5,27 %	2,13 %	9,70 %	19,15 %	9,72 %
75°	8,56 %	19,05 %	4,25 %	6,35 %	2,13 %	11,57 %	19,57 %	9,73 %
80°	9,58 %	20,59 %	4,84 %	7,64 %	4,26 %	15,28 %	20,43 %	9,73 %
85°	10,02 %	21,83 %	5,66 %	8,97 %	5,53 %	19,02 %	20,85 %	9,75 %
90°	10,02 %	**22,88 %**	6,63 %	10,50 %	7,23 %	**23,76 %**	20,85 %	9,77 %

Analyses indicate a low risk for planar sliding, which is not associated to any specific joint set. From the toppling modes, flexural toppling presents the highest risk, which is attributed to joint set 1m identified in the planar data. Wedge sliding presents the highest risk overall, where most of the critical intersections (Figure 75, Appendix's 10 and 11) correspond to interactions between structures of multi-bench scale (i.e., Set A intersecting with Set E and F). The risk for all failure modes remains consistent across the sector considering a ±20° range in the bench slopes azimuth (from kinematic sensitivity charts).

LINEAR DATA											PLANAR DATA						
SET	**1w**	**2w**	**3w**	**4w**	**5w**	**F**	**E**	**8w**	**A**	**I**	**SET**	**1m**	**2m**	**F**	**E**	**5m**	**A**
1w											**1m**						
2w											**2m**						
3w											**F**						
4w											**E**						
5w											**5m**						
F											**A**						
E																	
8w																	
A																	
I																	

Figure 75. Matrix of critical intersections of joint sets for wedge sliding. Intersections in primary critical zone (red). Intersections in secondary critical zone (yellow).

5.3.5 South East Sector

Dominant orientations of the minor discontinuities are presented in Table 18.

Table 18. Joint sets identified from the linear and planar data of the south east sector.

LINEAR DATA (871 JOINTS)					PLANAR DATA (444 JOINTS)				
SET	**DIP**	**DIP DIRECTION**	**# OF JOINTS**	**ID**	**SET**	**DIP**	**DIP DIRECTION**	**# OF JOINTS**	**ID**
1w	15	217	90		1m	78	144	53	SET E
2w	5	10	37		2m	86	155	22	
3w	12	285	27		3m	62	124	17	SET F
4w	36	30	54	SET A	4m	76	254	24	SET I
5w	79	73	19	SET B	5m	86	335	43	
6w	81	106	12	SET C	6m	54	28	13	SET A
7w	64	133	20	SET F	7m	80	76	35	SET B
8w	83	134	8	SET E					
9w	59	200	9	SET H					
10w	54	240	14						
11w	45	266	20						

The stereo nets constructed for the kinematic analyses are shown in Figure 76 and 77.

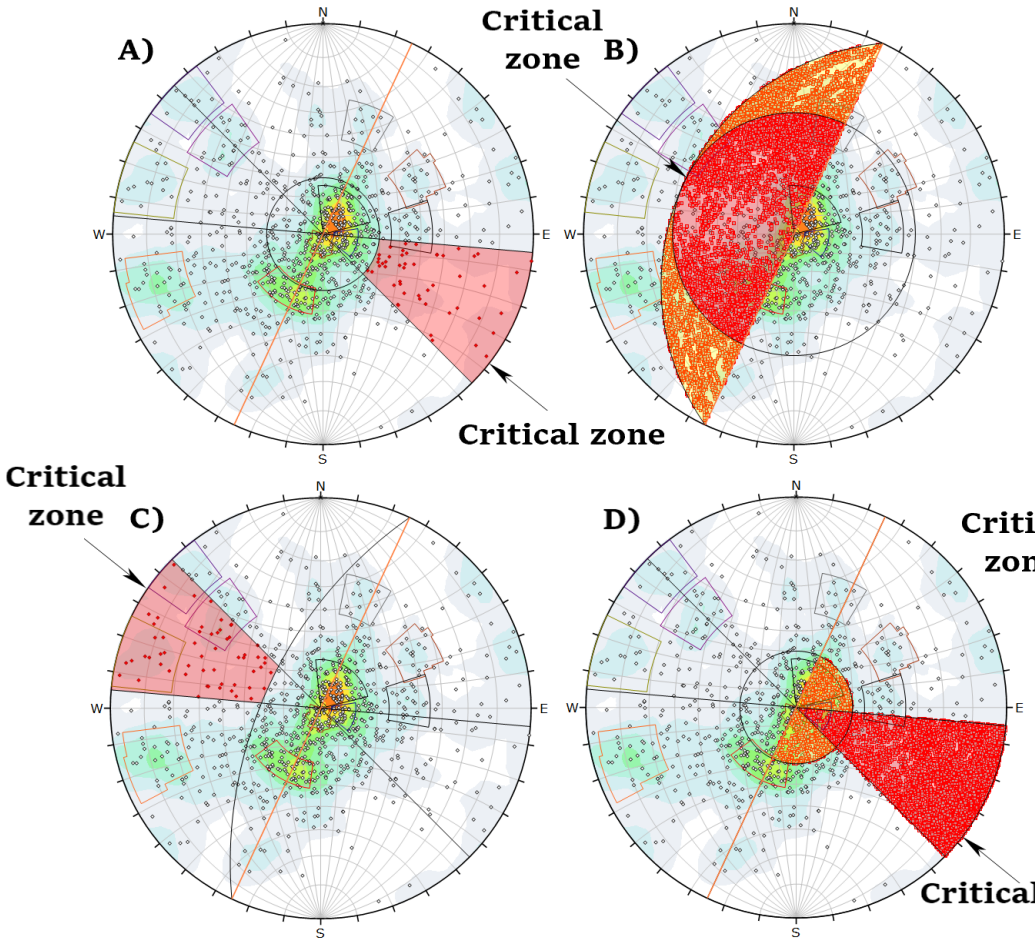

Figure 76. Kinematic analyses of the linear data of the southeastern sector using a 90° slope angle. (A) Planar sliding. (B) Wedge sliding. (C) Flexural Toppling. (D) Direct Toppling.

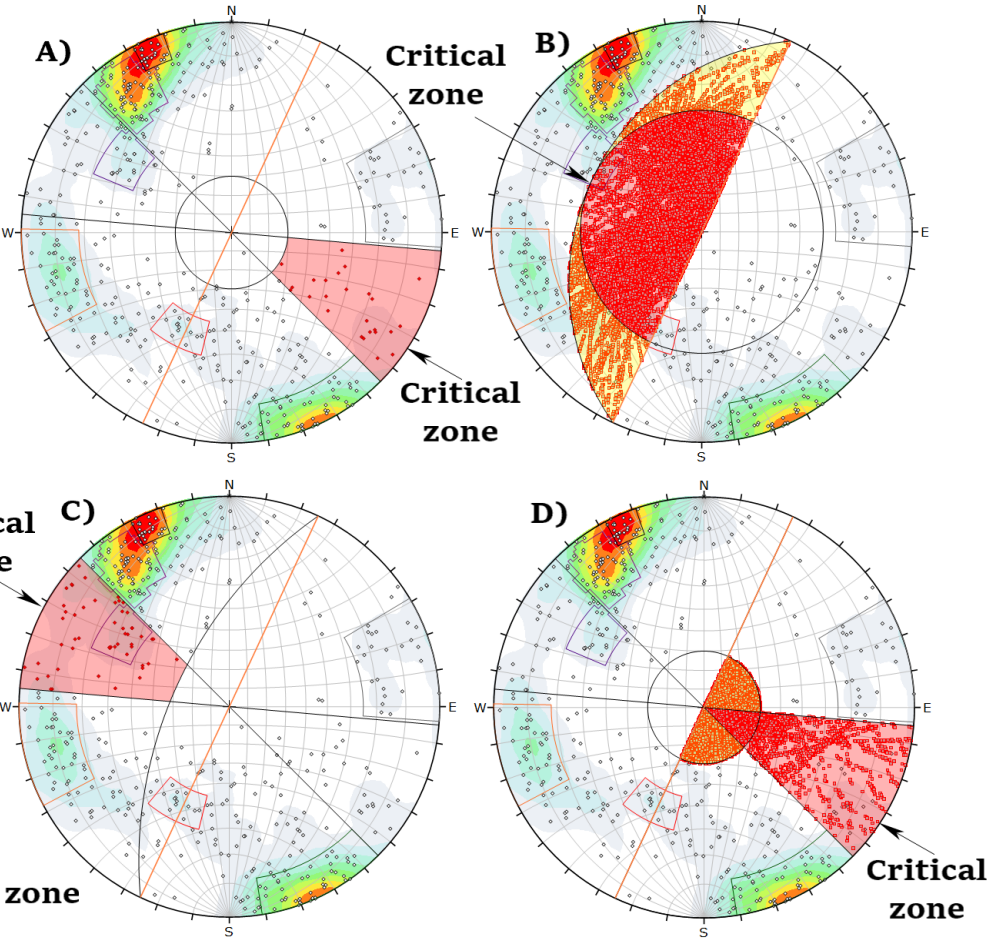

Figure 77. Kinematic analyses of the planar data of the southeastern sector using a 90° slope angle. (A) Planar sliding. (B) Wedge sliding. (C) Flexural Toppling. (D) Direct Toppling.

The greatest density concentrations of the linear data correspond to sub-horizontal structures allocated in the NE quadrant of the stereonets (Figure 76), that similarly to other sectors do not represent a structural failure risk. As for the planar data, the dominant structures correspond to steeply dipping fractures (Sets E and F). Linear data analyses suggest that the flexural toppling risk is associated to fractures dipping steeply towards the south east.

Table 19 presents the analyses results for the southeast sector (295° slope dip direction).

Table 19. Risk of planar, wedge, flexural toppling, and direct toppling failure modes.

	LINEAR DATA				PLANAR DATA			
	PLANAR	WEDGE	F. TOPPLING	D.TOPPLING	PLANAR	WEDGE	F. TOPPLING	D.TOPPLING
70°	3,94 %	12,56 %	6,04 %	3,82 %	2,70 %	12,85 %	10,59 %	8,53 %
75°	4,97 %	14,22 %	6,65 %	4,79 %	3,15 %	16,58 %	11,49 %	8,60 %
80°	5,09 %	15,78 %	6,90 %	6,01 %	4,50 %	20,46 %	11,49 %	8,69 %
85°	5,43 %	17,39 %	7,59 %	7,43 %	4,73 %	24,84 %	11,71 %	8,78 %
90°	6,36 %	**19,47 %**	7,75 %	9,89 %	5,63 %	**29,88 %**	11,71 %	8,86 %

Results from both linear data and planar data indicate a low risk for planar sliding and direct toppling (<10%). Flexural toppling risk is moderately low as well, however is associated to joint sets C, E, and F. Wedge failure mode presents the highest failure risk, specially from the planar data structures. Kinematic sensitivity charts indicate that the risk for wedge sliding and flexural toppling increases towards the north east area of the sector (benches dip direction >300°), while the planar sliding and direct toppling risk stays consistent within a ±20° range. Figure 78 presents the matrix of critical intersections for wedge sliding at 90° slope dip (stereo nets in Appendix 12 and 13).

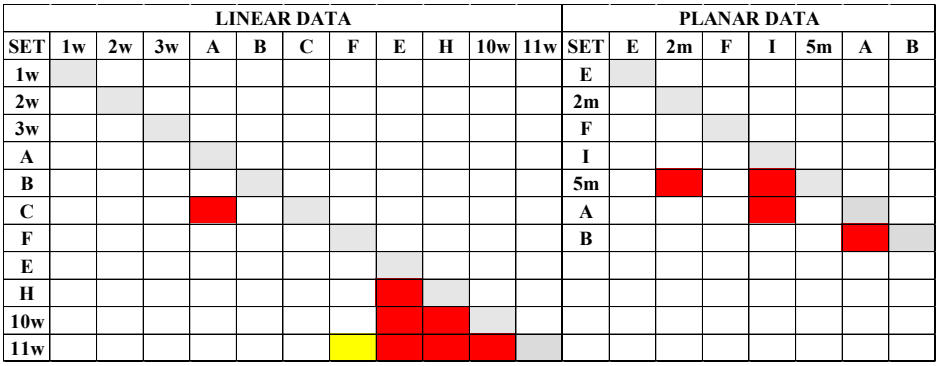

Figure 78. Matrix of critical intersections of joint sets for wedge sliding. Intersections in primary critical zone (red). Intersections in secondary critical zone (yellow).

5.3.6 South West Sector

Dominant orientations of the minor discontinuities are presented in Table 20.

Table 20. Joint sets identified from the linear and planar data of the south east sector.

LINEAR DATA (678 JOINTS)					PLANAR DATA (257 JOINTS)				
SET	DIP	DIP DIRECTION	# OF JOINTS	ID	SET	DIP	DIP DIRECTION	# OF JOINTS	ID
1w	11	313	44		1m	78	122	47	SET E
2w	6	169	13		2m	74	91	30	
3w	28	206	52		3m	80	33	18	
4w	58	204	18	SET G/H	4m	40	38	8	SET A
5w	80	229	18		5m	81	268	19	SET I
6w	89	136	10	SET E	6m	47	236	8	
7w	86	107	16	SET C	7m	54	210	6	SET G
8w	31	122	15		8m	79	215	10	
9w	83	71	12	SET B					
10w	35	44	31	SET A					
11w	43	246	20						

The stereo nets constructed for the kinematic analyses are shown in Figure 79 and 80.

fd

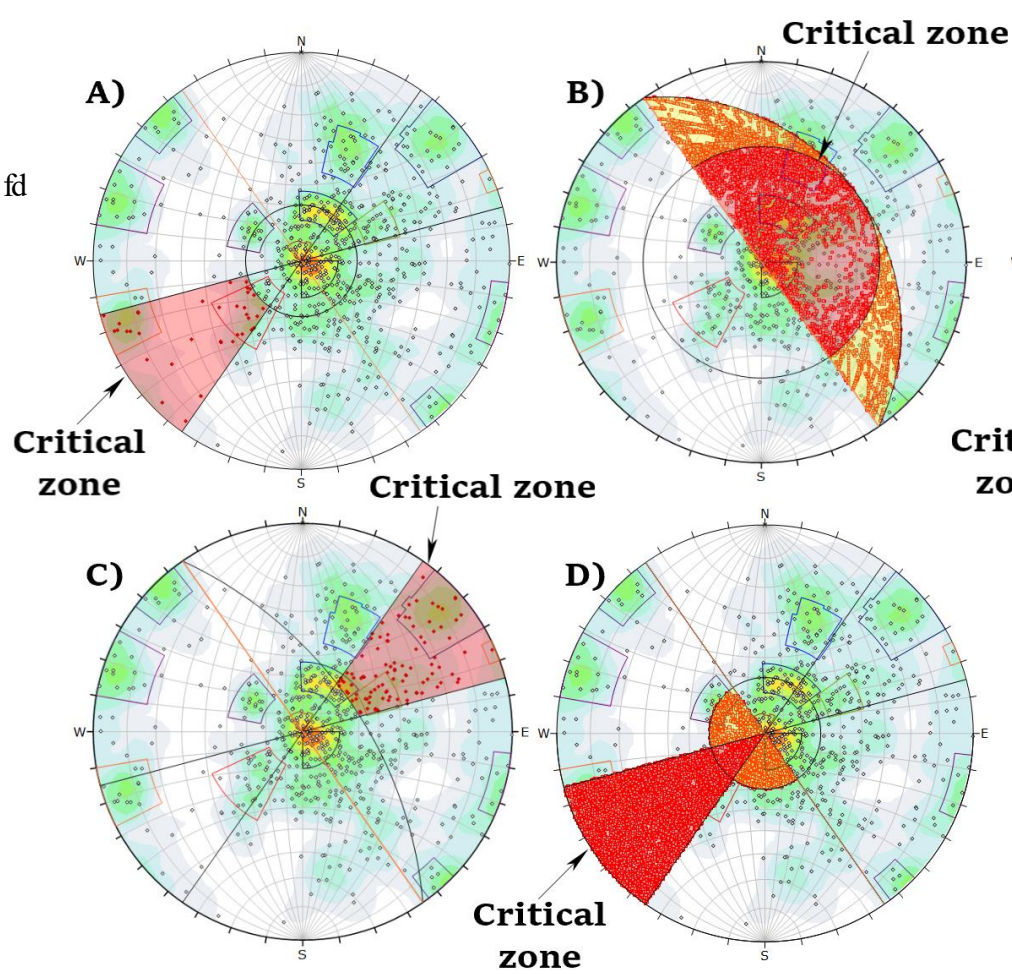

Figure 79. Kinematic analyses of the linear data of the southwestern sector using a 90° slope angle. (A) Planar sliding. (B) Wedge sliding. (C) Flexural Toppling. (D) Direct Toppling.

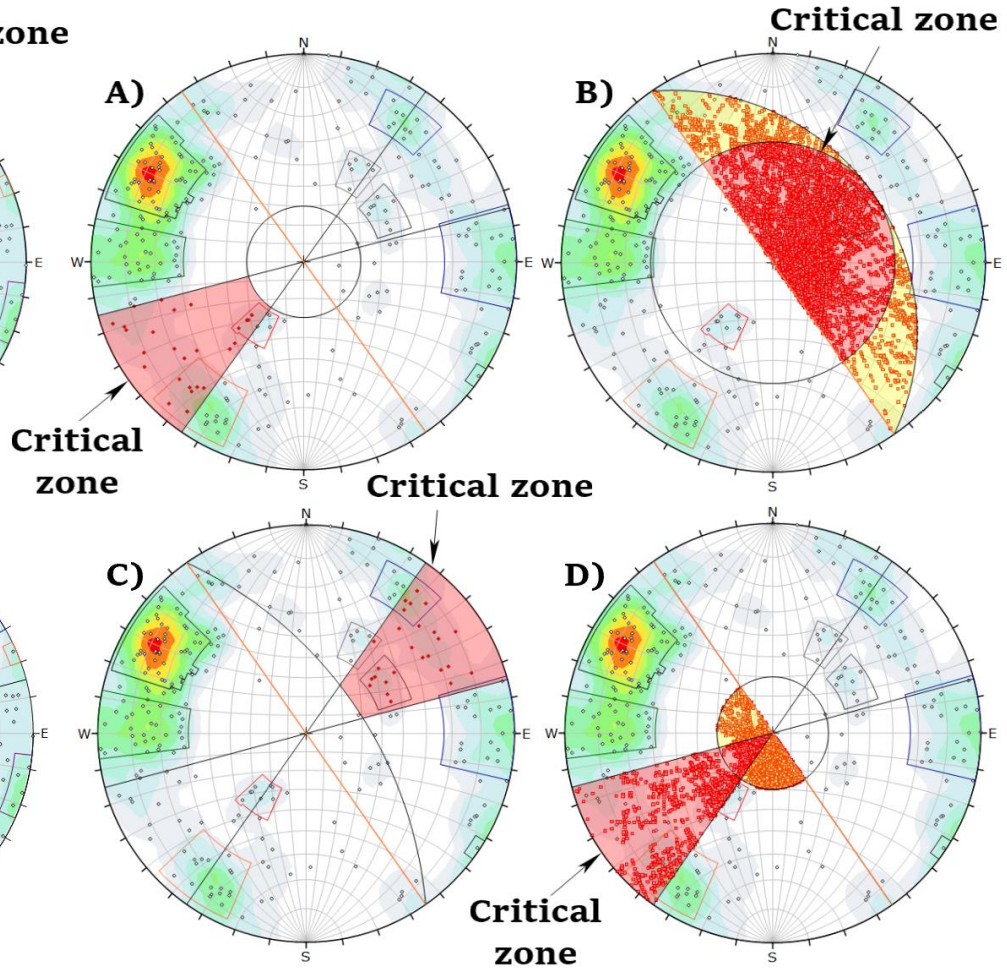

Figure 80. Kinematic analyses of the planar data of the southwestern sector using a 90° slope angle. (A) Planar sliding. (B) Wedge sliding. (C) Flexural Toppling. (D) Direct Toppling.

Structures from the linear data correspond mostly to fractures dipping shallowly towards the south west, whereas structures from the planar data are dominantly steeply dipping fractures that dip towards the south east. Kinematic analyses from both linear data and planar data suggest a risk for planar sliding and flexural toppling from Sets A and Set G, respectively. However, the structures density is low.

Table 21 presents the analyses results for the southwest sector (55° slope dip direction).

Table 21. Risk of planar, wedge, flexural toppling, and direct toppling failure modes.

	LINEAR DATA				PLANAR DATA			
	PLANAR	WEDGE	F. TOPPLING	D.TOPPLING	PLANAR	WEDGE	F. TOPPLING	D.TOPPLING
70°	4,04 %	10,11 %	8,81 %	6,84 %	3,50 %	20,15 %	7,39 %	4,58 %
75°	4,04 %	11,33 %	9,67 %	7,97 %	4,67 %	26,55 %	9,34 %	4,82 %
80°	5 %	13,08 %	10,30 %	9,22 %	7,39 %	33,11 %	10,12 %	5,09 %
85°	5,90 %	14,99 %	11,77 %	10,57 %	9,34 %	39,79 %	10,12 %	5,35 %
90°	7,39 %	**17,05 %**	13,16 %	12,11 %	10,12 %	**44,74 %**	10,12 %	5,55 %

Results indicate a low risk for planar sliding. However, the risk is associated to Set A (recognized to have a multi-bench condition). Direct toppling presents a low risk as well that is consistent over the different bench angles analyzed. Flexural toppling presents a moderate risk which is associated to Set G and H. Similar to other sectors, wedge sliding presents the highest risk, especially for the planar data structures. Kinematic sensitivity charts indicate that the risk for planar sliding and flexural toppling remains consistent despite variations in the benches azimuth, while the risk for wedge sliding and direct toppling increases towards the south of the sector. Figure 81 presents the matrix of critical intersections for wedge sliding at 90° slope dip (stereo nets in Appendix 14 and 15).

LINEAR DATA												PLANAR DATA								
SET	1w	2w	3w	G/H	5w	E	C	8w	B	A	11w	SET	E	2m	3m	A	I	6m	G	8m
1w												E								
2w												2m								
3w												3m								
G/H												A								
5w												I								
E												6m								
C												G								
8w												8m								
B																				
A																				
11w																				

Figure 81. Matrix of critical intersections of joint sets for wedge sliding. Intersections in primary critical zone (red). Intersections in secondary critical zone (yellow).

5.4 Inter-ramp Slope Scale Stability Analysis

The stability analysis at inter-ramp scale entails the evaluation of planar and wedge failure modes through stereo nets constructed using an equal angle projection. A friction angle of 27° was used for the analyses, which corresponds to the mean friction angle value estimated by Zhang et al. (2018) for structures with talc infill/alteration. This approach was taken to consider the effect of major structures with talc infill/enrichment (e.g., NE-flt-rv1). The following results highlight the inter-ramp slopes from each sector where potential instabilities were identified, which are raised by the effect of intermediate structures (multi-bench persistence joints) and major structures.

5.4.1 North Sector

The analyses of the north sector (180° slope dip direction) consider joint sets A, D, E, F, and G as intermediate structures (indicated in Table 10).

(1) Upper Inter-ramp (above -10mRL, ~51° IRA)

The major structures interacting with the inter-ramp slope and their local orientation are presented in Table 22.

Table 22. Major structures interacting with upper inter-ramp, north sector.

STRUCTURE	DIP	DIP DIRECTION
NE-flt-rv1	37	292
NS-flt-1	79	91
NS-flt-2	67	96
NS-flt-3	62	96

Results from kinematic analyses are summarized in Figure 82. No structure was recognized to have a potential to trigger a planar failure. Set G was recognized to represent a risk for the slope stability as it can potentially generate wedge failures with major, north-south trending structures (stereo net for wedge sliding in Appendix 16).

		Critical intersection for Wedge sliding								
	STRUCTURE	NS-flt-1	NS-flt-2	NS-flt-3	NE-flt-rv1	SET A	SET D	SET E	SET F	SET G
Potential for Planar sliding	NS-flt-1									
	NS-flt-2									
	NS-flt-3									
	NE-flt-rv1									
	SET A									
	SET D									
	SET E									
	SET F									
	SET G									

Figure 82. Matrix of planar and wedge failure assessment. Critical intersection between structures for wedge sliding (red).

(2) Middle Inter-ramp (-31mRL to -174mRL, ~56° IRA)

The major structures interacting with the inter-ramp slope and their local orientation are presented in Table 23.

Table 23. Major structures interacting with middle inter-ramp, north sector.

STRUCTURE	DIP	DIP DIRECTION
NS-flt-2	66	89
NS-flt-3	70	95
ENE-flt-1	65	310

Results from kinematic analyses are summarized in Figure 83. No structure was recognized to have a potential to trigger a planar failure. Sets G and D can potentially generate wedge failures with major, north-south trending structures (stereo net for wedge sliding in Appendix 17). However, the actual presence of these major structures in the slope is very limited i.e., risk is very low.

		Critical intersection for Wedge sliding							
	STRUCTURE	NS-flt-2	NS-flt-3	ENE-flt-1	SET A	SET D	SET E	SET F	SET G
Potential for Planar sliding	NS-flt-2								
	NS-flt-3								
	ENE-flt-1								
	SET A								
	SET D								
	SET E								
	SET F								
	SET G								

Figure 83. Matrix of planar and wedge failure assessment. Critical intersection between structures for wedge sliding (red).

5.4.2 North East Sector

The analyses of the north east sector (235° slope dip direction) consider joint sets D, E, F, and G as intermediate structures (indicated in Table 12).

(1) Upper Inter-ramp (above +18mRL, ~57° IRA)

The major structures interacting with the inter-ramp slope and their local orientation are presented in Table 24.

Table 24. Major structures interacting with upper inter-ramp, north east sector.

STRUCTURE	DIP	DIP DIRECTION
ENE-flt-1	54	316
NE-flt-2	61	294
EW-flt-1	84	181

Results from kinematic analyses are summarized in Figure 84. Set G is recognized to have a significant impact in the slope stability as it can potentially trigger a planar failure towards the north of the slope; and can additionally generate wedge failures with other intermediate and major structures (stereo nets for planar and wedge sliding in Appendix 18 and 19). Major structures ENE-flt-1 and EW-flt-1 present a critical intersection for wedge sliding, however, the actual "wedge" lays in the mined-out area of the Stage 5 pit, meaning that the risk is very low and/or null.

		Critical intersection for Wedge sliding						
	STRUCTURE	ENE-flt-1	NE-flt-2	EW-flt-1	SET D	SET E	SET F	SET G
Potential for Planar sliding	ENE-flt-1							
	NE-flt-2							
	EW-flt-1							
	SET D							
	SET E							
	SET F							
	SET G							

Figure 84. Matrix of planar and wedge failure assessment. Potential for planar sliding (blue). Critical intersection between structures for wedge sliding (red). Critical intersection with low/null risk (green).

(2) Upper-Middle Inter-ramp (+55mRL to -85mRL, ~60° IRA).

The major structures interacting with the inter-ramp slope and their local orientation are presented in Table 25.

Table 25. Major structures interacting with upper-middle inter-ramp, north east sector.

STRUCTURE	DIP	DIP DIRECTION
NE-flt-2	58	293
EW-flt-1	83	178

Results from kinematic analyses are summarized in Figure 85. Similar to the upper inter-ramp, Set G has potential to develop a planar failure, and additionally generate wedge failures with other intermediate and major structures. Major structures NE-flt-2 and EW-flt-1 present a critical intersection for wedge sliding (stereo net for wedge sliding in Appendix 20).

		Critical intersection for Wedge sliding					
	STRUCTURE	NE-flt-2	EW-flt-1	SET D	SET E	SET F	SET G
Potential for Planar sliding	NE-flt-2						
	EW-flt-1						
	SET D						
	SET E						
	SET F						
	SET G						

Figure 85. Matrix of planar and wedge failure assessment. Potential for planar sliding (blue). Critical intersection between structures for wedge sliding (red).

The intersection of structures NE-flt-2 and EW-flt-1 is displayed in Figure 86. This potential wedge-type failure is of high risk and volume, which represents a major threat for the Stage 5 pit and the northeast wall. If failure occurs, it could result in loss of all geotechnical structures location within the +53mRL to -83mRL level (including the haulage road/ramp located below the slope). Furthermore, the identification of this wedge

structure acknowledges a risk for the inter-ramp slopes above, as the point of intersection of the two discontinuities is located at the crest of the overall slope.

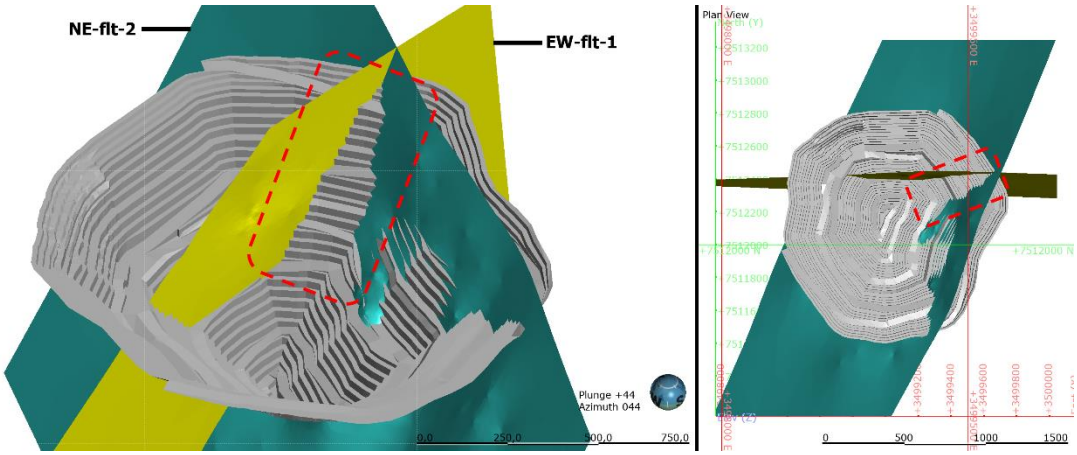

Figure 86. 3D view of Stage 5. Potential wedge failure between NE-flt-2 and EW-flt-1.

(3) Lower-Middle Inter-ramp (-78mRL to -148mRL, ~64° IRA)

The major structures interacting with the inter-ramp slope and their local orientation are presented in Table 26.

Table 26. Major structures interacting with lower-middle inter-ramp.

STRUCTURE	DIP	DIP DIRECTION
EW-flt-1	88	176
NE-flt-2	63	102

Results are summarized in Figure 87. Potential risks are similar to in previous slopes i.e., risk of planar and wedge sliding from Set G.

		Critical intersection for Wedge sliding					
	STRUCTURE	EW-flt-1	NS-flt-2	SET D	SET E	SET F	SET G
Potential for Planar sliding	EW-flt-1						
	NS-flt-2						
	SET D						
	SET E						
	SET F						
	SET G						

Figure 87. Matrix of planar and wedge failure assessment. Potential for planar sliding (blue). Critical intersection between structures for wedge sliding (red).

(4) Lower Inter-ramp (-289mRL to -153mRL, ~59° IRA)

The major structures interacting with the inter-ramp slope and their local orientation are presented in Table 27.

Table 27. Major structures interacting with lower inter-ramp, north east sector.

STRUCTURE	DIP	DIP DIRECTION
NS-flt-2	64	96
NS-flt-3	68	92

Results are summarized in Figure 88. Potential risks are similar to in previous slopes i.e., risk of planar and wedge sliding from Set G.

		Critical intersection for Wedge sliding					
	STRUCTURE	NS-flt-2	NS-flt-3	SET D	SET E	SET F	SET G
Potential for Planar sliding	NS-flt-2						
	NS-flt-3						
	SET D						
	SET E						
	SET F						
	SET G						

Figure 88. Matrix of planar and wedge failure assessment. Potential for planar sliding (blue). Critical intersection between structures for wedge sliding (red).

5.4.3 North West Sector

The analyses of the northwest Sector (105° slope dip direction) consider joint sets A, D, E, F, and G as intermediate structures (indicated in Table 14).

(1) Upper Inter-ramp (above -6mRL, ~52° IRA)

The major structures interacting with the inter-ramp slope and their local orientation are presented in Table 28.

Table 28. Major structures interacting with upper inter-ramp, north west sector.

STRUCTURE	DIP	DIP DIRECTION
NS-flt-5	72	86

The analysis of the upper inter-ramp additionally evaluates an 140° slope dip direction to take into account the inter-ramp slope identified in the northwest corner of the Stage 5 pit (as detailed in section 4.1) which is being intersected by structure NS-flt-5.

Analyses at 105° slope dip direction indicate a daylighting condition of structures NS-flt-5 and Set D (stereo net for planar sliding in Appendix 21). However, they dip at a steeper angle than the slope face. This means that the risk is low but should not be discarded. These two structures generate a critical intersection for wedge sliding as well. Results are summarized in Figure 89.

		Critical intersection for Wedge sliding					
	STRUCTURE	NS-flt-5	SET A	SET D	SET E	SET F	SET G
Potential for Planar sliding	NS-flt-5						
	SET A						
	SET D						
	SET E						
	SET F						
	SET G						

Figure 89. Matrix of planar and wedge failure assessment. Potential for planar sliding (blue). Critical intersection between structures for wedge sliding (red).

Figure 90 indicates the area of influence for planar sliding generated by the effect of NS-flt-5 and a potential joint plane from Set D.

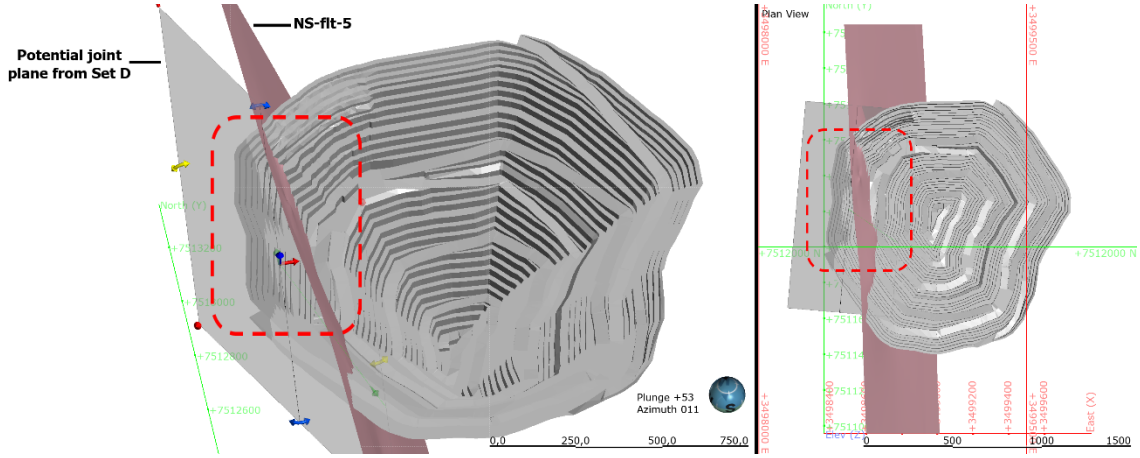

Figure 90. 3D view of Stage 5 pit. Potential planar failure produced by NS-flt-5 and joint plane from Set D.

In contrast, analyses at 140° slope dip direction indicate a daylighting condition of structures Sets E and F, however, they dip at a steeper angle than the slope face as well. Results are summarized in Figure 91.

		Critical intersection for Wedge sliding					
	STRUCTURE	NS-flt-5	SET A	SET D	SET E	SET F	SET G
Potential for Planar sliding	NS-flt-5						
	SET A						
	SET D						
	SET E						
	SET F						
	SET G						

Figure 91. Matrix of planar and wedge failure assessment. Potential for planar sliding (blue). Critical intersection between structures for wedge sliding (red).

(2) Middle Inter-ramp (-6mRL to -210mRL, ~58° IRA).

The major structures interacting with the inter-ramp slope and their local orientation are presented in Table 29.

Table 29. Major structures interacting with middle inter-ramp, north west sector.

STRUCTURE	DIP	DIP DIRECTION
NS-flt-1	73	93
EW-flt-1	83	182
ENE-flt-1	71	313

Results from kinematic analyses are summarized in Figure 92. Structures NS-flt-1 and Set D are recognized to have a daylight condition with the slope. However, they dip steeper than the slope face, which means that the risk for planar failure is low but should not be discarded. An additional critical intersection between joint sets was identified.

		Critical intersection for Wedge sliding							
	STRUCTURE	NS-flt-1	EW-flt-1	ENE-flt-1	SET A	SET D	SET E	SET F	SET G
Potential for Planar sliding	NS-flt-1								
	EW-flt-1								
	ENE-flt-1								
	SET A								
	SET D								
	SET E								
	SET F								
	SET G								

Figure 92. Matrix of planar and wedge failure assessment. Potential for planar sliding (blue). Critical intersection between structures for wedge sliding (red).

5.4.4 South Sector

The analyses of the south sector (0° slope dip direction) consider joint sets A, E, and F as intermediate structures (indicated in Table 16).

(1) Upper Inter-ramp (above +153mRL, ~53° IRA)

The major structures interacting with the inter-ramp slope and their local orientation are presented in Table 30.

Table 30. Major structures interacting with upper inter-ramp, south sector.

STRUCTURE	DIP	DIP DIRECTION
NE-flt-2	58	302
NE-flt-rv1	39	291
NS-flt-1	75	89
NS-flt-2	74	78
NS-flt-3	68	81
Splay-flt-010	78	75

Results are presented in Figure 93. No structure represents a risk for triggering a planar failure. Multiple critical intersections for wedge-type failures are identified (stereo net for wedge sliding can be found in Appendix 22) where sliding involves structures from the vein system (NS-flt-1, NS-flt-2, NS-flt-3, and Splay-flt-010).

		Critical intersection for Wedge sliding								
	STRUCTURE	NE-flt-2	NE-flt-rv1	NS-flt-1	NS-flt-2	NS-flt-3	Splay-flt-010	SET A	SET E	SET F
Potential for Planar sliding	NE-flt-2									
	NE-flt-rv1									
	NS-flt-1									
	NS-flt-2									
	NS-flt-3									
	Splay-flt-010									
	SET A									
	SET E									
	SET F									

Figure 93. Matrix of planar and wedge failure assessment. Critical intersection between structures for wedge sliding (red). Critical intersection with low/null risk (green).

The intersection of NE-flt-2 with NS-flt-2, NS-flt-3, and Splay-flt-010 generates adjacent wedge blocks of relatively low volume near to the crest of the south wall. If failure of these blocks occurs simultaneously, it may endanger the geotechnical structures found within the +248mRL to 113mRL level, and the haulage roads located below the inter-ramp slope. In contrast, intersection between NE-flt-2 and NS-flt-1 is of low/null risk, as the wedge formed lays far from the other wedge blocks and the boundary of the pit. Figure 94 presents the area of influence of the intersections.

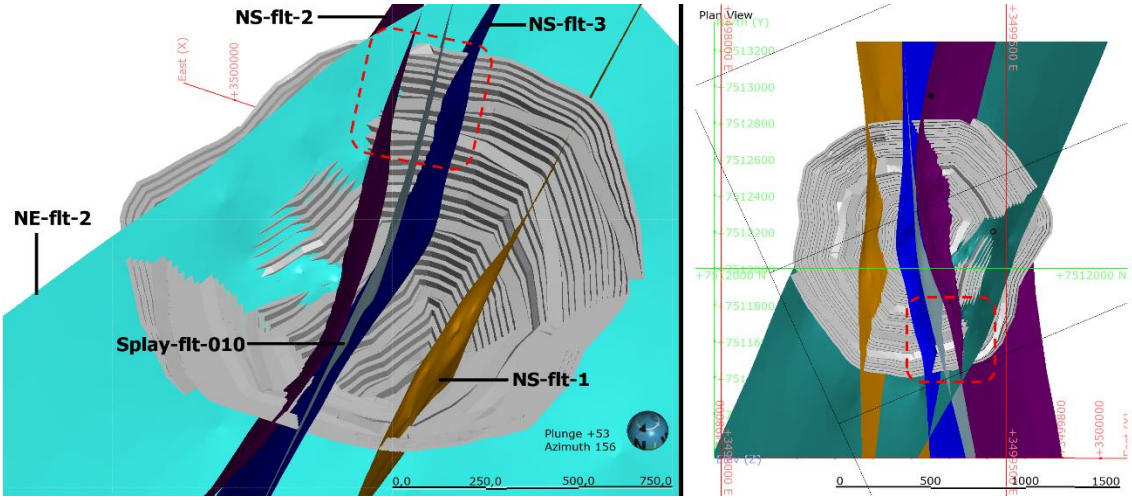

Figure 94. 3D view of Stage 5 pit. Potential wedge failures produced by the intersection of NE-flt-2 with NS-flt-2, NS-flt-3, and Splay-flt-010.

(2) Middle Inter-ramp (+90mRL to -98mRL, ~57° IRA)

The major structures interacting with the inter-ramp slope and their local orientation are presented in Table 31.

Table 31. Major structures interacting with middle inter-ramp, south sector.

STRUCTURE	DIP	DIP DIRECTION
NE-flt-2	60	282
NS-flt-2	76	74
NS-flt-3	70	81
Splay-flt-010	77	75

Results are presented in Figure 95. Wedge sliding analysis indicate multiple critical intersections between NE-flt-2 and structures from the vein system. This suggests that the area of influence presented in Figure 95 may extend up to the -106mRL haulage road, representing a threat for the stability of the overall slope.

		Critical intersection for Wedge sliding						
	STRUCTURE	NE-flt-2	NS-flt-2	NS-flt-3	Splay-flt-010	SET A	SET E	SET F
Potential for Planar sliding	NE-flt-2							
	NS-flt-2							
	NS-flt-3							
	Splay-flt-010							
	SET A							
	SET E							
	SET F							

Figure 95. Matrix of planar and wedge failure assessment. Critical intersection between structures for wedge sliding (red). Critical intersection with low/null risk (green).

5.4.5 South East Sector

The analyses of the south east sector (295° slope dip direction) consider joint sets A, E, and F as intermediate structures (indicated in Table 18).

(1) Middle Inter-ramp (+95mRL to -112mRL, ~56° IRA)

The major structures interacting with the inter-ramp slope and their local orientation are presented in Table 32.

Table 32. Major structures interacting with middle inter-ramp, south east sector.

STRUCTURE	DIP	DIP DIRECTION
NE-flt-2	45-53	293
NS-flt-2	73	72

Results from the analyses are presented in Figure 96. Planar sliding evaluation exhibits a high risk for planar failure from structure NE-flt-2 (stereo net in Appendix 23) as the structure daylights the slope face and additionally dips at a lower angle than the slope, fulfilling the main geometric requirements for developing a planar failure. Wedge sliding analysis additionally exhibits a critical intersection between NE-flt-2 and NS-flt-2.

		Critical intersection for Wedge sliding				
	STRUCTURE	NE-flt-2	NS-flt-2	SET A	SET E	SET F
Potential for Planar sliding	NE-flt-2					
	NS-flt-2					
	SET A					
	SET E					
	SET F					

Figure 96. Matrix of planar and wedge failure assessment. Potential for planar sliding (blue). Critical intersection between structures for wedge sliding (red).

The effect of NE-flt-2 in the inter-ramp slope is critical for the design and development of the Stage 5 pit (Figure 97). If planar failure were to occur, it could endanger all geotechnical structures below the +90mRL level. This means that the impact could extend to the overall-slope scale. Additionally, its intersection with NS-flt-2 represents a potential wedge failure that could impact both the south and south eastern walls.

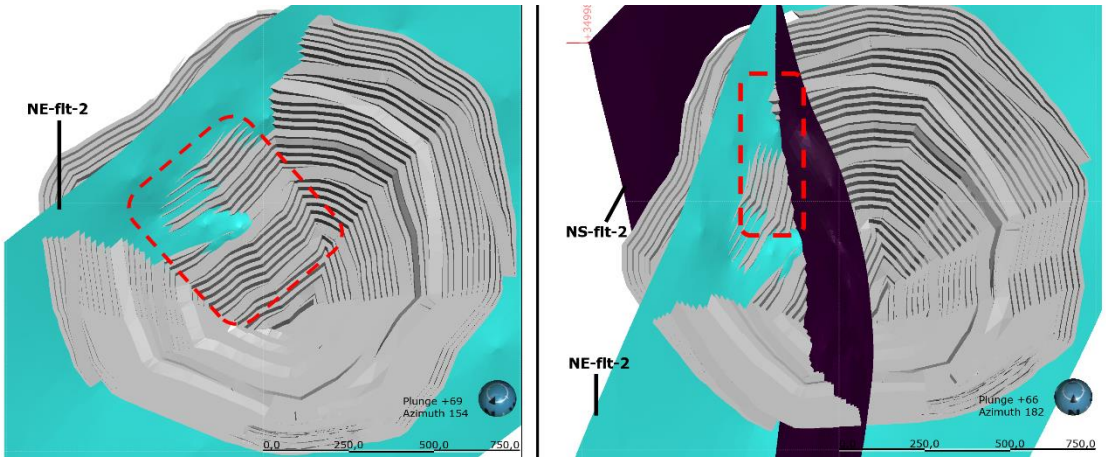

Figure 97. 3D view of Stage 5 pit. Potential planar failure from NE-flt-2 (left). Potential wedge failure produced by the intersection of NE-flt-2 with NS-flt-2 (right).

5.4.6 South West Sector

The analyses of the southwest sector (55° slope dip direction) consider joint sets A, E, F, and G as intermediate structures (indicated in Table 20).

(1) Upper Inter-ramp (+225mRL to +25mRL, ~52° IRA).

The major structures interacting with the inter-ramp slope and their local orientation are presented in Table 34.

Table 34. Major structures interacting with upper inter-ramp, south west sector.

STRUCTURE	DIP	DIP DIRECTION
ENE-flt-1	62	320
NS-flt-5	71	87
NE-flt-rv1	38	291

Results are summarized in Figure 98. Set A represents a risk for the inter-ramp as it has a potential to generate planar failures towards the south of the slope (dip direction shifts slightly to 50°). Additionally, it can generate wedge failures with set Set E and F, which are major-systematic joints. A critical intersection between NS-flt-5 and ENE-flt-1 was identified (stereo net in Appendix 24), however, the point of intersection is located in the mined-out area of the pit, meaning that the risk is low/null for the inter-ramp slope.

		Critical intersection for Wedge sliding						
	STRUCTURE	ENE-flt-1	NS-flt-5	NE-flt-rv1	SET A	SET E	SET F	SET G
Potential for Planar sliding	ENE-flt-1							
	NS-flt-5							
	NE-flt-rv1							
	SET A							
	SET E							
	SET F							
	SET G							

Figure 98. Matrix of planar and wedge failure assessment. Potential for planar sliding (blue). Critical intersection between structures for wedge sliding (red). Critical intersection with low/null risk (green).

(2) Upper-Middle Inter-ramp (+62mRL to -82mRL, ~57° IRA)

The major structures interacting with the inter-ramp slope and their local orientation are presented in Table 35.

Table 35. Major structures interacting with upper-middle inter-ramp, south west sector.

STRUCTURE	DIP	DIP DIRECTION
ENE-flt-1	66	325
NS-flt-5	72	83
NS-flt-1	71	94

Results are summarized in Figure 99. The main risk of the inter-ramp slope is the development of wedge-type failures caused by the intersection of Set A with intermediate and major structures. A critical intersection between NS-flt-1 and ENE-flt-1 is identified, however, the point of intersection is located in the mined-out area of the pit, meaning that the risk is low/null for the inter-ramp slope.

		Critical intersection for Wedge sliding						
	STRUCTURE	ENE-flt-1	NS-flt-5	NS-flt-1	SET A	SET E	SET F	SET G
Potential for Planar sliding	ENE-flt-1							
	NS-flt-5							
	NS-flt-1							
	SET A							
	SET E							
	SET F							
	SET G							

Figure 99. Matrix of planar and wedge failure assessment. Potential for planar sliding (blue). Critical intersection between structures for wedge sliding (red). Critical intersection with low/null risk (green).

(3) Lower-Middle Inter-ramp (-82mRL to -238mRL, ~58° IRA)

The major structures interacting with the inter-ramp slope and their local orientation are presented in Table 36.

Table 36. Major structures interacting with lower-middle inter-ramp, south west sector.

STRUCTURE	DIP	DIP DIRECTION
NS-flt-1	75	86

Similar to the other inter-ramp slopes from the south west sector, the main potential instabilities for planar and wedge failure mode are raised by Set A (Figure 100).

		Critical intersection for Wedge sliding				
	STRUCTURE	NS-flt-1	SET A	SET E	SET F	SET G
Potential for Planar sliding	NS-flt-1					
	SET A					
	SET E					
	SET F					
	SET G					

Figure 100. Matrix of planar and wedge failure assessment. Potential for planar sliding (blue). Critical intersection between structures for wedge sliding (red).

5.5 Overall Slope Scale Stability Analysis

The stability analysis at overall scale examines the critical conditions of the major structures in the overall slopes (i.e., designated sectors). This by evaluating planar and wedge failure modes in stereo nets of equal angle projection. A friction angle of 27° was used for the analyses to consider the effect of structures with talc infill/enrichment (Zhang et al., 2018). For each wall the overall slope angle (OSA) was measured from the Stage 5 pit design.

5.5.1 North Sector

The structures considered for the analysis of the north wall are presented in table 37.

Table 37. Major structures interacting with the north wall.

STRUCTURE	DIP	DIP DIRECTION
EW-flt-1	82	183
NE-flt-rv1	35	291
NS-flt-1	79	91
NS-flt-2	67	99
NS-flt-3	65	93
ENE-flt-1	64	315

The evaluation of planar and wedge failure modes (~47° OSA) is presented in Figure 101.

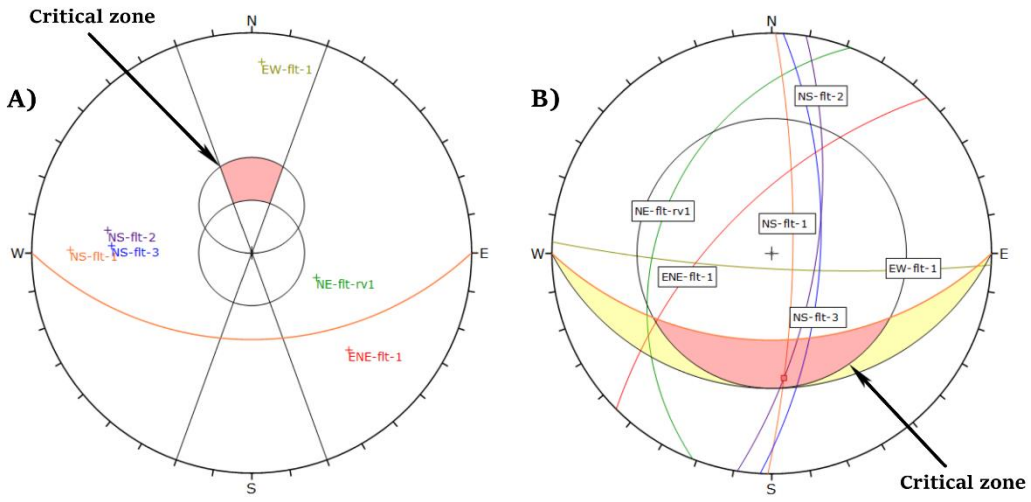

Figure 101. Kinematic analyses of the north wall. (A) Planar sliding. (B) Wedge sliding.

Results from the kinematic analyses only indicate one critical condition from the structures, which corresponds to the intersection between NS-flt-1 and NS-flt-2 for wedge sliding. However, their point of intersection is not within the pit layout, which means that the risk is low and/or null for the slope stability.

In addition, the stereo nets exhibit that structure EW-flt-1 has a daylighting condition with the slope. EW-flt-1 is a fault with geochemical signature that is intercepting almost perpendicularly the ramp located in the -187mRL to -163mRL level. Although the fault does not fullfill all geometrical requirements for planar sliding (as it dips steeper than the slope), it still represents a zone of weakness and instability that could lead to potential rock mass movement under varying stress conditions (e.g., ground water, drill and blast disturbance). If failure ocurrs along the structure plane, it may lead to loss of all geotechnical structures below the -163mRL level (Figure 102). Therefore, its potential risk should not be discarded, and additional geotechnical investigations should be

conducted with the purpose of understanding if there is need to modify the design of the ramp and/or slope.

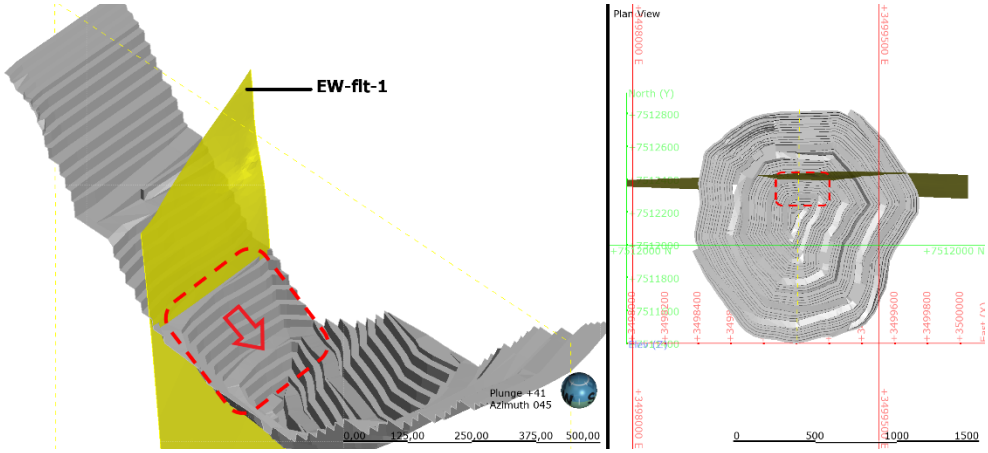

Figure 102. Slice of 3D view of Stage 5 pit. Potentil planar failure from EW-flt-1 in the north wall.

5.5.2 North East Sector

The structures considered for the analysis of the north east wall are presented in table 38.

Table 38. Major structures interacting with the north east wall.

STRUCTURE	DIP	DIP DIRECTION
EW-flt-1	83	181
NS-flt-2	64	96
NS-flt-3	68	92
ENE-flt-1	54	316
NE-flt-2	61	294

The evaluation of planar and wedge failure modes (~46° OSA) is presented in Figure 103.

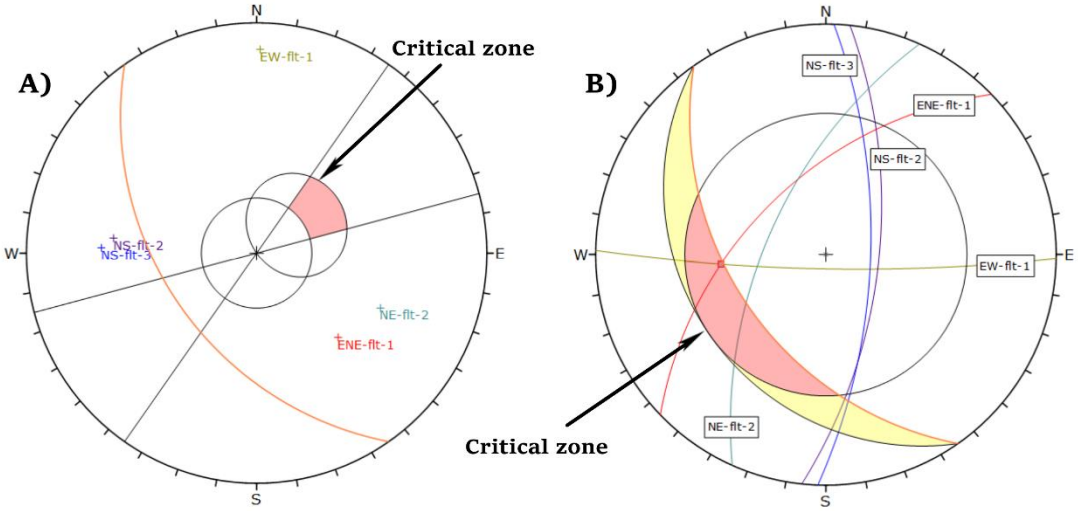

Figure 103. Kinematic analyses of the north east wall. (A) Planar sliding. (B) Wedge sliding.

Analyses results exhibit one critical condition from the structures, which corresponds to the intersection between ENE-flt-1 and EW-flt-1 for wedge sliding. However, the wedge

formed between the structures is in the mined-out area (center of the pit) which means that the risk is low and/or null for the slope stability.

From further examination of the wedge sliding stereo net, it can be recognized that the intersection point between EW-flt-1 and NE-flt-2 is near the critical zone. This suggests the existence of a potential wedge structure, which was already recognized during section 5.4.2. The area of influence of the wedge block is indicated in Figure 86, which extends for +500m in height entailing three inter-ramp slopes. This means that the potential risk of the structure extends to the overall slope scale, and that it should be investigated further to mitigate hazards arising from slope failure.

5.5.3 North West Sector

The structures considered for the analysis of the north west wall are presented in table 39.

Table 39. Major structures interacting with the north west wall.

STRUCTURE	DIP	DIP DIRECTION
EW-flt-1	85	182
NE-flt-rv1	37	292
NS-flt-1	75	96
NS-flt-5	72	86
ENE-flt-1	63	320

The evaluation of planar and wedge failure modes (~48° OSA) is presented in Figure 104.

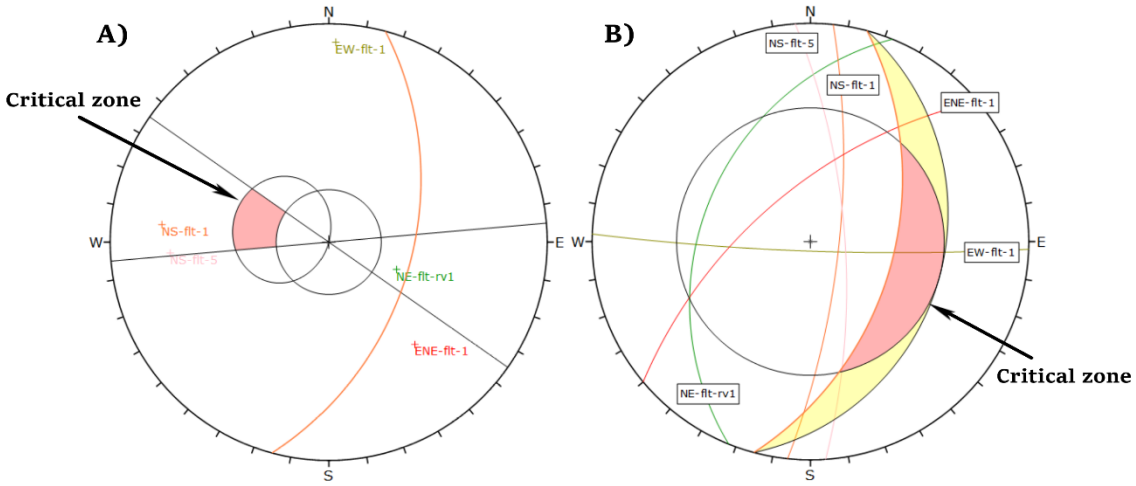

Figure 104. Kinematic analyses of the North West Wall. (A) Planar sliding. (B) Wedge sliding.

Kinematic analyses results do not indicate explicitly any critical condition and/or instability from the structures. However, structures NS-flt-1 and NS-flt-5 are daylighting the slope, indicating that they are susceptible to triggering planar failures under varying stress conditions. The risks associated to these structures were already recognized in

section 5.4.3 for the upper and middle inter-ramp slopes of the north west sector. If a planar failure occurred along any of the two structures, the consequences would reach the overall-slope scale as multiple ramps, haulage roads, and inter-ramp slopes would be lost. The area of influence of the structures is presented in Figure 105.

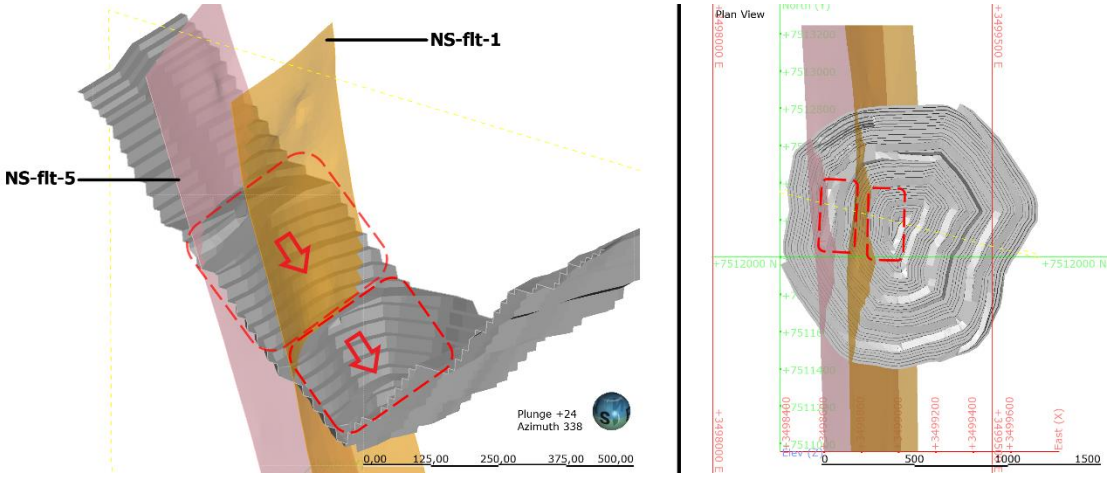

Figure 105. Slice of 3D view of Stage 5 pit. Potential planar failure from NS-flt-1 and NS-flt-5 in the north west wall.

5.5.4 South Sector

The structures considered for the analysis of the south wall are presented in table 40.

Table 40. Major structures interacting with the south wall.

STRUCTURE	DIP	DIP DIRECTION
NE-flt-2	58	301
NE-flt-rv1	39	291
NS-flt-1	75	89
NS-flt-2	73	76
NS-flt-3	69	78
Splay-flt-010	79	76

The evaluation of planar and wedge failure modes (~45° OSA) is presented in Figure 106.

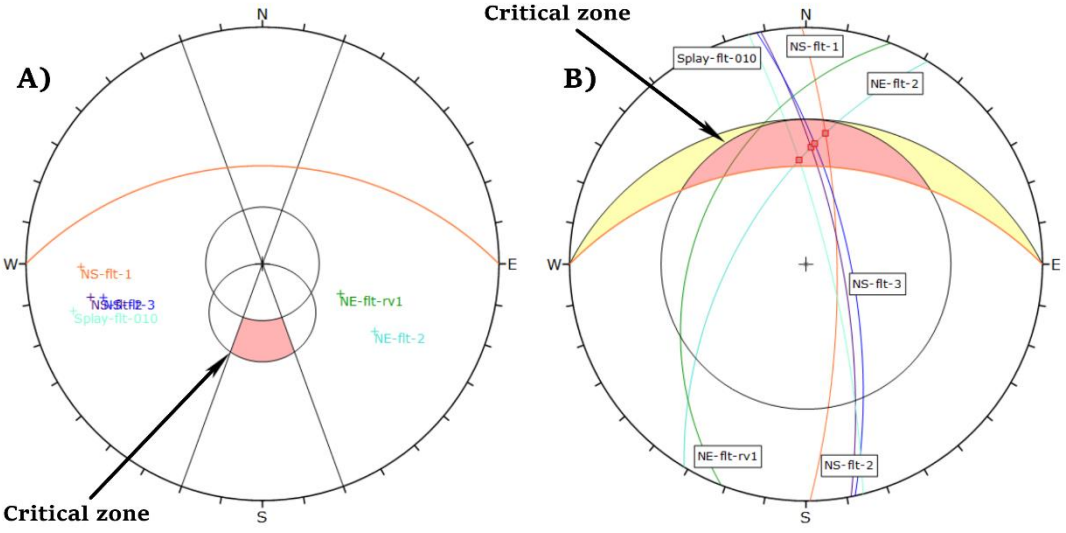

Figure 106. Kinematic analyses of the South Wall. (A) Planar sliding. (B) Wedge sliding.

Analyses indicate that the main threat to the stability of the south wall is the wedge-type structures generated by the intersection of fault NE-flt-2 with structures from the vein system (NS-flt-2- NS-flt-3, and Splay-flt-010). This risk was already highlighted in section 5.4.4, where potential instabilities could impact the upper and middle inter-ramp slopes and haulage roads (Figure 94) i.e., the consequences reach the overall slope scale.

5.5.5 South East Sector

The structures considered for the analysis of the south east wall are presented in table 41.

Table 41. Major structures interacting with the south east wall.

STRUCTURE	DIP	DIP DIRECTION
NE-flt-2	45-53	294
NS-flt-2	74	77
NS-flt-3	66	87

The evaluation of planar and wedge failure modes (~45° OSA) is presented in Figure 107.

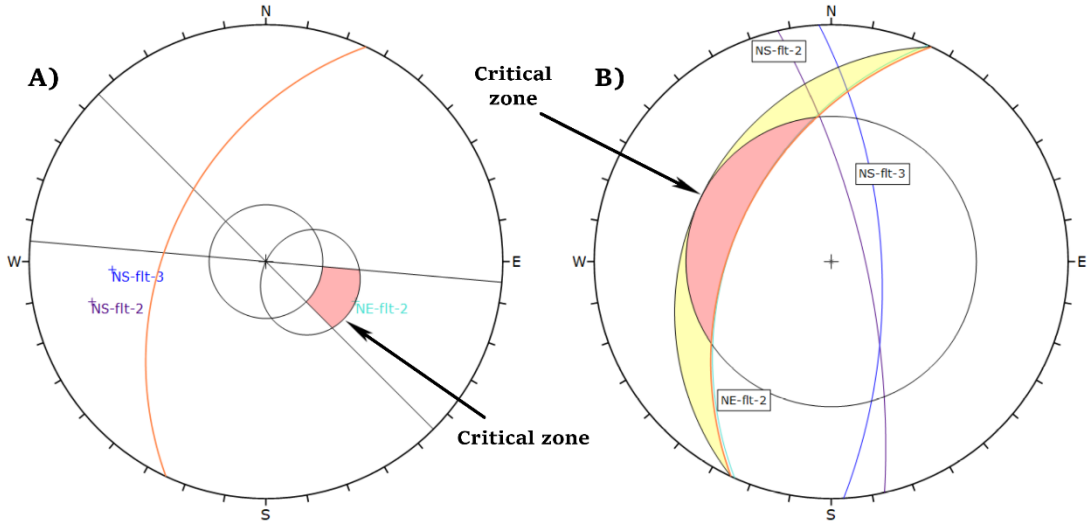

Figure 107. Kinematic analyses of the South East Wall. (A) Planar sliding. (B) Wedge sliding.

The south east wall of the Stage 5 pit represents an area of major risk as fault NE-flt-2 has a high potential for developing a planar failure (as indicated by the planar sliding analysis in Figure 107). NE-flt-2 is a regional fault interpreted with high confidence, which strikes sub-parallel to the south east wall and dips at approximately 45-53°. As discussed in section 5.4.5, the fault intersects the middle inter-ramp of the slope. This means that if failure occurred along the plane of NE-flt-2, all geotechnical structures below the +90mRL level would be lost (Figure 108), representing a threat for the mine in terms of safety and economics. Therefore, complementary geological and geotechnical investigations should be conducted to understand the behaviour of the structure, and to determined if modifications to the pit design are necessary.

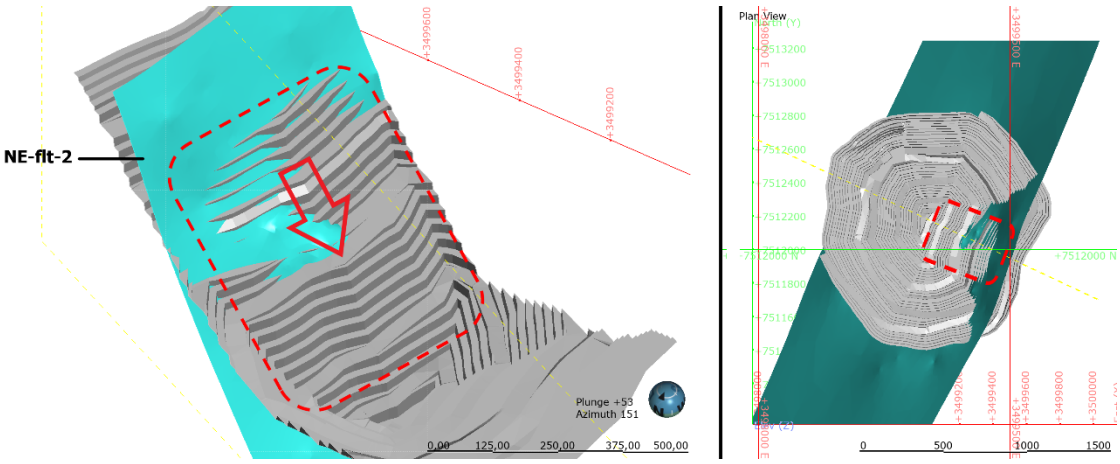

Figure 108. Potential planar failure from NE-flt-2 in the north east wall. Sliced 3D view of Stage 5 pit.

5.5.6 South West Sector

The structures considered for the analysis of the southwest wall are presented in table 42.

Table 42. Major structures interacting with the south west wall.

STRUCTURE	DIP	DIP DIRECTION
NE-flt-rv1	37	291
NS-flt-1	74	89
ENE-flt-1	62	319
NS-flt-5	71	86

The evaluation of planar and wedge failure modes (~47° OSA) is presented in Figure 109.

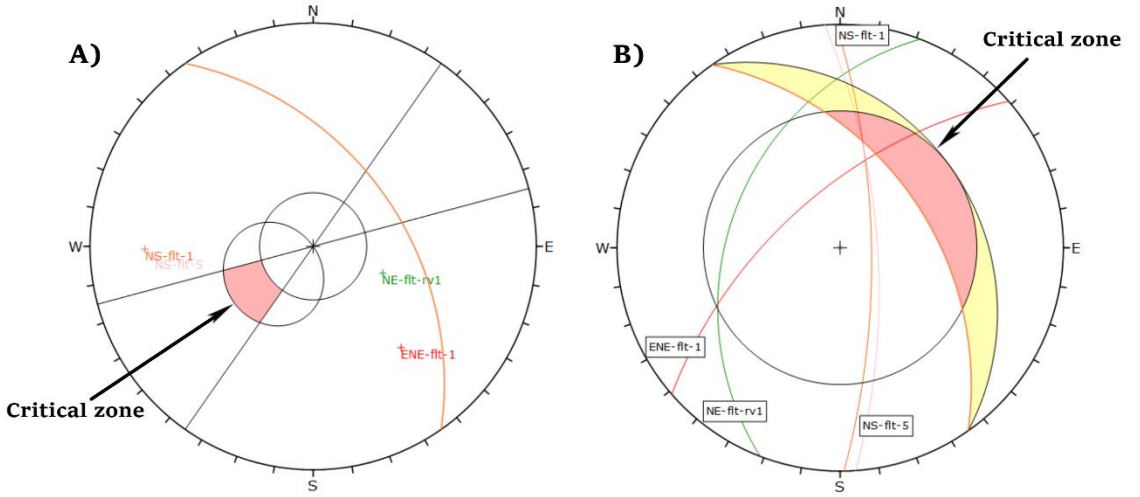

Figure 109. Kinematic analyses of the South East Wall. (A) Planar sliding. (B) Wedge sliding.

Planar and wedge sliding analyses don't indicate any critical conditions from the structures. Intersection of ENE-flt-1 with vein structures (NS-flt-1 and NS-flt-5) is near the wedge sliding critical zone, however, the wedge structures lay in the mined-out area (center of the pit) i.e., the risk is low/null for the slope.

6 DISCUSSION

6.1 Slope Instabilities Caused by Minor Discontinuities

The Kevitsa slope failure database has registered 185 rock falls since 2019. Approximately 50% of these incidents can be categorized as "minor" slope failures, as their volume is smaller than $10m^3$. In comparison, 9% of them are associated with larger volumes exceeding $300m^3$. Visualization of the rock falls exhibits that most of them are concentrated in the west-northwest and northeast sections of the pit (Figure 110).

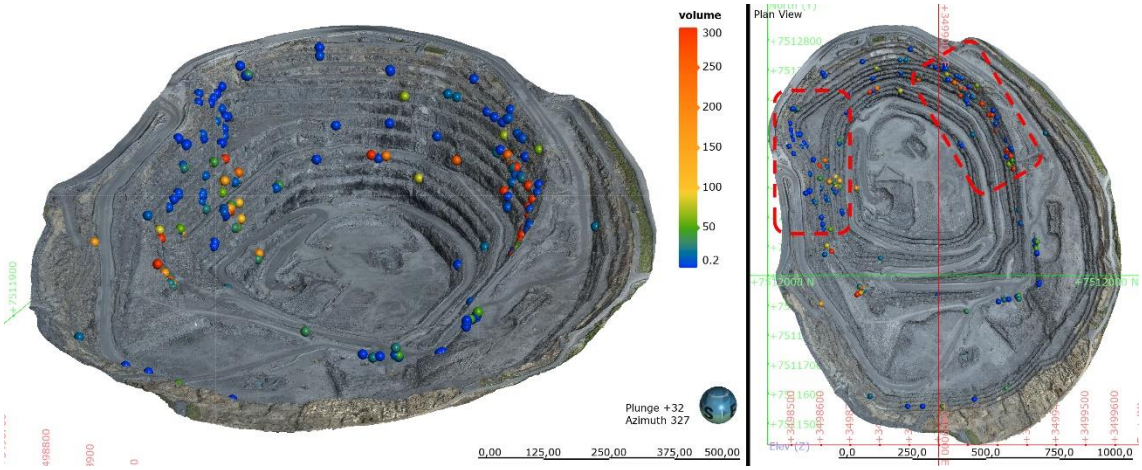

Figure 110. Location and volume of slope failures. in 3D view from the 2022 pit photogrammetry.

Although the rock falls significantly vary in volume, majority of them can be described as bench-scale wedge and planar failures. These typically occur shortly after blasting and can be rooted to distinctive joint sets of the deposit. According to the density and geometrical properties of the rock joints (i.e., orientation, persistence, spacing) their impact to the pit stability varies.

The most dominant structures at the mine site can described as north-east trending fractures that dip steeply towards the south-east. These were grouped during the study into joint sets E (~65/135), F (~85/140), and C (~83/108), by the analysis of linear, planar, and laser scan data. The structures have been recognized in previous studies (Pabst, 2023; WSP, 2014), and are interpreted to be the result of a transpressive stress field with a NE-SW shear component (Lindqvist, 2017). In terms of stability, the orientation of the structures is unfavorable for slopes trending north, north-east. This aligns with the bench-scale kinematic analysis results, as benches from the northwest sector of the Stage 5 pit present the highest risk for planar sliding and wedge sliding (18,05% and 54,12%

respectively, from planar data analyses) from all sectors. Additionally, this area of the current pit registers a large amount of slope failures (indicated in Figure 110).

Structures from Sets E, F, and C were also recognized to comprise multiple critical intersections for wedge sliding across other sectors of the pit. Such intersections were determined from the bench-scale kinematic analyses (Figures 66, 69, 72 and 81), and can be corroborated with the slope failures observed in the pit photogrammetry (Figure 111)

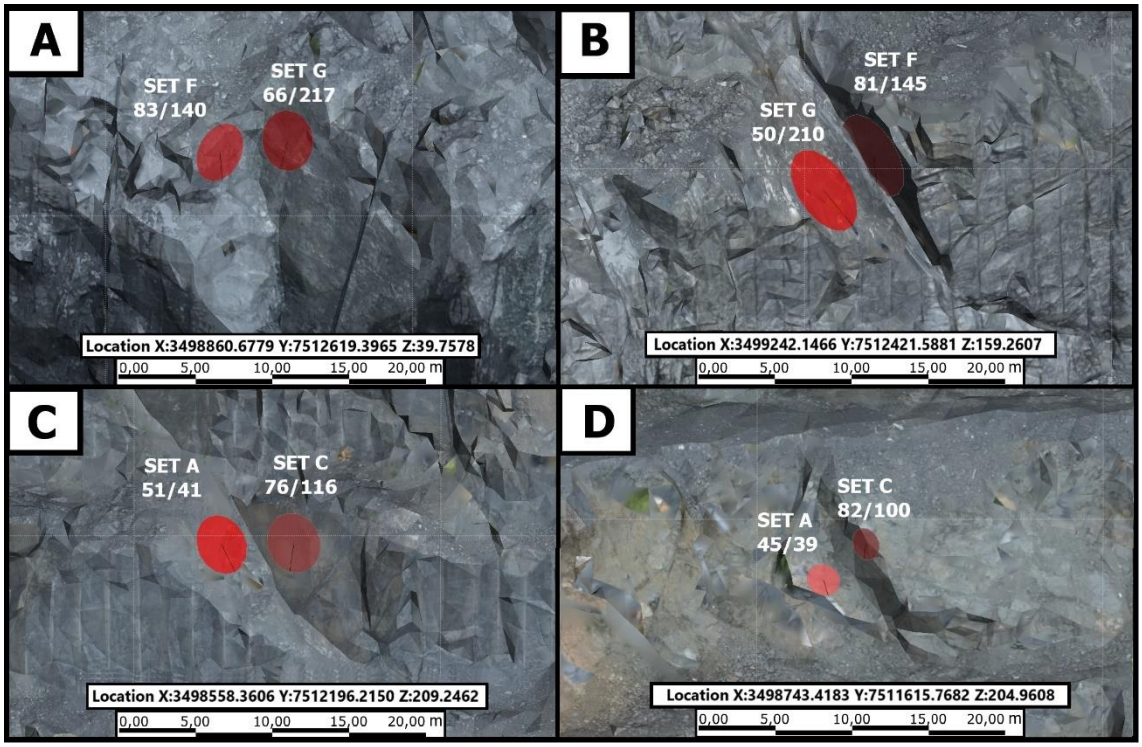

Figure 111. Wedge failures from pit photogrammetry involving north-east trending fractures. (A) North section; (B) North East section; (C) North West section; (D) South West section of the pit.

The slopes of the north-west section of the Stage 5 pit face an additional stability risk which is attributed to structures from Set D (~60/95). These fractures have an unfavorable orientation for slopes trending north-northeast, increasing the likelihood of planar and wedge failures. While the density of the structures is not as high as that of Sets E, F and C, the fractures from Set D exhibit an average persistence of over 40m (as shown in Figure 56) making them prone to trigger multi-bench slope failures.

Collectively, fractures from joint sets C, D, E, and F represent a structural risk for the north west section of both the current pit and planned Stage 5 pit. They create an area of potential slope instability where bench or multi-bench slope failures can occur along the discontinuity surfaces or pair of intersecting discontinuities. This is indicated by the rock falls observed in the pit photogrammetry (Figure 112) and the kinematic analyses.

Figure 112. Slope failures in the North West section of the pit from 3D photogrammetry.

The north-east section of the pit represents another area susceptible to slope instability, with multiple slope failures reported, including the ocurrence with the largest volume registered at $7628m^3$. Such rock falls can be attributed to north west trending fractures that dip moderately to steeply towards the south west. These were grouped during the study into joint sets G (~50/210) and H (~69/201). The structures comprise most of the critical intersections for wedge sliding of the north east sector analyses (Figure 69), which means that the elevated risk for wedge failure (25,46% and 23,98% from linear and planar data analyses, respectively) can be largely attributed to them. Such critical intersections can be observed in the pit photogrammetry (Figure 113).

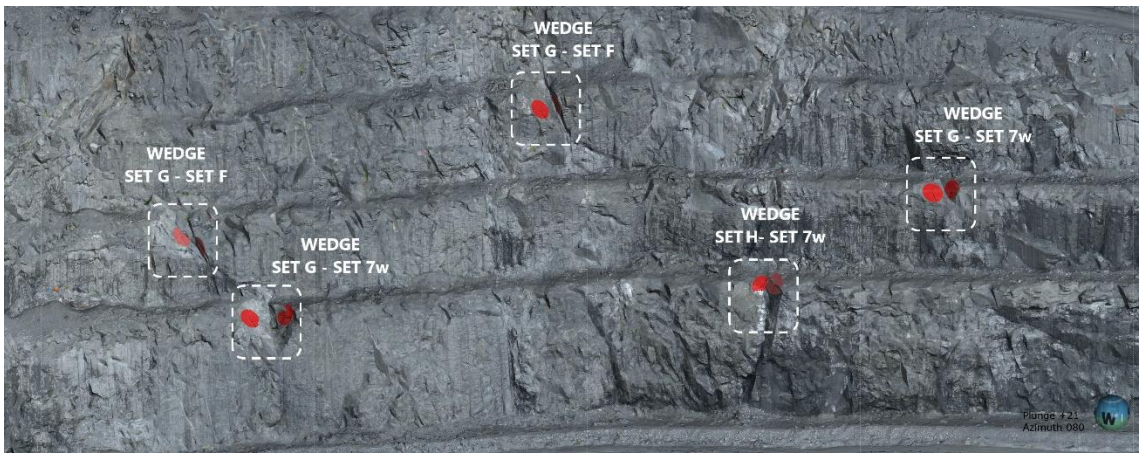

Figure 113. Wedge failures in North East section of the pit. From 3D photogrammetry.

In addition to their bench-scale impact, structures from Set G represent a risk for the inter-ramp slopes due to their multi-bench condition (indicated in Figure 60). Wedge failures associated to the structures seem to occur simultaneously over multiple benches and can be found parallel to previous rock falls. Figure 114 shows the most recent slope failure involving fractures from Set G ($4619m^3$), in which sliding occurs over the intersection plane of Sest G F extending for almost 3 benches (~90m vertically).

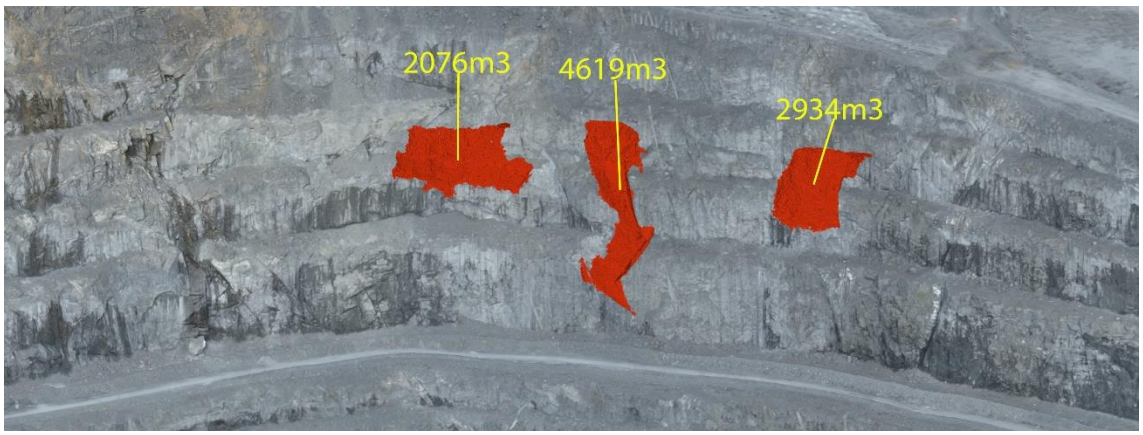

Figure 114. Slopes failures in North East section of the pit. From 3D photogrammetry.

Conclusively, it can be deducted that the areas with most influence of minor discontinuities are the north-west and north-east sectors of both the current pit and the proposed Stage 5 pit (Figure 115). This due to the density, orientation, and persistence of fractures from joint sets C, D, E, F, G, and H, which are the most dominant structures.

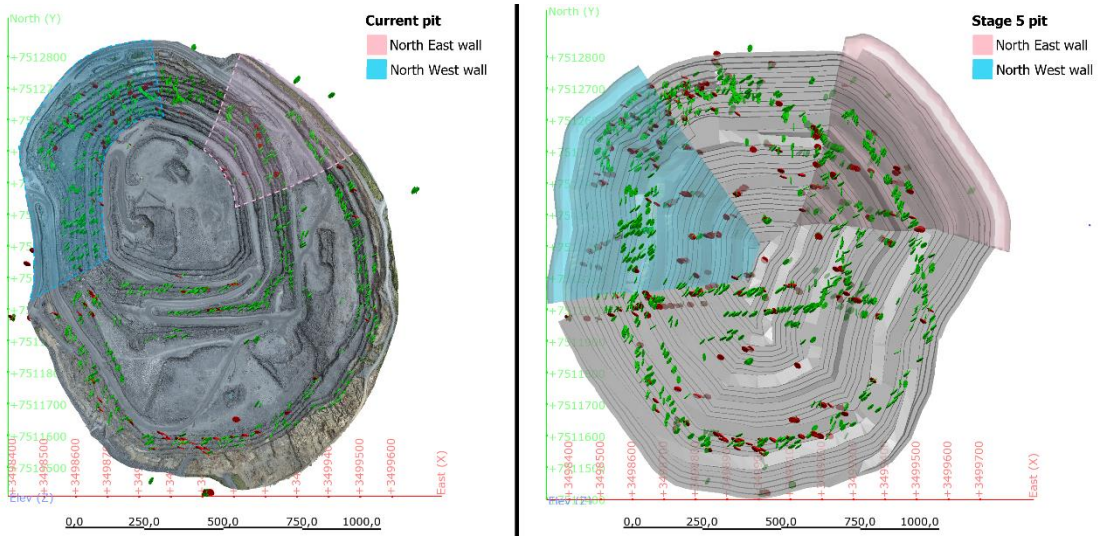

Figure 115. Sectors of major influence of minor discontinuities in current pit (left) and Stage 5 pit (right). Southeast and southwest dipping fractures (green and red respectively).

Nevertheless, it should be highlighted that the impact of the structures is not limited to these sectors, and most likely extends to the north wall (which reports significant slope failures) due fracture's orientation variability.

Additionally, the stability of other sectors could be largely influenced by minor discontinuities. Such as the south-west wall of the Stage 5 pit, which presents a significant risk for planar and wedge sliding at bench scale (10,12% and 44,74% respectively, from planar data analysis) attributed primarily to structures from Set A (which have a multi-bench condition). However, due to the small rock exposure and slope failures reported in the area, it cannot be corroborated currently.

6.2 Slope Instabilities Caused by Major Discontinuities

Slope failures caused by major structures are not as frequent at Kevitsa. The most recent occurrence was interpreted by Pabst (2023) to be attributed to the interaction between NE-flt-rv1 and NS-flt-1, which led to a wedge failure in the southwestern section of the pit (Figure 116). Nevertheless, kinematic analyses of major structures revealed several potential instabilities for the inter-ramp and overall slopes of the Stage 5 pit.

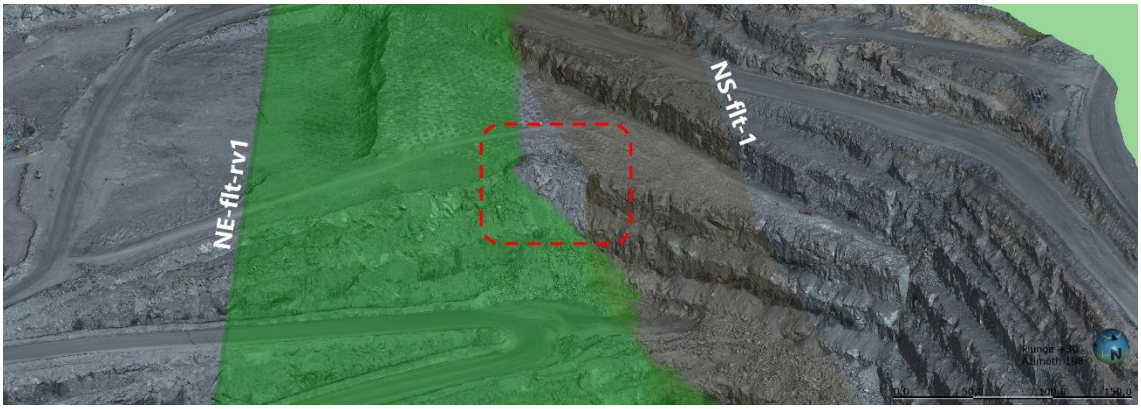

Figure 116. Wedge failure in the southwest section of the pit. From 3D photogrammetry.

Potential planar failures of large volume were recognized from EW-flt-1, NS-flt-1, NS-flt-5, and NE-flt-2. The risk associated to structures EW-flt-1, NS-flt-1 and NS-flt-5 can be classified as medium because the structures daylight the overall slopes but dip steeper than them. This means that the orientation of the structures is not entirely critical, however, they still represent a zone of weakness where failure could be triggered by varying stress conditions (e.g., groundwater, drill and blast disturbance). In comparison, the planar failure associated to NE-flt-2 presents the largest volume and is of high risk as the structure complies with all critical conditions for planar sliding. Figure 117 shows the potential planar failures that could be raised by major structures in the Stage 5 pit.

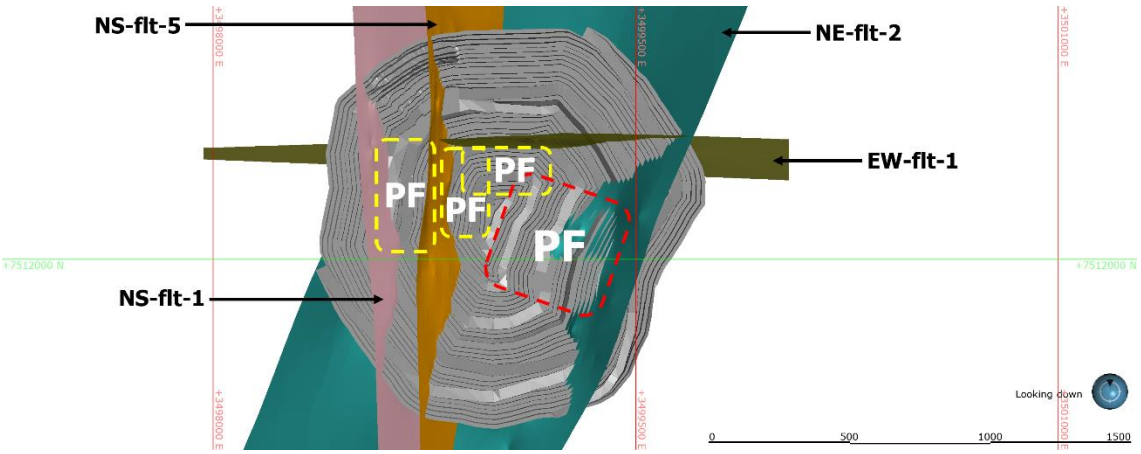

Figure 117. Potential planar failures (PF) of Stage 5 pit. Areas of medium risk (yellow) and areas of high risk (red).

Potential wedge failures were also recognized in the Stage 5 pit. From these, the most significant in volume is produced by the intersection of structures NE-flt-2 and EW-flt-1, which are two faults interpreted with high confidence (Pabst, 2023). The intersection of the two structures occurs at the upper inter-ramp slope of the northeast wall, stablishing a wedge structure that extends for over 500m in height. This means that it represents a threat to the overall slope stability, with potential repercussions for the entire pit.

Wedge structures of lower volume were identified from the intersections between NE-flt-2 with NS-flt-2, NS-flt-3, and Splay-flt-010. Individually, these wedge blocks pose a low risk due to their low volume and their intersection point which is located slightly behind the pit boundary. However, due to parallelism of the discontinuities, if failure from one wedge block occurred it could potentially trigger failure of the adjacent blocks. This could endanger all geotechnical structures found within the +248mRL to 113mRL level of the south wall. Figure 118 presents the potential wedge failures of the Stage 5 pit.

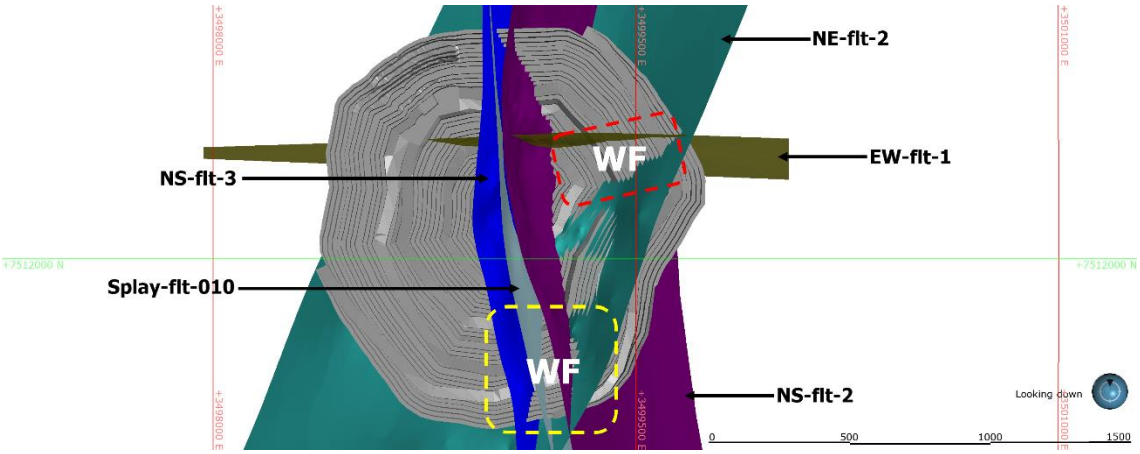

Figure 118. Potential wedge failures (WF) of Stage 5 pit. Areas of medium risk (yellow) and areas of high risk (red).

Overall, it can be deducted that the most critical structure for the development of the Stage 5 pit is structure NE-flt-2, due to its susceptibility to generate both planar and wedge failures of large scale. This suggests the need for further geological investigation to improve the understanding of the structure orientation and extension. Additionally, detailed geotechnical assessments that incorporate the rock mass properties should be conducted to define the structure's impact on the Stage 5 pit design.

It should also be highlighted that structures EW-flt-1, NS-flt-1 and NS-flt-5 are intersecting sub-perpendicularly different haulage roads of the Stage 5 pit. This indicates areas of the pit design that should be reviewed as well.

7 CONCLUSSIONS AND RECOMMENDATIONS

The research conducted in this thesis reviewed the impact of the geological discontinuities within the Kevitsa area into the proposed excavation slopes of the Stage 5 pit design. Dominant joint orientations were characterized, and their impact on slope stability was assessed by kinematic analysis of rock blocks carried out using stereographic projection techniques.

Joint set analyses improved the understanding of the structural conditions of the minor discontinuities, which should be considered when defining the existence and extension of major structures in the Kevitsa structural model. The analyses determined NE and NW trending as the dominant fracture orientations, which align with regional and local topographic lineaments (Lindqvist, 2017). The steeply NE trending fractures pose a structural risk for north, north-east trending bench slopes, where the threat extends to the inter-ramp scale due to the persistence of joint sets D, E, and F. The moderately to steeply NW trending fractures pose a structural risk for north, north-west trending bench slopes, and are accountable for the slope failures of largest volume reported at Kevitsa. These can be described as wedge failures resulting from the interaction of joint sets G and E/F, all of which present a multi-bench condition. The risks recognized from the structures suggest a need for geotechnical berms in the Stage 5 pit in the sectors highlighted in Figure 115. In addition, further examination of joint set A should be conducted as rock exposure increases at the southern part of the pit. This will be useful to understand its influence on slope stability, which is greater in the south west sector.

Analyses of major structures suggested that characterization of fault NE-flt-2 is critical for the development of the Stage 5 pushback. Diamond-drilling campaigns should aim to define the extension and shape of the structure, especially in the -165mRL level below the proposed south-east wall as the modelled surface mesh has a very irregular shape in this area. Geotechnical modelling using limit equilibrium (LEM) or finite element (FEM) methods should be conducted to provide a factor of safety to the structures flagged in section 6.2. This could define if modifications to the Stage 5 pit are necessary, which could entail: (1) doing a pushback of the south east wall to keep it behind NE-flt-2 (to avoid planar failure); and (2) straitening the benches of the south wall to maintain a 0° azimuth (to avoid formation of wedge blocks).

REFERENCES

Aladejare, A. E., & Akeju, V. O. (2020). Design and sensitivity analysis of rock slope using Monte Carlo simulation. Geotechnical and Geological Engineering, 38, 573-585.

Aladejare, A. E., & Wang, Y. (2018). Influence of rock property correlation on reliability analysis of rock slope stability: from property characterization to reliability analysis. Geoscience Frontiers, 9(6), 1639-1648.

Altiti, A. H., Alrawashdeh, R. O., & Alnawafleh, H. M. (2021). Open pit mining. Mining Techniques—Past, Present and Future.

Anderson, E. M. (1905). The dynamics of faulting. Transactions of the Edinburgh Geological Society, 8(3), 387-402.

Arteaga, F., Nehring, M., Knights, P., & Camus, J. (2014). Schemes of exploitation in open pit mining. In Mine Planning and Equipment Selection: Proceedings of the 22nd MPES Conference, Dresden, Germany, 14th–19th October 2013 (pp. 1307-1323). Springer International Publishing.

Berthet, L. (2021). Boliden Summary Report. Resources and Reserves 2021, Kevitsa.

Bishop, R. (2020). Applications of close-range terrestrial 3D photogrammetry to improve safety in underground stone mines (Doctoral dissertation, Virginia Tech).

Booth, M. (2015) Comments on The Kevitsa property, Lapland, Finland. 2015. A report prepared for First Quantum Minerals Ltd.

Brownscombe, W., Ihlenfeld, C., Coppard, J., Hartshorne, C., Klatt, S., Siikaluoma, J. K., & Herrington, R. J. (2015). The Sakatti Cu-Ni-PGE sulfide deposit in northern Finland. In Mineral deposits of Finland (pp. 211-252). Elsevier.

Cloos, E. (2014) Fractures. Available at: https://web.archive.org/web/20140713211137/http://rockfracture.com/html2/GeologicalStructure.html [Accessed: February 23, 2023].

DesRoches, A., Danielescu, S., & Butler, K. (2014). Structural controls on groundwater flow in a fractured bedrock aquifer underlying an agricultural region of northwestern New Brunswick, Canada. Hydrogeology Journal, 22(5), 1067.

Dos Santos, T. B., Lana, M. S., Pereira, T. M., & Canbulat, I. (2019). Quantitative hazard assessment system (Has-Q) for open pit mine slopes. International Journal of Mining Science and Technology, 29(3), 419-427.

Du, S. G., Saroglou, C., Chen, Y., Lin, H., & Yong, R. (2022). A new approach for evaluation of slope stability in large open-pit mines: a case study at the Dexing Copper Mine, China. Environmental Earth Sciences, 81(3), 102.

Eilu, P., Pankka, H., Keinänen, V., Kortelainen, V., Niiranen, T., & Pulkkinen, E. (2007). Characteristics of gold mineralisation in the greenstone belts of northern Finland. Geological Survey of Finland, Special Paper, 44, 57-106.

Fleurisson, J. A. (2012). Slope design and implementation in open pit mines: geological and geomechanical approach. Procedia Engineering, 46, 27-38.

Goodman, R., and Bray, J. 1976. Toppling of rock slopes. Proceedings, Specialty Conference on Rock Engineering for Foundations and Slopes, American Society of Civil Engineers. Boulder, CO, vol. 2, pp. 201-234.

Goodman, R.E. (1980). Introduction to Rock Mechanics (Chapter 8), Toronto: John Wiley, pp 254-287.

Gray, D., Cameron, T., & Briggs, A. (2016): Kevitsa Nickel Copper Mine, Lapland, Finland NI 43-101 Technical Report 30th March.

Gu, X., Wang, Q., Xu, X., & Ma, X. (2021). Phase planning for open pit coal mines through nested pit generation and dynamic programming. Mathematical Problems in Engineering, 2021, 1-8.

Hanski, E. & Huhma, H. (2005). Central Lapland greenstone belt. In: Lehtinen, M. Nurmi, P.A. & Rämö, O.T. (eds.) Precambrian geology of Finland – Key to the evolution of the Fennoscandian Shield. Elsevier, Amsterdam, pp. 139-194.

Helsinki University of Technology. (2006). Test report TKK-Kal 21/2006.

Hoek, E., Read, J., Karzulovic, A., & Chen, Z. Y. (2000). Rock slopes in civil and mining engineering. In ISRM International Symposium. International Society for Rock Mechanics and Rock Engineering.

Hölttä, P., Väisänen, M., Väänänen, J., & Manninen, T. (2007). Paleoproterozoic metamorphism and deformation in Central Lapland, Finland. Gold in the Central Lapland Greenstone Belt. Geological Survey of Finland, Special Paper, 44, 7-56.

Hudson, J.A. and Harrison, J.P. 1997. Engineering Rock Mechanics – An Introduction to the Principles, Pergamon Press.

Hungr, O., Leroueil, S., & Picarelli, L. (2014). The Varnes classification of landslide types, an update. Landslides, 11, 167-194.

Jigsaw, (2009) Structural investigations at the Kevitsa Ni-Cu-PGE mine and surrounding areas, Finland. Unpublished confidential report for First Quantium Minerals Ltd.

Kolapo, P., Oniyide, G. O., Said, K. O., Lawal, A. I., Onifade, M., & Munemo, P. (2022). An Overview of Slope Failure in Mining Operations. Mining, 2(2), 350-384.

Kotavaara, O., Domenech, G., Mingot, S., Joutsenvaara, J., Puputti, J., Yll, D. N., & Ala-Hulkko, T. (2023). Interferometric Synthetic Aperture Radar (InSAR)-based measurements of displacements due to geomorphologic changes in northern mining environments–testing and validating InSAR in open pit and tailings of Pyhäsalmi Mine, Finland (No. EGU23-6208). Copernicus Meetings.

Kuchling, K. (2015) Pit wall angles and bench width – how do they relate?, OVERVIEW. Available at: https://kuchling.com/13-pit-wall-angles-and-bench-width-how-do-they-relate/ [Accessed: December 15, 2022].

Lana, M. S. (2014). Numerical modeling of failure mechanisms in phyllite mine slopes in Brazil. International Journal of Mining Science and Technology, 24(6), 777–782.

Lappalainen, M. and White, G. (2010). NI 43-101 Technical Report on Mineral Resources of the Kevitsa Deposit Project, Finland.

Lindqvist, T., Skyttä, P., Koivisto, E., Häkkinen, T., & Somervuori, P. (2017). Delineating the network of brittle structures with geotechnical, structural and reflection seismic data, Kevitsa open pit, northern Finland. GeoResJ, 13, 159-174.

Lisle, R. J., & Leyshon, P. R. (2004). Stereographic projection techniques for geologists and civil engineers. Cambridge University Press.

Luolavirta, K., K., Hanski, E., Mayer, W., O'Brien, H. and Santaguida, F. (2017): PhD Project: Magmatic evolution of the Kevitsa intrusion and its relation to the Ni-Cu-(PGE) mineralization, presentation, p. 26.

Malik, R. (2018) Classification of folds: Rocks: Geology, Geography Notes. Available at: https://www.geographynotes.com/rocks/folds/classification-of-folds-rocks-geology/5653 [Accessed: February 23, 2023].

Mandl, G. (2005). Rock joints. Springer-Verlag Berlin Heidelberg.

Marjoribanks (2021) Measuring structures in oriented core, Roger Marjoribanks. Available at: http://rogermarjoribanks.info/measuring-structures-oriented-core/ [Accessed: 20 May 2023].

McDonald, I. (2020). The distribution of talc within the Kevitsa Ni-Cu-PGE mine, Finland.

Mitma, C. A. O. (2020). Slope Stability Analysis of Open Pit Mines under Geomechanical Uncertainty (Doctoral dissertation, McGill University (Canada).

Mote, T., Morley, D., Keuscher, T., & Crampton, T. (2004). GIS-based kinematic slope stability analysis. In The ESRI user conference In: Proceedings 24th annual ESRI international user conference, August (pp. 9-13).

Nicholas, D. E., & Sims, D. B. (2001). Collecting and using geologic structure data for slope design. Slope Stability in Surface Mining. SME Littleton, Co, 11-26.

Niiranen, T., Lahti, I., Nykänen, V., & Karinen, T. (2014). Central Lapland Greenstone Belt 3D modeling project final report. Geological Survey of Finland, Report of Investigation, 209(5).

Obregon, C., & Mitri, H. (2019). Probabilistic approach for open pit bench slope stability analysis–A mine case study. International Journal of Mining Science and Technology, 29(4), 629-640.

Osasan, K. S., & Afeni, T. B. (2010). Review of surface mine slope monitoring techniques. Journal of Mining Science, 46, 177-186.

Pabst et. al. (2023) Boliden Report: Kevitsa Structural Interpretation 2023. Internal Boliden Report.

Pabst, S. (2021). 2020/2021 Structural Model for the Kevitsa Cu-Ni-PGE sulphide deposit, Central Lapland Greenstone Belt, Finland; Boliden internal report.

Piteau, D. R., & Martin, D. C. (1982, June). Mechanics of rock slope failure. In 3rd International Conference of Stability in Surface Mining. Vancouver, Canada (pp. 113-169).

Priest, S. D., & Brown, E. T. (1983). Probabilistic stability analysis of variable rock slopes. Trans.-Inst. Min. Metall., Sect. A; (United Kingdom), 92.

Räsänen, J., Hanski, E., Juopperi, H., Kortelainen, V., Lanne, E., Lehtonen, M. I., ... & Väänänen, J. (1996, January). New stratigraphical map of central Finnish Lapland. In The 22nd Nordic Geological Winter Meeting (pp. 8-11).

Read, J., & Stacey, P. (2009). Guidelines for open pit slope design.

RIEGL (2020) News, RSS. Available at: http://www.riegl.com/media-events/single-news/article/surface-extraction-and-analysis-from-iriegli-laser-scan-data/ [Accessed: April 28, 2023].

Rocscience (2023) Density calculation, Dips Documentation | Density Calculation. Available at: https://www.rocscience.com/help/dips/documentation/viewing-and-display-options/contour-options/density-calculation [Accessed: February 24, 2023].

Skycatch (2021) What is photogrammetry, and how has it evolved in open pit mining?, Skycatch Blog. Available at: https://blog.skycatch.com/what-is-photogrammetry-and-how-is-it-used-in-open-pit-mining [Accessed: 22 May 2023].

SRK Finland. (2019) Technical Report for the Kevitsa Cu-Ni-PGE Mine, Finland: Boliden Kevitsa Mining Oy. Available at: https://www.boliden.com/globalassets/operations/exploration/mineral-resources-and-mineral-reserves-pdf/2019/resources_and_reserves_petiknas_norra_2019-12-31.pdf [Accessed: 20 May 2023].

SRK Finland. (2021). Kevitsa 3D Slope Stability Numerical Analysis. Unpublished report issued to Boliden Kevitsa Oy.

Stead, D., & Wolter, A. (2015). A critical review of rock slope failure mechanisms: the importance of structural geology. Journal of Structural Geology, 74, 1-23.

Sturzenegger, M., & Stead, D. (2009). Close-range terrestrial digital photogrammetry and terrestrial laser scanning for discontinuity characterization on rock cuts. Engineering Geology, 106(3-4), 163-182.

Terzaghi RD (1965). Sources of error in joint surveys. Geotechnique15, 287–304.

Thomas, R. D. H., Neilsen, J. M., Wilson, H. F., & Lamb, P. (2015). Structural interpretation from Televiewer surveys. In Proceedings of the Ninth Symposium on Field Measurements in Geomechanics (pp. 729-741). Australian Centre for Geomechanics.

Törmänen, T., Konnunaho, J. P., Hanski, E., Moilanen, M., & Heikura, P. (2016). The Paleoproterozoic komatiite-hosted PGE mineralization at Lomalampi, Central Lapland greenstone belt, northern Finland. Mineralium Deposita, 51(3), 411-430.

Twiss, R. J., & Moores, E. M. (2007). Structural geology (2nd ed., 736 p). New York: W. H. Freeman and Company.

Ureel, S., Momayez, M., & Oberling, Z. (2013). Rock core orientation for mapping discontinuities and slope stability analysis. International Journal of Research in Engineering and Technology, 2(7), 1-8.

Villaescuesa, E. (1991). A three-dimensional model of rock jointing. Thesis PhD. University of Queensland, Brisbane.

Weir, F. M. (2015). The future of structural data from boreholes. International Journal of Geotechnical Engineering, 9(3), 223-228.

WSP Finland Ltd. (2014) Kevitsa slope stability study, Phase I determination of geotechnical domains: geological structures and rock quality.

WSP Finland Ltd. (2015) Kevitsa Slope Stability study, Phase II Stability Analyses.

Wyllie, D. C., & Mah, C. (2004). Rock slope engineering. CRC Press.

Zhang, N., Li, C. C., Lu, A., Chen, X., Liu, D., & Zhu, E. (2018). Experimental studies on the basic friction angle of planar rock surfaces by tilt test. ASTM International.

APPENDICES

APPENDIX 1. Pole plot of Diamond-drill core logging dataset.

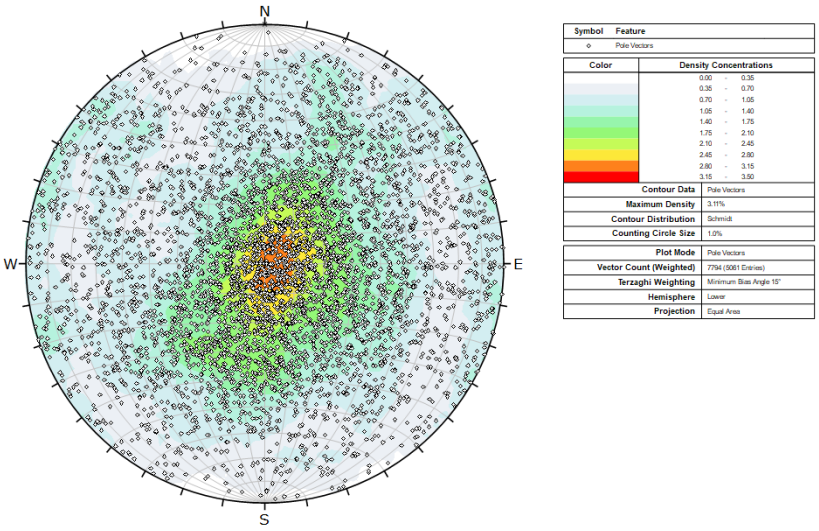

APPENDIX 2. Pole plot of photogrammetry mapping dataset.

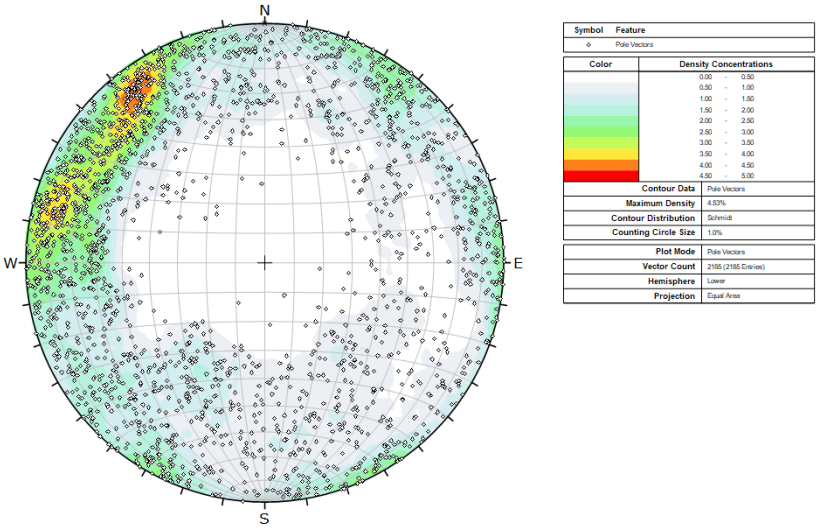

APPENDIX 3. Pole plot of Acoustic televiewer logging dataset.

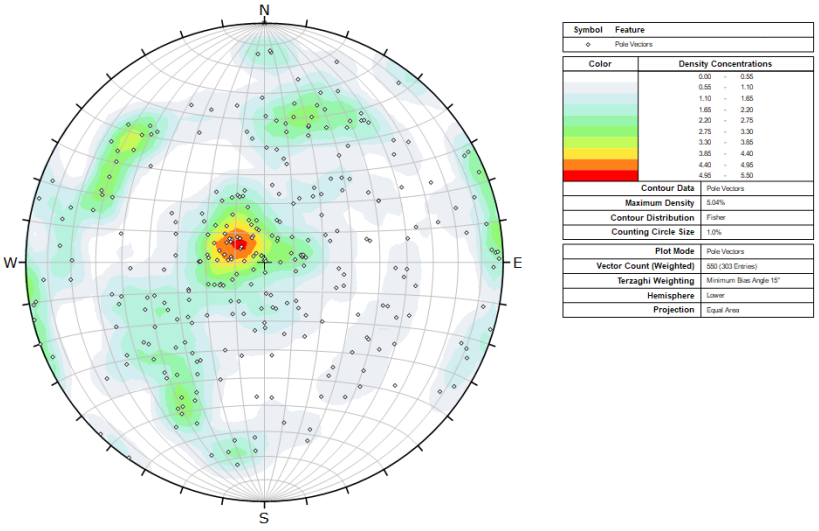

APPENDIX 4. Critical intersections for wedge sliding of the North sector. Stereo net of linear dataset.

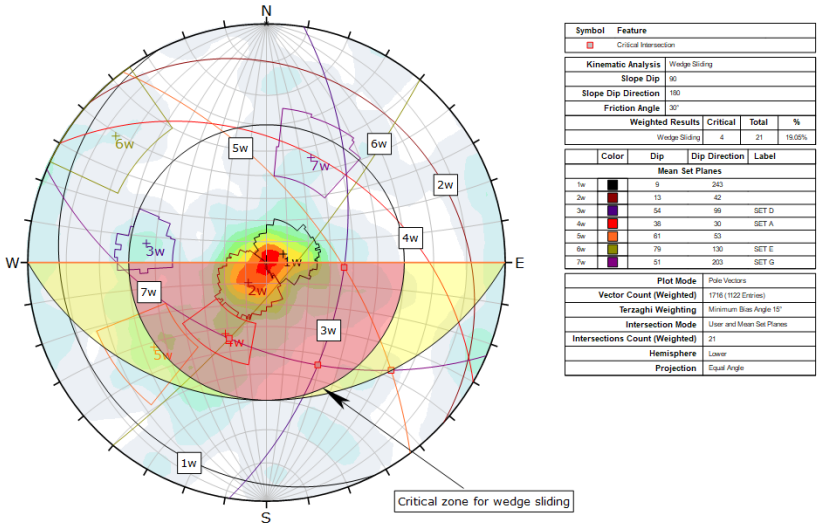

APPENDIX 5. Critical intersections for wedge sliding of the North sector. Stereo net of planar dataset.

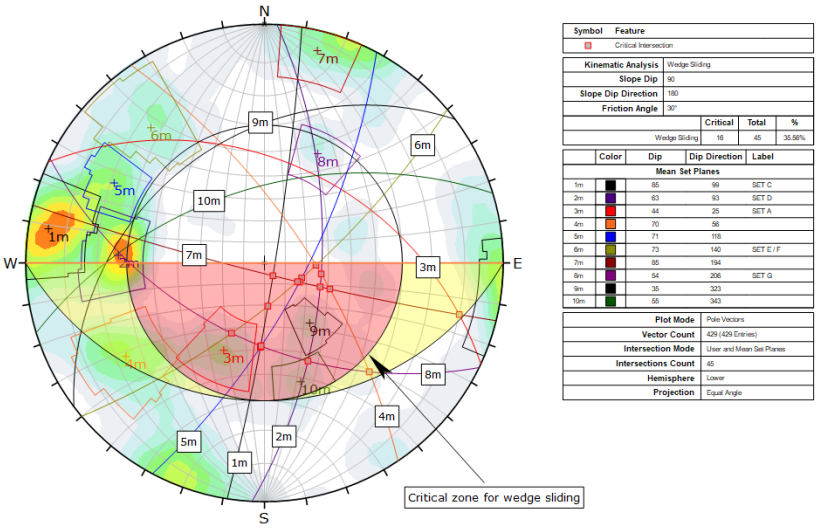

APPENDIX 6. Critical intersections for wedge sliding of the North East sector. Stereo net of linear dataset.

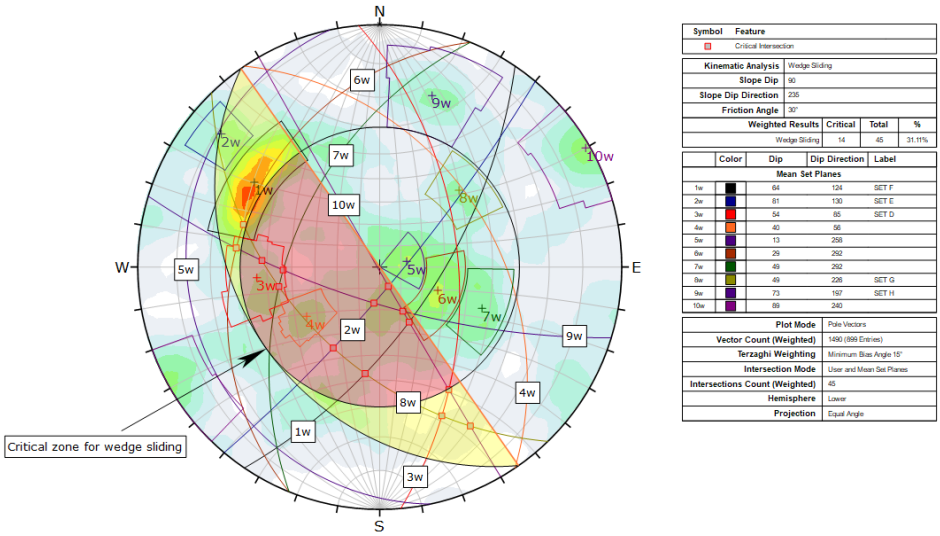

APPENDIX 7. Critical intersections for wedge sliding of the North East sector. Stereo net of planar dataset.

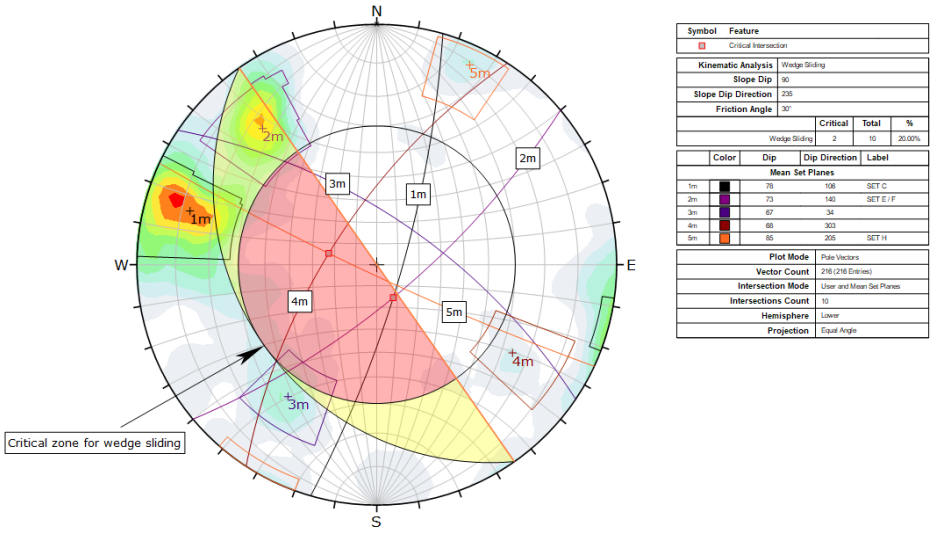

APPENDIX 8. Critical intersections for wedge sliding of the North West sector. Stereo net of linear dataset.

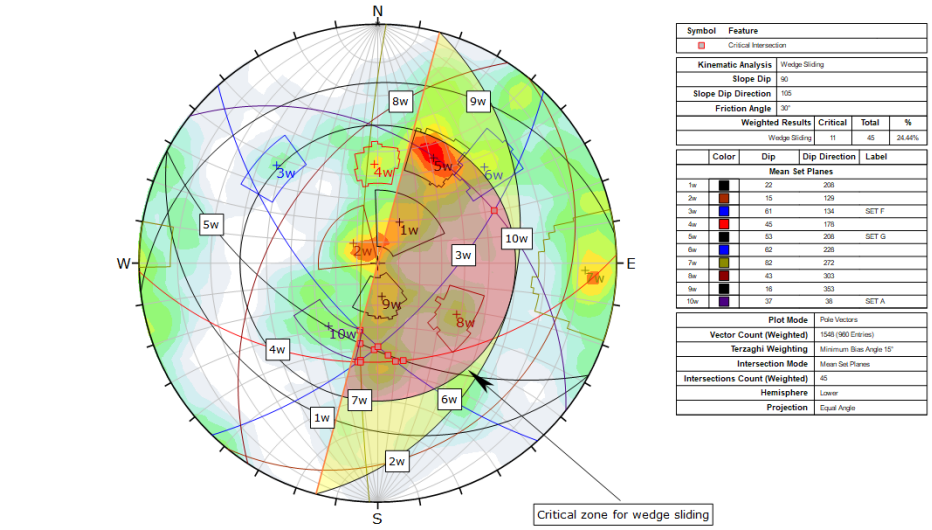

APPENDIX 9. Critical intersections for wedge sliding of the North West sector. Stereo net of planar dataset.

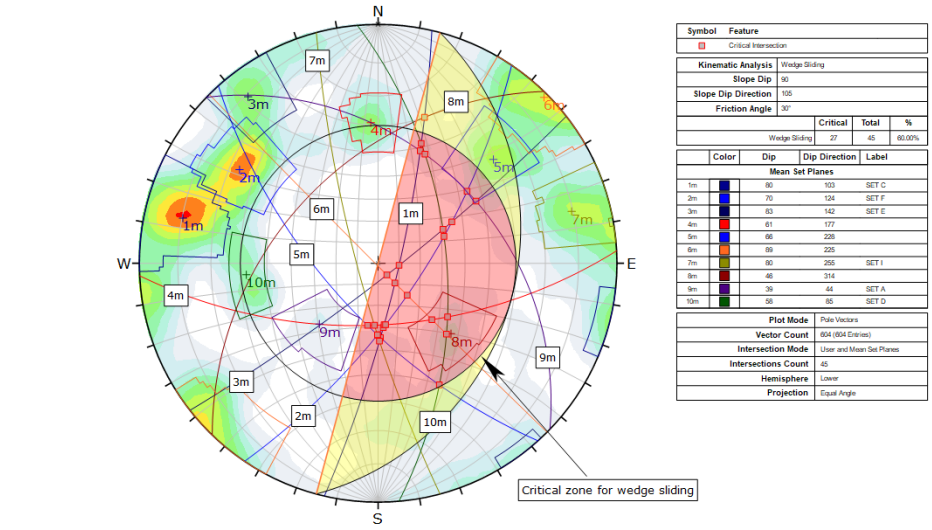

APPENDIX 10. Critical intersections for wedge sliding of the South sector. Stereo net of linear dataset.

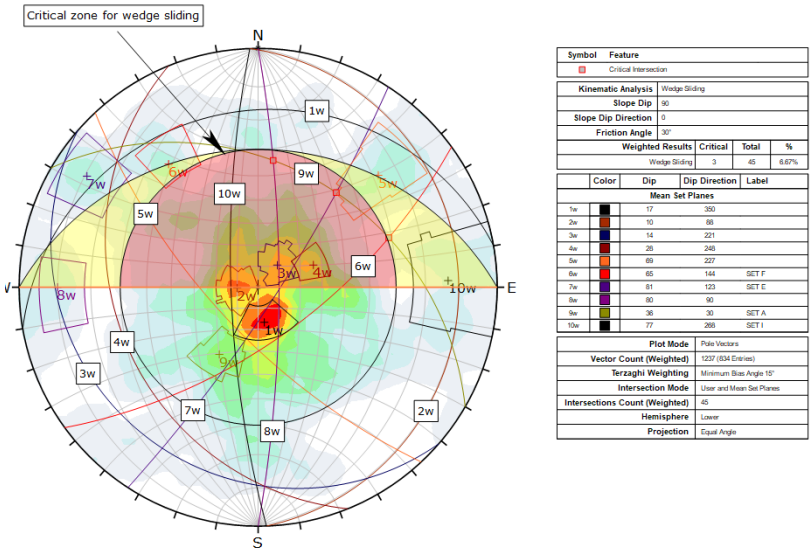

APPENDIX 11. Critical intersections for wedge sliding of the South sector. Stereo net of planar dataset.

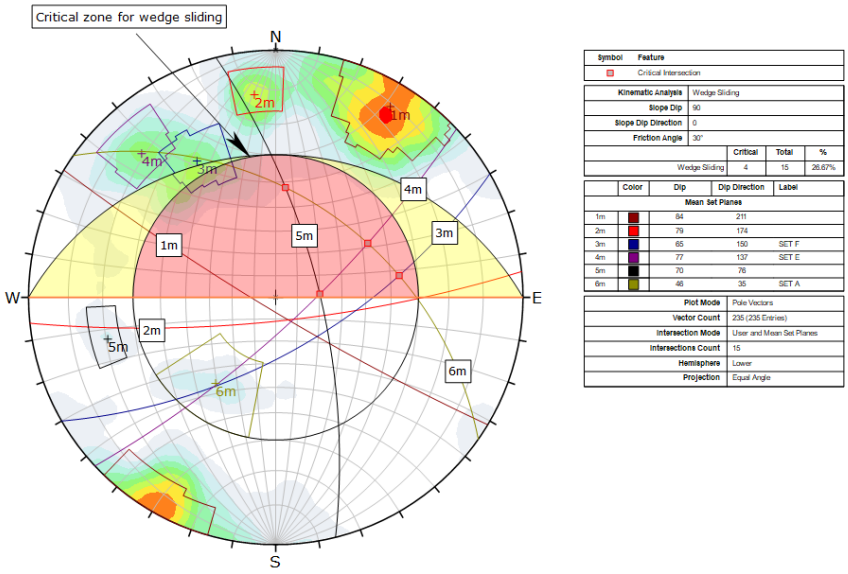

APPENDIX 12. Critical intersections for wedge sliding of the South East sector. Stereo net of linear dataset.

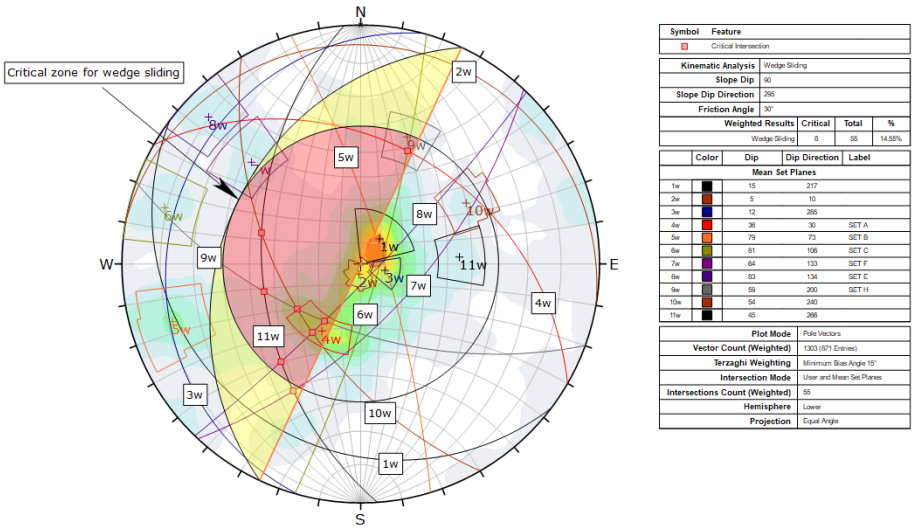

APPENDIX 13. Critical intersections for wedge sliding of the South East sector. Stereo net of planar dataset.

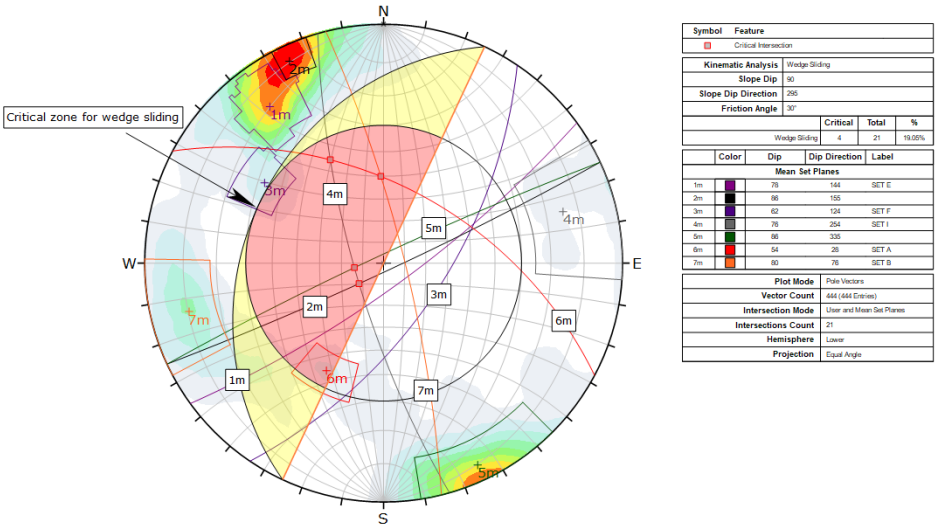

Symbol	Feature
	Critical Intersection

Kinematic Analysis	Wedge Sliding
Slope Dip	90
Slope Dip Direction	295
Friction Angle	30°

	Critical	Total	%
Wedge Sliding	4	21	19.05%

	Color	Dip	Dip Direction	Label
Mean Set Planes				
1m		78	144	SET E
2m		86	155	
3m		62	124	SET F
4m		78	254	SET I
5m		86	335	
6m		54	28	SET A
7m		80	78	SET B

Plot Mode	Pole Vectors
Vector Count	444 (444 Entries)
Intersection Mode	User and Mean Set Planes
Intersections Count	21
Hemisphere	Lower
Projection	Equal Angle

APPENDIX 14. Critical intersections for wedge sliding of the South West sector. Stereo net of linear dataset.

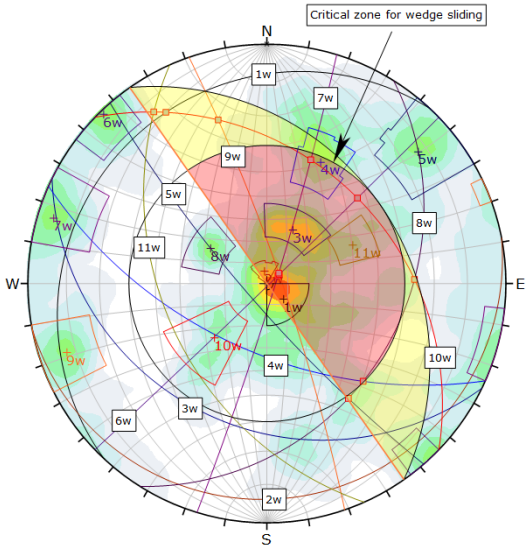

Symbol	Feature
	Critical Intersection

Kinematic Analysis	Wedge Sliding
Slope Dip	90
Slope Dip Direction	55
Friction Angle	30°

Weighted Results	Critical	Total	%
Wedge Sliding	11	55	20.00%

	Color	Dip	Dip Direction	Label
Mean Set Planes				
1w		11	313	
2w		6	169	
3w		28	206	
4w		58	204	SET G / H
5w		80	229	
6w		89	136	SET E
7w		86	107	SET C
8w		31	122	
9w		83	71	SET B
10w		35	44	SET A
11w		43	246	

Plot Mode	Pole Vectors
Vector Count (Weighted)	1051 (678 Entries)
Terzaghi Weighting	Minimum Bias Angle 15°
Intersection Mode	User and Mean Set Planes
Intersections Count (Weighted)	55
Hemisphere	Lower
Projection	Equal Angle

APPENDIX 15. Critical intersections for wedge sliding of the South West sector. Stereo net of planar dataset.

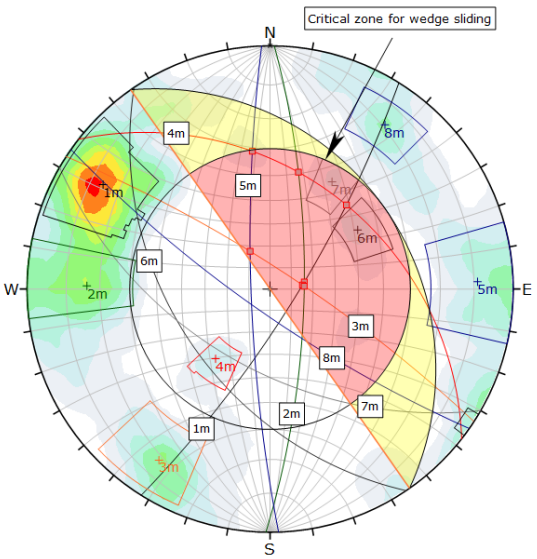

Symbol	Feature
	Critical Intersection

Kinematic Analysis	Wedge Sliding
Slope Dip	90
Slope Dip Direction	55
Friction Angle	30°

	Critical	Total	%
Wedge Sliding	7	28	25.00%

	Color	Dip	Dip Direction	Label
Mean Set Planes				
1m		78	122	SET E
2m		74	91	
3m		80	33	
4m		40	38	SET A
5m		81	268	SET I
6m		47	236	
7m		54	210	SET G
8m		79	215	

Plot Mode	Pole Vectors
Vector Count	257 (257 Entries)
Intersection Mode	Mean Set Planes
Intersections Count	28
Hemisphere	Lower
Projection	Equal Angle

APPENDIX 16. Wedge sliding stereo net of the Upper inter-ramp of the North sector.

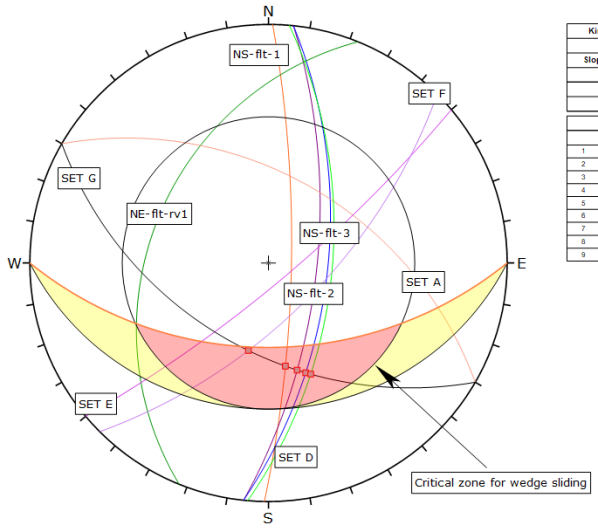

Kinematic Analysis	Wedge Sliding
Slope Dip	51
Slope Dip Direction	180
Friction Angle	27°

	Critical	Total	%
Wedge Sliding	5	36	13.89%

	Color	Dip	Dip Direction	Label
User Planes				
1		79	91	NS-flt-1
2		67	96	NS-flt-2
3		62	96	NS-flt-3
4		37	292	NE-flt-rv1
5		50	30	SET A
6		60	95	SET D
7		80	140	SET E
8		65	135	SET F
9		50	210	SET G

APPENDIX 17. Wedge sliding stereo net of the Middle inter-ramp of the North sector.

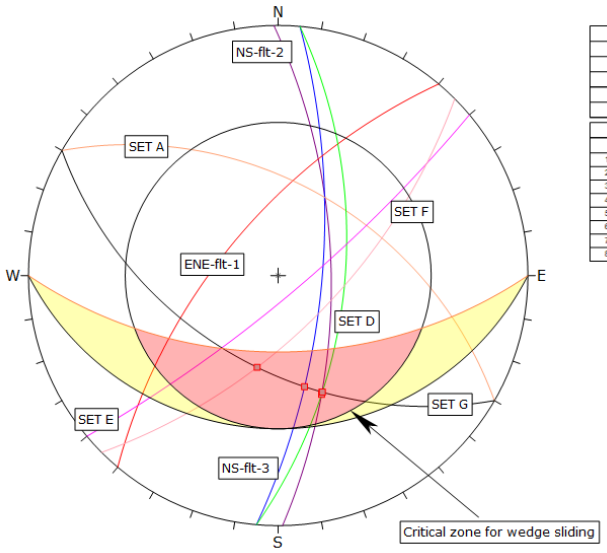

Kinematic Analysis	Wedge Sliding
Slope Dip	56
Slope Dip Direction	180
Friction Angle	27°

	Critical	Total	%
Wedge Sliding	5	28	17.86%

	Color	Dip	Dip Direction	Label
User Planes				
1		66	89	NS-flt-2
2		70	95	NS-flt-3
3		65	310	ENE-flt-1
4		50	30	SET A
5		60	95	SET D
6		80	140	SET E
7		65	135	SET F
8		50	210	SET G

APPENDIX 18. Planar sliding stereo net of the Upper inter-ramp of the North East sector.

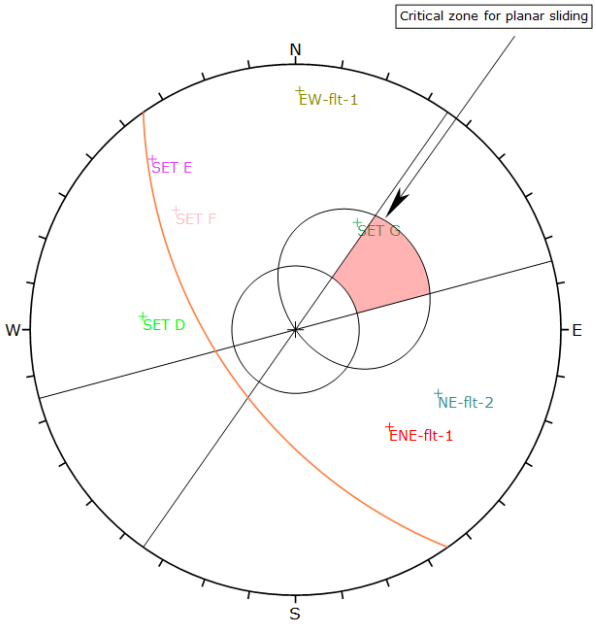

Kinematic Analysis	Planar Sliding
Slope Dip	57
Slope Dip Direction	235
Friction Angle	27°
Lateral Limits	20°

	Critical	Total	%

	Color	Dip	Dip Direction	Label
User Planes				
1		54	316	ENE-flt-1
2		61	294	NE-flt-2
3		84	181	EW-flt-1
4		60	95	SET D
5		80	140	SET E
6		65	135	SET F
7		50	210	SET G

APPENDIX 19. Wedge sliding stereo net of the Upper inter-ramp of the North East sector.

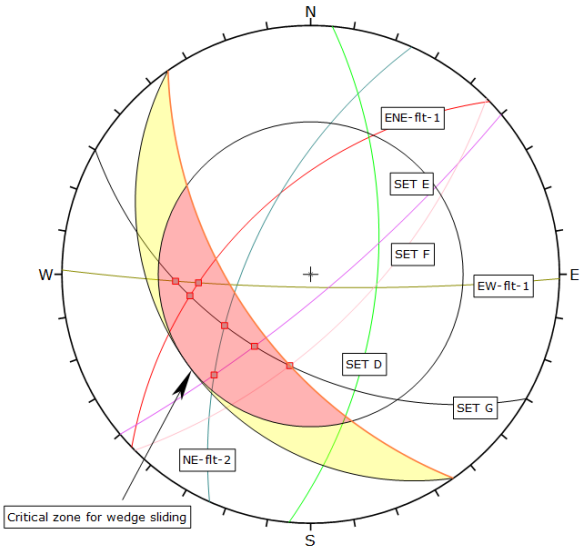

Kinematic Analysis	Wedge Sliding
Slope Dip	57
Slope Dip Direction	235
Friction Angle	27°

	Critical	Total	%
Wedge Sliding	7	21	33.33%

	Color	Dip	Dip Direction	Label
User Planes				
1		54	316	ENE-flt-1
2		61	294	NE-flt-2
3		84	181	EW-flt-1
4		60	95	SET D
5		80	140	SET E
6		65	135	SET F
7		50	210	SET G

APPENDIX 20. Wedge sliding stereo net of the Upper-middle inter-ramp of the North East sector.

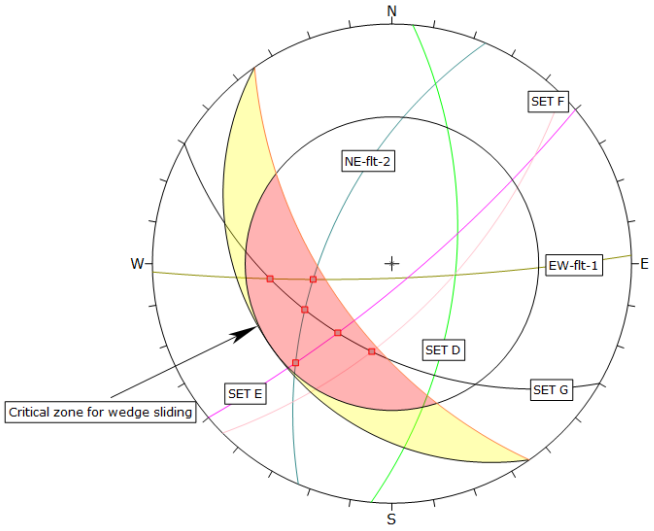

Kinematic Analysis	Wedge Sliding
Slope Dip	60
Slope Dip Direction	235
Friction Angle	27°

	Critical	Total	%
Wedge Sliding	6	15	40.00%

	Color	Dip	Dip Direction	Label
User Planes				
1		58	293	NE-flt-2
2		83	178	EW-flt-1
3		60	95	SET D
4		80	140	SET E
5		65	135	SET F
6		50	210	SET G

APPENDIX 21. Planar sliding stereo net of the Upper inter-ramp of the North West sector.

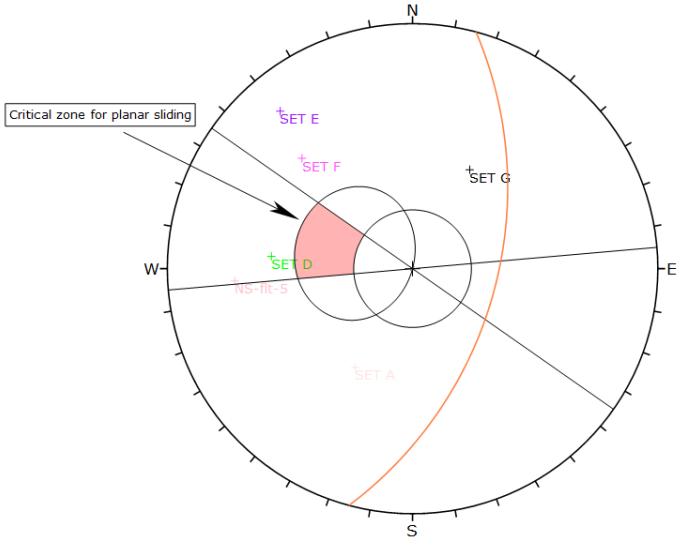

Kinematic Analysis	Planar Sliding
Slope Dip	52
Slope Dip Direction	105
Friction Angle	27°
Lateral Limits	20°

	Critical	Total	%

	Color	Dip	Dip Direction	Label
User Planes				
1		72	86	NS-flt-5
2		50	30	SET A
3		60	95	SET D
4		80	140	SET E
5		65	135	SET F
6		50	210	SET G

APPENDIX 22. Wedge sliding stereo net of the Upper inter-ramp of the South sector.

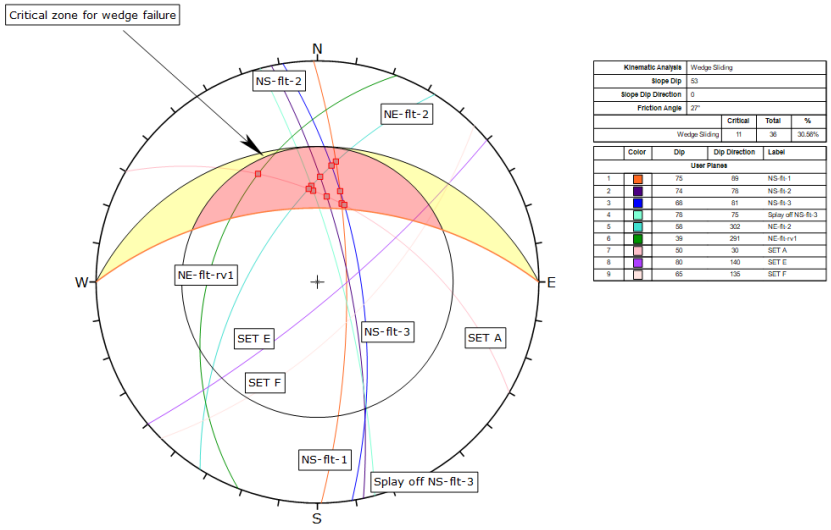

APPENDIX 23. Planar sliding stereo net of the Middle inter-ramp of the South East sector.

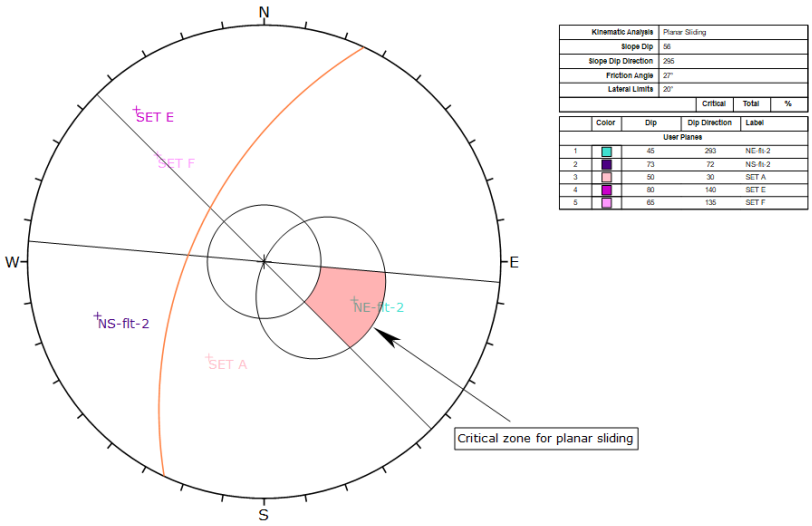

APPENDIX 24. Wedge sliding stereo net of the Upper inter-ramp of the North West sector.